Damage Detection Methodology for Composite UAV Wings using Modal Analysis and Probabilistic Concepts

by

Timothy Prinsloo

A dissertation submitted in partial fulfilment of the requirements for the degree

Master of Engineering

in the Department of Mechanical and Aeronautical Engineering

Faculty of Engineering, the Built Environment and Information Technology

University of Pretoria
Pretoria

2011

Damage Detection Methodology for Composite UAV Wings using Modal Analysis and Probabilistic Concepts

Author: Timothy Prinsloo
Supervisor: Professor P.S. Heyns
Department: Department of Mechanical and Aeronautical Engineering
Degree: Master of Engineering

Abstract

Monitoring of structural integrity is critical in many fields today, and particularly so in the civil, mechanical and aerospace engineering industries. In the aerospace industry, appreciably sized and almost exclusively composite UAVs share the airspace with other aircraft. Such composite structures also pose numerous uncertainties to structural health monitoring and analysis techniques. This necessitates research into a methodology for practical and effective structural health monitoring techniques.

This work presents a methodology for structural health monitoring and particularly delamination detection in composite wing structures. The approach uses experimental modal analysis with due consideration for the probabilistic effects of random variations in material and geometrical properties, for the purpose of a general and non wing-specific damage detection technique.

A large number of composite material coupons were tested to determine statistical distributions of 2D orthotropic material properties, using an optical image correlation system to reduce the expense of testing. Uncertainties in the wing geometry arising from manufacturing variances were taken into consideration. The material properties of the foam spar and resin beadings were considered isotropic and deterministic. A finite element model of the wing was subsequently improved using a scanning laser vibrometer to conduct detailed experimental modal analyses of five wings, and a multi-model updating approach based on frequency and mode shape information was used to update selected sensitive material properties. Significant improvement was accomplished.

Using the probabilistic material property database, a confidence region was established for wing mode shapes through a Monte Carlo procedure. It was shown that delamination effects are capable of perturbing the dynamic mode shapes beyond the confidence regions implied by the material uncertainties. This provides a basis for further development of a structural health monitoring methodology for composite structures, taking due account of the many uncertainties in the structure.

Acknowledgements

Contents

List of Figures

List of Tables

Nomenclature

Symbol	Description	Unit
English Letter		
a	Partial Derivative of Taylor Series	
C	Damping	N.s/m
E	Young's modulus	Pa
f	Forcing vector	N
G	Shear modulus	Pa
K	Stiffness modulus	N/m
L	Ribbon direction	
M	Mass	N
N	Number of degrees of freedom	
P	Material property	
Q	Reduced stiffness matrix	
S	Compliance matrix	
s	Sample standard deviation	
S	Sensitivity matrix	
t	Time	S
u	Displacement	m
$\dot{u}$	Velocity	m/s
$\ddot{u}$	Acceleration	m/s^2
W	Direction of expansion	
$\bar{x}$	Sample mean	
X	Normally distributed variable	
Z	Ply thickness	
Greek Letter		
γ	Coefficient of variance	
γ	Shear Strain	
ε	Tensile Strain	
μ	Mean	
v	Poisson's Ratio	
ρ	Density	kg/m^3
σ	Standard Deviation	
σ	Tensile Stress	Pa
τ	Shear Stress	Pa
ψ	Mode Shape	
ω	Circular Frequency	rad/s
Abbreviations		
1/2/3D	One/Two/Three Dimensional	
ASTM	American Society for Testing and Materials	
CSC	Cross Signature Correlation	
CSIR	Council for Scientific and Industrial Research	

Abbreviation	Description
DFRF	Displacement Frequency Response Function
DICS	Digital Image Correlation System
EMA	Experimental Modal Analysis
FBG	Fibre Bragg Grating
FE	Finite Element
FEA	Finite Element Analysis
FEM	Finite Element Model
FRF	Frequency Response Function
FRP	Fibre Reinforced Plastic
IPV	Inner Product Vector
ITE	Impulse Excitation Test
LST	Lightweight Structures Technology
MAC	Modal Assurance Criterion
MB	Model-based
MCS	Monte Carlo Simulation
MDOF	Multi Degree of Freedom
MIF	Modal Identification Function
MIMO	Multiple Input Multiple Output
NDI/E/T	Non Destructive Inspection/Evaluation/Testing
OMA	Operational Modal Analysis
PC	Personal Computer
PCE	Polynomial Chaos Expansion
PDE	Partial Differential Equation
PPS	Product Data Sheet
PR	Pattern Recognition
Q4/8	Quad Four/ Eight
RFOP	Rational Fraction Orthogonal Polynomials
SDOF	Single Degree of Freedom
SFRF	Strain Frequency Response Function
SHM	Structural Health Monitoring
SIMO	Single Input Single Output
UAV	Unmanned Aerial Vehicle

1. Introduction and Literature Review

1.1. Introduction

Monitoring of structural integrity is critical in many fields today, and particularly so in the civil, mechanical and aerospace engineering industries. In the case of unmanned aerial vehicles (UAVs), which share airspace with many types of aircraft, it is increasingly becoming important to know the structural condition of these not necessarily small aerial vehicles. As a result, serious research is being done in this area from various perspectives and employing a multitude of techniques, from visual to acoustic. An interesting challenge in this field is the development of condition monitoring techniques that can be applied to production products made from composite materials.

This work develops a structural health monitoring methodology for use on production composite UAV wings, through vibration analysis. While many damage detection techniques are applicable, they still remain very specific to the structure in question. This can be a problem in the case of complex composite structures such as UAV wings, in which repeatability of manufacture is an issue. This necessitates the need for an uncertainty approach.

Variability of material properties such as elastic modulus tends to follow a specific distribution, which is transferred through the eigen-value problem and response analysis to a distribution of dynamic characteristics (resonant frequencies, damping factors and modal constants). This in conjunction with confidence bounds, variance etc. creates a data-base for a set of production wings. That is, a production wing can be expected to comply with a specified dynamic behaviour within specific confidence bounds.

To implement this, a distribution of 2D-Orthotropic material data, including longitudinal, transverse and shear stiffness as well as Poisson ratios, is created from tensile tests. The coefficient of variance of the composite pre-preg skin properties is around 4-12%. Three undamaged wings are dynamically excited under free vibration conditions and a scanning laser Doppler vibrometer is used to measure the response. The dynamic tests are then used, in conjunction with finite element models, to perform multi-model updating and extract the material properties, for each skin ply etc. This is specific to each wing and found to lie within the predicted data distribution and range. The model updating compares dynamic constants in an optimising routine that continually adjusts selected parameters (Young's modulus etc.) in the model in order to optimise the fit to the test data.

The finite element model is then used in a Monte Carlo fashion to determine a distribution and confidence bound for the dynamic characteristics, which comply with the dynamic characteristics from the dynamic test results, extracted through experimental modal analysis.

Damage (specifically delamination) is considered through three case studies (three delaminated wings of increasing delamination size); the effect can be seen to lie outside the

desired dynamic confidence bounds. This then displays a perturbation of expected dynamic behaviour which can be used for damage detection.

Initial tests to validate the model updating and dynamic test process were first done deterministically using Fibrelam off-cut panels, acquired from Aerosud. Fibrelam comprises of an aramid honeycomb core bonded between woven glass fibre/phenolic composite skins.

1.2. Literature Review

Composite materials are increasingly being used in primary structures of aircraft like the Boeing 787, AirbusA380, Typhoon Euro fighter and in UAVs, because of their superior strength properties over metallic materials. Fibre reinforced materials are however more complex. Their structural anisotropy and the combination of different phases of material (fibres and matrix) result in various types of damage, and damage detection remains a challenging task (Diamanti and Soutis, 2010:342).

1.2.1. Damage

Delamination, probably the most frequently occurring damage, is a de-bonding of adjoining plies in laminated composites. The causes of delamination such as imperfect bonding, cracks in matrix materials, separation of adjoining piles and broken fibres, may originate during manufacturing or may be induced during in-service loading, such as by foreign object impact or by fatigue (Zou, Tong and Steven 2000:357).

Kashtalyan and Soutis (2007) describe the most commonly encountered type of damage as being caused by impact. Significant degradation of the mechanical properties can easily occur as a result of low-velocity impact (due to their low through-thickness strength).

If the energy of the impacting object exceeds a specific threshold, the internal bonding between adjacent fibre layers is destroyed over a certain area around the impact location. In the delamination region the un-bonded fibre layers are free to glide along the fibre plane directions which result in local reduction in shear stiffness and additional friction (Keye, 2006:201).Delaminations may not be visible on the surface of composite structures, since they are embedded within the laminates, but they may still have significant effects.

A significant amount of work has been conducted in order to determine the influence of damage on composite structures. This work has been done in conjunction with development of non-destructive inspection/evaluation/testing (NDI/E/T) techniques (Diamanti et al. 2010).

1.2.2. Experimental Damage Detection

Currently available non-destructive evaluation (NDE) methods are mostly non-model methods, i.e., either visual or localized experimental methods, such as acoustic or ultrasonic methods, magnetic field methods, radiographs, eddy-current methods or thermal field methods (Doebling, Farrar, Prime and Shevitz, 1995).Diamanti et al. (2010) reviews the use

of low frequency Lamb waves generated by piezoelectric transducers for internal laminate damage identification.

Some of these techniques are impractical for aircraft testing. Almost all of these techniques require that the vicinity of the damage is known in advance and that the portion of the structure being inspected is readily accessible for human beings and unfortunately these experimental methods can only provide local information.

Shortcomings of currently available NDE methods indicate a requirement of damage inspection techniques that can give global information on the structure and do not require direct human accessibility of the structure.

This requirement has led to the development of model-based methods that examine changes in the vibration characteristics of the structure and also led to the development of smart structures/intelligent material systems which have the ability to detect damage on-line, and the capacity to locate the position of the damage (Zou, et al. 2000).

1.2.3. Model and Response Based Damage Detection

Model-based (MB) methods are those that analyse structures through the implementation of finite element analysis. Finite element (FE) models are modified to simulate damage and experimental data can then be compared with the numerical data to determine damage location and extent. The effectiveness of the whole group of MB techniques, however, is dependent on the accuracy of the structural model and these methods may have difficulties when applied to complex structures (Zou, et al. 2000). Various response characteristics of the structure such as modal analysis, time response, frequency response and impedance response can be extracted from models and analyzed.

Modal analysis methods use information from all modal parameters (modal frequencies, mode shapes and modal damping ratio). These methods assume that modal parameters are functions of the physical properties of the structure (mass, damping and stiffness). Changes in the physical properties resulting from damage will thus cause changes in modal characteristics (Vanlanduit, Parloo and Guillaume, 2002).

Typical modal analysis methods include: frequency response function methods, modal shape changes methods, modal shape curve methods, sensitivity-based update methods and change in measured stiffness methods.

Monitoring of damage in composite structures using frequency responses and specifically resonance frequencies has been extensively explored (Salawu, 1997). Kessler, Spearing, Atalla, Cesnik, and Soutis (2002) found that the method was reliable for detecting small amounts of damage in a simple composite structure, however, the potentially important information about damage type, size, location and orientation was lost using this method since several combinations of these variables can yield identical response signatures.

As an overview in terms of vibration, delamination decreases the natural frequency of the structure in question and causes changes to the mode shape, as a result of the reduction in stiffness caused by the delamination. Small delaminations however, have little effect on low order vibration mode frequencies (Della, 2007).

The increase of friction in the delamination is generally perceived as an increase in modal damping (Saravanos and Hopkins, 1996:992). The alteration to mode shapes is restricted to the immediate vicinity of the delamination and decreases rapidly with distance from the damage location (Keye, 2006).

For structural mass, the effects of delamination are usually very small and can often be neglected (Zoe, et al. 2000).

Alnefaie (2009) numerically researched the effects of delamination on the mode shapes in composite plates. It was found that while the effects were local they were also mode dependent, which means that the damage could only be effectively detected in modes that excited the damaged location, as with mode shape seven in figure 1-1. Typically, delaminations that lie near nodal lines have little effect on vibration.
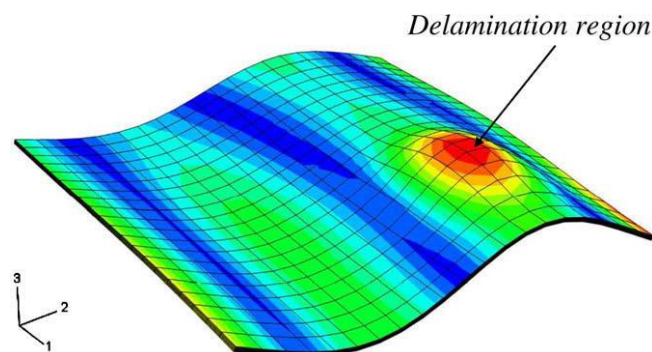
Figure 1-1: The Seventh Mode Shape of Plate C (Alnefaie, 2009)

A pattern recognition (PR) method based on frequency response functions (FRFs) of a healthy and damaged scale aircraft wing was developed by Trendafilova, Cartmell and Ostachowicz (2008).A PR procedure developed from the nearest neighbour principle was applied to recognise difference in categories of damaged and healthy data over a selected frequency band.

More recently an inner product vector (IVP) method was developed by Yang, Wang, Wang, Ding and Dang (2009) which incorporated cross correlation of mode shapes. An IVP difference between intact and damaged structure modes was adopted as a damage index. Location of damage was determined by an abrupt change in this index.

Pandey, Biswas and Samman (1990) calculated curvature mode shapes from displacement mode shapes using a central difference approximation. Curvature modes shapes are related to flexural stiffness. It was again found that damage effects were local but reduced curvature shape amplitude. Wahab and Roeck (1999a) extended this method for application in the civil engineering industry as applied to bridges.

Maeck, Wahab and Peeters (2000) and Gentile and Saisi (2007) both used degradation of structural stiffness as methods of damage detection in concrete structures.

1.2.4. Damage Detection with Model Updating

The methods discussed above generally compare modal parameters of an undamaged structure with the modal parameters obtained on the same structure in a damaged condition and are described by Lauwagie, Sol and Dascotte (2002a) as more response-based. Wahab, Roeck and Peeters (1999b) investigated a damaged reinforced concrete beam under laboratory conditions as an application of a more model-based approach. This method aimed at finding a set of model parameters of a FE model in order to have an optimal correlation between the experimentally measured and numerically calculated modal parameters. Damage was then assessed by investigating the obtained model parameters.

Kharrazi, Carlos, Brincker and Dascotte (2001) detected damage in a four story steel structure by observing changes in FE model element properties after model updating. Damage was simulated by removing members of the structure. Teughels, Maeck and De Roeck (2002) used damage functions, representative of reduction in element bending stiffness, in a sensitivity-base FE model updating routine to access damage in a reinforced concrete beam. Later, in 2004, Teughels, et al. applied the method to a highway bridge.

Model updating was proposed as a possible tool to reconstruct damage patterns by Lauwagie, et al. (2002a).The paper discussed the application of a model-based approach to identify homogeneity of an undamaged cement beam, and the damage pattern of the same beam after damaging.

1.2.5. Smart Materials

Methods like damage detection based on curvature mode shapes as discussed before, require offline investigation and large equipment. Development of a smart material capable of actuating and sensing responses is a significant leap towards online structural health monitoring (SHM). A smart structure/material contains a network of embedded and/or surface bonded actuators and sensors (Chattopadhyay, Changho and Dragomir-Daescu, 1999).

This capability allows for research into areas of condition monitoring like piezoelectric application and strain modal approaches utilising strain gauges and fibre optics.

The strain modal approach has been investigated as a leading practical engineering application for the last decade. Yam, Leung and Xue (1996) derived a relationship between the strain mode and displacement mode for vibrating elastic structures. Through finite element modeling it is possible to relate the strain frequency response function (SFRF) and displacement frequency response function (DFRF).Strain modal analysis holds the advantage of being more sensitive to local structural changes than displacement (Yam, et al. 1996).

With modern equipment like the Polytec Doppler scanning laser vibrometer, it is possible to directly measure velocity response. Displacement can be obtained through integration of the velocity response. Strain responses are then attained from this through spatial differentiation (Spangenberg, 2009).In the past this method was hampered by difficulty in acquiring precise data from accelerometers. Alternatively strain can be directly measured with the use of strain gauges but mathematical difficulties relating to the asymmetrical nature of the SFRF requires more test data to attain a DFRF (Vári and Heyns, 1997).

Advancements in fibre-optics have led to materials embedded with fibre Bragg gratings (FBGs). Cusano, Capoloung, Campopiano and Cutolo (2006) performed experimental modal analysis on a model aircraft wing embedded with fibre-optic sensors, based on FBGs, to measure strains. SFRFs were extracted from the FBGs and DFRFs from accelerometers. Cusano, et al. (2006) found good correlation between strain and displacement modes.

Grouve, Wamet, de Boer, Akkerman and Vlekken (2008) investigated, through a simple model, shifts in resonance frequencies only, for the detection of a delamination in a simple beam. FBGs were used to obtain resonance frequencies of delaminated fibre reinforced cantilever beams and accelerometer results were used to validate the results. It was concluded that the use of FBGs for modal analysis provides opportunity for structural health monitoring of composite laminates.

1.2.6. Model Updating for Material Identification

With the development and application of composites, interest in novel techniques of analysis of the mechanical behaviour of these materials has ensued. Cunha and Piranda (1999) applied a sensitivity based model updating technique to determine the stiffness properties of a composite plate from dynamic tests. Later Lauwagie, Sol, Roebben and Heylen (2002b) validated the Resonalyser method for material identification of steel and aluminium plates by comparison to impulse excitation tests (IETs).

The Resonalyser method uses measured resonance frequencies to identify orthotropic material properties through model updating while IETs use analytical formulas to calculate the elastic moduli from the resonance frequencies (Lauwagie et al., 2002b).

Oliver, Kosmatka, Hemez and Farrar (2006) developed a small series of all-composite test pieces emulating wings from a lightweight all-composite UAV to support SHM. The wings consisted of four main components; two pre-preg and honeycomb co-cured skins (top and bottom skin) and two pre-preg spars. These were assembled in a secondary process using structural adhesive.

Each wing component was modelled separately (meta-model) and updated through correlation with modal analysis results from each component. After updating the full FE model was constructed from the meta-models and compared to the first 20 resonant frequencies form the fully constructed wing. Results showed and overall frequency improvement of 32.6% for the full meta-updated FE model.

Lauwagie and Dascotte (2002c) developed a multi-model updating technique for material identification of layered materials. By combining one numerical (FE) model with corresponding experimental modal data for each type of material present, enough global correlation equations between numerical and experimental responses can be acquired to find a unique solution for material properties. Thus an entire FE model can be updated as a unit. Lauwagie only used resonant frequencies as response parameters.

Correlation of the correct numerical and experimental responses is vitally important. If during model updating a switch of mode shapes occurs (FE modes no longer correspond to the correct experimental modes), as may easily happen with closely coupled modes, updating will fail (Euler, Sol and Dascotte, 2006). The correlation of responses must then be manually checked and altered between update iterations. Euler, et al. (2006) explored the use of mode shapes for response correlation and found that if the MAC matrix is diagonal after updating, no switching occurred.

1.2.7. Uncertainty in Structural Vibration Modelling

The transition from research to practice in the field of SHM has been rather slow. One major reason for the slow-progress in applying diagnostic technologies to real-world structures is the existence of uncertainty in every step of the damage assessment process (Lopez and Sarugul-Kiljn, 2010).

Factors like delamination crack-tip singularities, matrix cracks, moisture content and temperature variation have effects on the repeatability of laminate vibration modes (Della, 2007). Some major uncertainty factors are structural related and are categorised into four groups (Allegri, Corradi and Marchetti, 2006);

- uncertainties affecting material properties like stiffness and strength modulus,
- uncertainties regarding geometrical configuration,
- uncertainties about applied constraints and
- uncertainties with regard to applied loads.

Singh, Bisht, Pandir and Shukla (2009) considered material uncertainty and found the elastic modulus to have dominant effects on scattering of resonant frequencies as compared to other properties. Sensitivity to material properties changed with laminate thickness and oscillation amplitude.

Small variance in ply angle can have a significant effect on mode shape. Teh and Huang (1980) experimented with fibre orientation in composite beams and found that due to torsion-flexure coupling, the orientation is significant for angles less than 25°.

Uncertainty is usually identified as aleatory/variability uncertainty or epistemic/subjective uncertainty. Aleatory uncertainty pertains to inherent variation associated with the system where as epistemic uncertainty refers to a lack of knowledge (Lopez, et al. 2010).

1.2.8. Epistemic Uncertainty: Fuzzy Logic

Chandrashekhar and Ganguli (2009) used fuzzy theory, which facilitates epistemic uncertainty (fuzziness from lack of knowledge), with a new sliding window defuzzifier for damage detection. A steel beam with elastic modulus uncertainty, coefficient of variance (COV) of 3%, and noise level of 0.15 in measurement data, was used to test the method and it was found to detect damage with 94% accuracy.

De Gersem, Moent, Desmet and Vandepitte (2005) used a fuzzy finite element method to calculate uncertain frequency response functions. A case study was performed on the Garteur benchmark problem of a simplified aircraft model. This test-bed is designed and manufactured by Garteur action group to evaluate the efficiency and reliability of ground vibration tests. De Gersem, et al. identified three areas of uncertainty.

- Firstly uncertainty arose from lack of knowledge about the damping characteristics of the visco-elastic layer as well as the quality of the glue used to bond it to the wings.
- The second area of uncertainty was geometrical with regards to the degrees of freedom at the intersection between the fuselage and wings.
- Finally uncertainty was introduced by Young's modulus.

De Gersem, et al (2005) produced a Fuzzy FRF of the Garteur model with the three uncertain parameters (figure 1-2). The figure illustrates the sensitivity of the upper and lower FRF bounds with respect to the input uncertainty level.
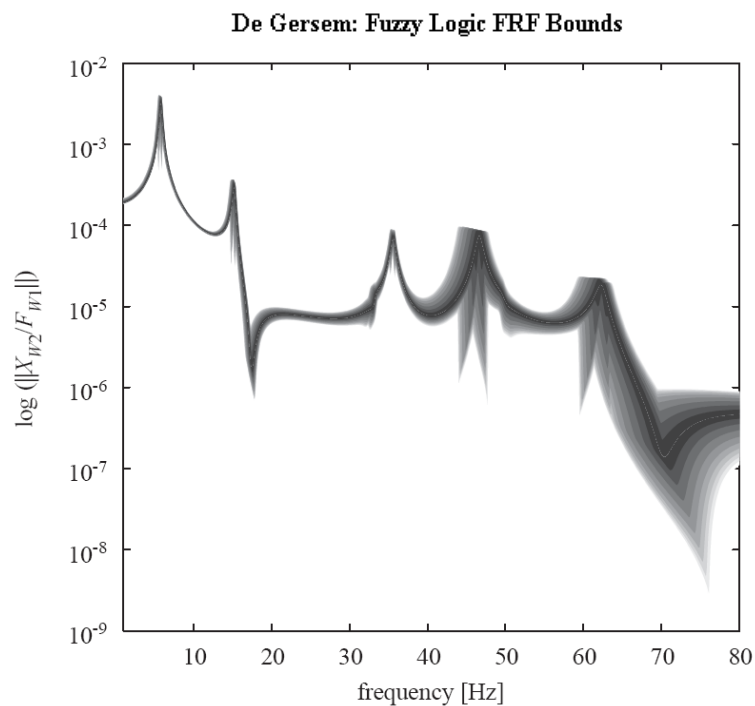
Figure 1-2: Fuzzy FRF of the Garteur Model (De Gersem, et al. 2005)

1.2.9. Aleatory Uncertainty: Probabilistic Methods

Manan and Cooper (2010) developed an approach to determine a probabilistic FRF model using the Polynomial Chaos Expansion (PCE) technique. PCE models are developed for the modal parameters determined from curve-fitting FRFs obtained from a FE model using a Latin Hypercube technique to define the test cases. The individual probabilistic frequency, damping ratio and complex amplitude PCE models are then combined to define the probabilistic FRF–PCE model.

Manan, et al. (2010) illustrated the methodology on a simple cantilever beam with variation in Young's Modulus. A study was then performed on an aircraft composite wing FE model in which the longitudinal and shear modulus were allowed to vary. The probability density function (PDF) estimates, using the PCE approach for the modal parameters, and the overall FRF scatter bounds were compared and found to correlate very well with those obtained from extensive Monte Carlo simulations(MCS), as in figure 1-3.
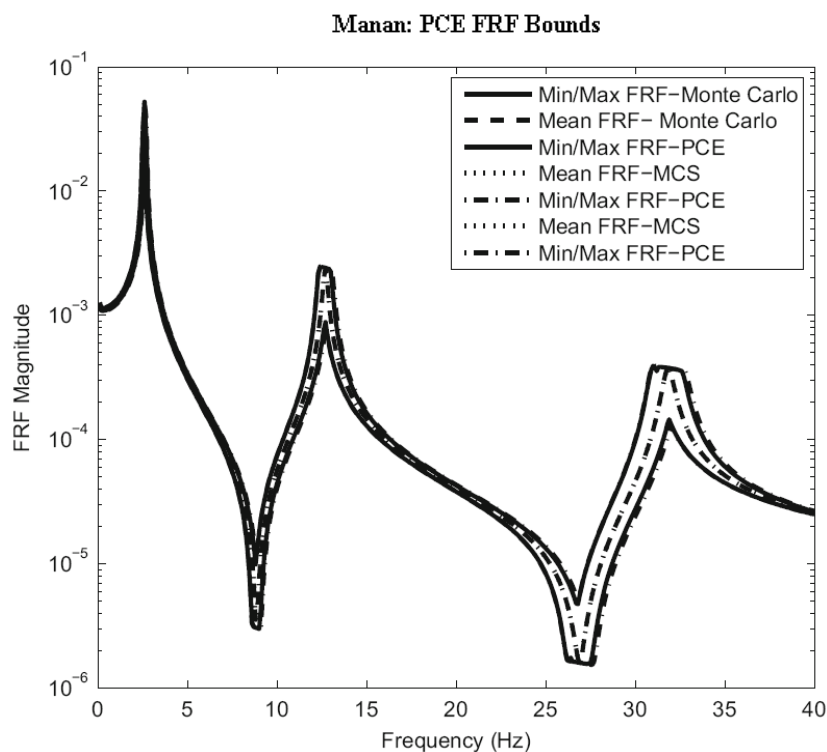
Figure 1-3: 95% Confidence Bands on Composite Wing FRF (Manan, et al. 2010)

Chen, Duhamel and Soize (2006) validated a non-parametric probabilistic approach which allows model uncertainties and data uncertainties to be taken into account and developed to predict low and medium frequency dynamics of structures.

Chen, et al. (2006) experimentally tested eight composite sandwich panels and it was noted that that the experimental responses almost always belong to the predicted confidence region. Where the experimental results fall outside the confidence region it is due to the fact that the predicted region is calculated with a probability level 0.96 and not with the level 1.Figure 1-4 shows good correlation with experimental results.
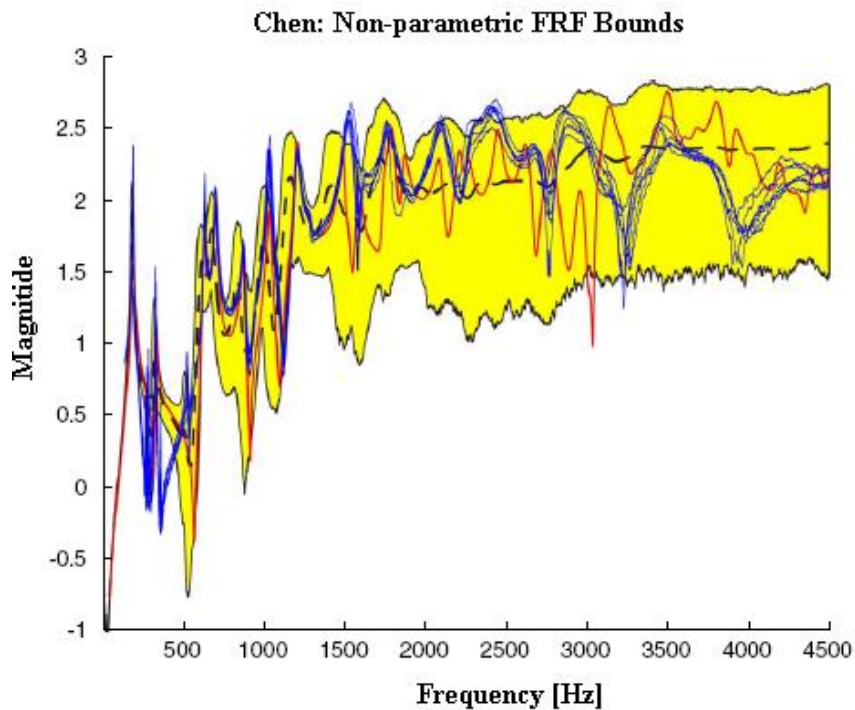
Figure 1-4: 96% Confidence Bands on Composite Sandwich FRF (Chen, et al. 2006)

Typically the methods discussed above can be and often are verified using the probabilistic Monte Carlo approach. Monte Carlo techniques are used in combination with FEM and iteratively produce solutions for stochastic distribution of response on the basis of the stochastic distribution of the input, e.g. materials, geometry and loading (Van Vinckenroy and de Wilde, 1995).

This is certainly the simplest and most trusted probabilistic method to quantify variability but requires computation time and resources for complicated models. Thus other methods have been developed to deal with uncertainty. Monte Carlo however still remains a basis for method verification and is widely used to quantify uncertainty.

1.3. Project Scope

Application of SHM research has been a formidable challenge in the real world. This problem has been brought about by various structural and modelling uncertainties. In the case of composite UAV wings, variances in material characteristics result in profound variance in modal parameters.

Although research has been done to explore these effects, it has been limited to natural frequencies and frequency response functions. Furthermore, incorporating these findings in into an SHM methodology still needs to be done effectively. While many SHM techniques show promising results, they are wing specific. The consequence of this is that they cannot be applied to production wings that may show appreciable variance in structural parameters and modal response.

To fill the gap between research and application, this dissertation presents a methodology for damage detection in composite UAV wings through modal analysis, while considering

stochastic material properties with a probabilistic approach. Three, often separate, fields of research have to be combined; effects of material variability on the vibration of structures, Multi-model updating, and SHM.

A combination of advanced experimental and post processing techniques must be correlated with numerical modelling to construct a basis for Monte Carlo simulation. A database of variable mode shape responses will then define a confidence range in which the varied modal responses from a production line of wings are expected to fall. Any perturbation from this confidence interval is cause for concern and may be related to wing damage.

The main outcomes of this research include:

- The construction of a distribution of 2D orthotropic material properties of the laminate UAV pre-preg skins. This is established using an advanced image correlation system and extensive tensile testing.

- Attaining the experimental modal parameters (in particular mode shapes) of six UAV wings including two additional geometrically different responses for an undamaged wing. A scanning laser vibrometer is used to obtain precise response measurements.

- Construction of a finite element model representative of the wing structure.

- Multi-model updating, in an effort to improve correlation between FEM and experimental modes for non-destructive dynamic material identification and as a basis for probabilistic analysis.

- The construction of a confidence region on modal parameters (mode shapes in particular) representative of the undamaged UAV wing case.

- A case study utilising the proposed SHM methodology for damage detection on three damaged wings.

1.4. Dissertation Flow

Two composite structures are considered in this research. Fibrelam sandwich panels are used to establish testing and numerical analysis procedures. These panels are not considered probabilistically and are confined to simplifying assumptions with regard to laminate modelling. Test results from four of these panels are used in the dissertation. Six more are used for surface reflection tests and general setup familiarisation.

Secondly composite UAV wings are considered. These represent a much more complex configuration with a symmetric airfoil. They are geometrically simplified by removing structural components like ribs, hard points and structural mountings but still retain complexity through the airfoil shape and interaction between a stiffening spar, laminate skins and resin beadings.

Six composite UAV wings were manufactured of which three were embedded with circular delamination defects of increasing size at the same central location. The three remaining undamaged wings are necessary for repeatability studies. Resin beadings joining the top and bottom aerofoil skins at the leading edge failed in one of the undamaged wings and resulted in an unexpected fourth damaged wing case.

The flow of the project is depicted in figure 1-5. Here all the aspects of the work are linked together respective of interaction with necessary fields.

The research starts off with two types of experimental testing; destructive and non-destructive. These separate fields are processed and combined at a model updating stage from which a probability analysis follows.

A destructive testing procedure is followed to determine the physical material properties of the structure. This is achieved through tensile testing and where available and applicable, from material data sheets. Tensile test coupons are prepared in accordance with ASTM testing standards and used to extract 2D orthotropic tensile moduli, shear moduli and Poisson's ratio of composite laminates. The data here is used for two purposes. With extensive testing, a probabilistic distribution of the material properties is created in addition to providing initial "guess" values for finite element modelling.
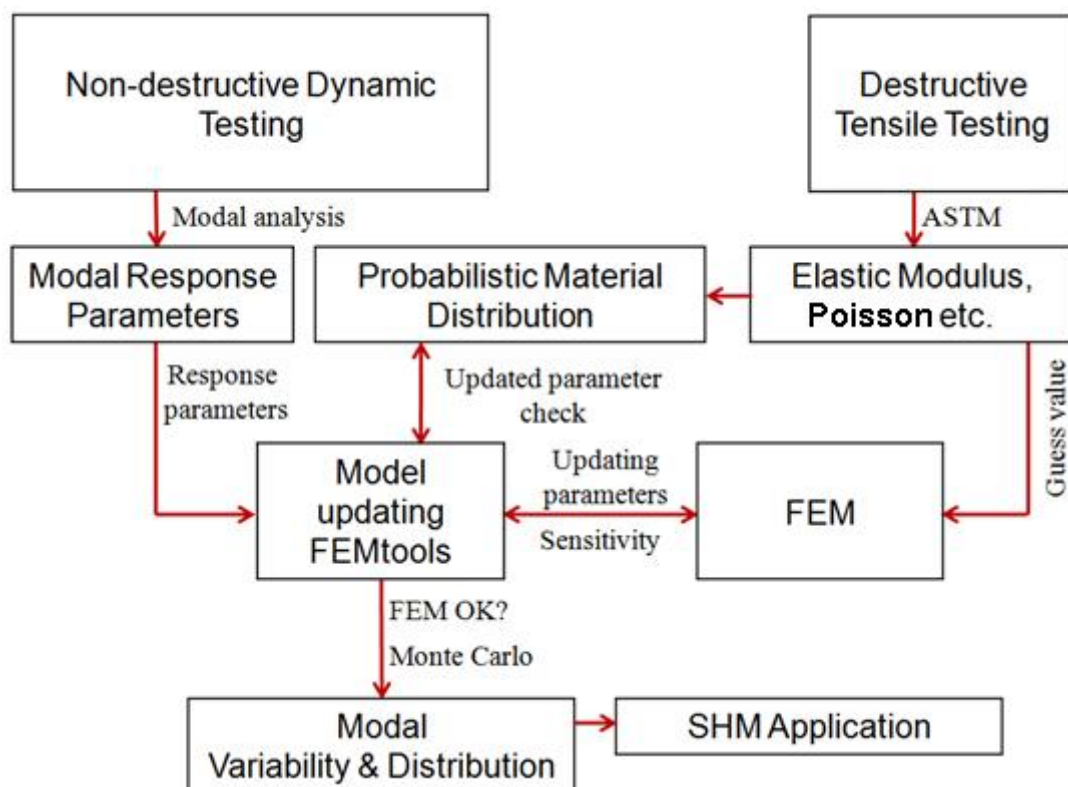
Figure 1-5: Project Methodology Flow Chart

The second area of experimental testing is non-destructive. With the use of a scanning laser vibrometer the dynamic response of the structure in question is captured. Through advanced signal processing and modal analysis, modal response parameters are retrieved that describe the vibration characteristic of the structure. These responses provide correlation parameters

for model updating and later response data for SHM case studies when damage cases are considered.

The dynamic test setup is further simplified by considering free-free vibration conditions. Uncertainty relating to boundary conditions and structural loading is largely eliminated and only geometrical and material uncertainty remains in terms of the structure.

A finite element model is constructed for both Fibrelam and UAV wing structures. A normal modes analysis is performed and numerical data is produced with the intent of correlating the model response with experimental modal parameters.

This correlation is improved by a multi-model updating procedure. This analysis requires an experimental setup for each material to be updated in the structure. That is three experimental dynamic tests for a UAV wing constructed from a laminate skin, foam spar and resin beading. Fibrelam panels require two test setups, one for each of its material components; laminate skin and honeycomb core. Each setup varies only in geometrical shape (length of the component).

By correlating modal response parameters from the numerical FE model and experimental results, enough correlation parameters are obtained in conjunction with the multiple models to update material parameters from all materials in the structures. A sensitivity analysis determines the most sensitive material properties and thus identifies those which can be considered deterministic, due to minimal effects from property variation and those which should be considered probabilistic.

Updating of an FE model to better match the experimental responses of an undamaged structure serves as a method of non-destructive material testing of the material in that specific structure from which the experimental results was obtained. Comparison of the converged values of material property parameters with the distribution created by tensile testing, verifies the FE model and model updating procedure. Another consequence of the model updating is that materials considered deterministic are now updated and reliably representative of production components. A base FE model representative of an undamaged structure has thus been created and by varying the probabilistic parameters through a Monte Carlo procedure, modal responses can be quantified to represent expected responses from undamaged wings later on in a production line.

The research then proceeds to test these modal parameter bounds to verify if indeed undamaged wings will fall within the predicted confidence region and if the effects of delamination damage will be large enough to force changes in the modal parameters that will make them fall outside the predicted region.

1.5. Dissertation Overview

This dissertation comprises six chapters. Each chapter focuses on a main aspect of the project and is briefly summarised here.

1. Introduction and Literature Review

The problem is introduced and investigated in literature. Main aspects and methods for each area of interest are considered and reviewed. The project scope is defined and all aspects of the dissertation are related in a flow chart. The main project outcomes are presented.

2. Basic Theory

This chapter covers the main theoretical aspects required for this research. Basic vibration concepts are covered followed by composite theory. Probability is explored and analytically applied to a SDOF system. Finally the essence of model updating is tackled and important concepts discussed.

3. Manufacturing, Specifications and Materials Testing

This chapter includes two main aspects of this dissertation, manufacture and destructive materials testing. Both Fibrelam and the composite UAV wings specifications are presented and structural material properties are attained through tensile testing and retrieved, when available, from materials data sheets.

4. Vibration Testing and Modal Analysis

The non-destructive aspect of the experimental testing is dealt within this chapter. Vibration response data is first collected and analysed. Setup configuration is covered and explained after which the applied signal processing is discussed and frequency domain results are presented. In the second section the acquired vibration data is post-processed through modal analysis and modal parameters are presented and discussed.

5. FE Modelling and Updating

This chapter presents the procedure followed for modelling the Fibrelam and UAV structures as well as updating them to more accurately present experimental test results. This chapter aims at creating a FE model representative of a standard wing that can be used as a basis for Monte Carlo simulation.

6. Probabilistic Analysis

This chapter has two main objectives. Firstly a Monte Carlo simulation is performed to ascertain the effect of material variability on modal response. The definition of a confidence region on modal responses is then used in case studies to verify if undamaged wing responses fall within this confidence region and whether damage can be detected.

2. Basic Theory

This chapter explores four main theoretical categories. Essential vibration basics are covered along with composite laminate theory required for FE modelling. Probabilistic concepts are discussed and expanded for application in vibration analysis. Finally model updating is investigated and essential procedures and requirements covered.

2.1. Vibrations

To begin simply, the vibration of a structure is characterised by its mass and stiffness. Damping is simply an influence over the magnitude of vibration. Typically the dynamic response of a structure can be mathematically described using these parameters.

2.1.1. Single Degree of Freedom

For a single degree of freedom (SDOF) system, their relationship is described by Rao (2005:117) as:

$$\omega_n = \left(\frac{K}{M} \right)^{\frac{1}{2}} \tag{2.1}$$

where M is the structural mass, K structural stiffness and ω_n is the natural/resonant frequency.

Unfortunately things are more complicated than this in the real world and these parameters are more likely related in a multi-degree of freedom (MDOF) scenario.

2.1.2. Equation of Motion

Rao (2005:220) describes the governing equation of motion for a linear, discrete system as:

$$\left[M \right]\{\ddot{u}(t)\} + \left[C \right]\{\dot{u}(t)\} + \left[K \right]\{u(t)\} = \{ f(t) \} \tag{2.2}$$

were $[C]$ is the structural damping matrix, $\{f(t)\}$ is the force vector in the time domain, $\{\ddot{u}(t)\}$ is the acceleration vector, $\{\dot{u}(t)\}$ is the velocity vector and $\{u(t)\}$ is the displacement vector all as a function of time t.

In finite element modeling, a single equation of the form of equation (2.2) is generated for each degree-of-freedom (DOF) in the model. Each node or grid point in the finite element mesh can have up to six DOFs (three translations and three rotational motions). The matrices [M], [C] and [K] have to be estimated, either by finite element discretisation or by experimental system identification (FEMtools, 2010:3).

The eigen-values and eigen-vectors can be extracted from equation 2.3.

$$\det\left(\left[K\right] + s\left[C\right] + s^2\left[M\right]\right) = 0 \qquad\qquad (2.3)$$

Since the eigen-vectors are not unique in value but only in shape, they are called mode shapes. Modal damping, natural frequency and mode shapes are called the modal parameters of the structure.

2.1.3. Damping

Damping is an important element in the analysis of dynamic systems. Damping is difficult to model accurately since it is caused by many mechanisms including viscous effects (e.g. dashpot, shock absorber), external friction (e.g. slippage in structural joints), internal friction (e.g. characteristic of the material type) and structural non-linearity (e.g. plasticity, gaps).

Because they are so difficult to estimate, damping values are usually based on the results of experimental testing or from literature that provides damping values for similar structures. Simple approximations are often justified because many mechanical structures are only lightly damped.

When experimental data is available, the damping model of choice will be the one that allows one to best reproduce the experimental FRFs.

2.1.4. Normal Modes Analysis

Finite elements models are usually built without including the damping of the structure (FEMtools, 2010:3). Nevertheless, the undamped results are still useful in cases where the damping forces in the structure are significantly less than the inertial or stiffness forces. For natural vibrations of undamped structures, the excitation force and the damping matrix [C] are set to zero. This leads to a general eigen-value problem of order N (the number of degrees of freedom of the structure).

The solutions to this real eigen-value analysis problem are called the normal modes. The eigen-values are modal frequencies and the mode shapes are real valued. They are functions of the geometry, materials and boundary conditions of the structure.

Although Patran was used to construct the structural models for this dissertation, FEMtools, rather than Nastran, was used as the modal analysis solver since a solution is required in every model updating step. FEMtools uses a Lanczos subspace method to solve for normal modes. The Lanczos method for eigen-value extraction is a method which owes its popularity in structural-vibration application to its ability to extract a given number of lowest order eigen-values of a system using a minimum number of iterations (FEMtools, 2010).

2.1.5. Frequency Response Analysis

Frequency response functions are an essential frequency domain tool containing modal parameter information. Experimentally, modal parameters are determined from measured

FRFs. It is of particular interest to simulate the FRFs from an analytical model because FRFs can be directly measured. The correlation between analytical and experimental FRFs serves as a measure of the validity of the finite element model. Because FRFs provide response information over a frequency range, the capability of a finite element model to simulate responses in that frequency range can be estimated. FRFs can therefore also serve as responses for correlation analysis, sensitivity analysis and model updating (FEMtools, 2010).

2.2. Composites

A composite material is defined as a material, which on a macro-scale, consists of two or more distinct material types acting in combination Kollar & Springer (2003). This is a very broad definition but the term composite material however, is increasingly being used as a generic term to describe fibre reinforced plastics (FRPs). FRPs typically consist of a plastic matrix which is reinforced by some type of fibre.

2.2.1. A Brief History of Composite Materials

The first composite material known was made in Egypt around 3,000 years ago when clay was reinforced with straw to build walls. The development of FRP's however dates back to the First World War (Kollar et al, 2003), when the British used cotton and sisal fibres to reinforce phenolic resins for the production of some secondary aircraft components. During WWII, engineers soon realised that the processing requirements for FRPs allowed for the manufacturing of complex curved shapes including fairings, radomes and disposable fuel tanks.

In the recent past, primary structure application in the aerospace industry was explored in military aircraft like the F-16 and F-14 tail planes. Typically the use still remained in secondary structures of aircraft.

Today composites are used in the automotive, chemical, electronic construction, marine and aerospace industries (Robert, 1998). In the aerospace industry modern passenger aircraft like the Airbus A380 and the military version A400M consist of more composite components than ever before. In 1986 the Voyer Aircraft was constructed entirely of composite material. Currently UAV's (unmanned aerial vehicles) are the focus of many research projects, including that of the CSIR (Council for Scientific and Industrial Research) in South Africa (Campbell, 2009).

2.2.2. Modern Composite Description

The advantage of composite materials is that, if well designed, they usually exhibit the best qualities of their constituents and often some qualities that neither constituent possesses. Composite materials are commonly used in weight sensitive structures due to their high stiffness/weight ratio (Robert, 1998).

Composite material systems often take the form of either long or short fibre composites (a matrix reinforced with fibres), particulate composites or laminated composites. Laminate fibres, are usually shown as a schematic as in figure 2-1. In practice they will be very small in diameter and scattered through the matrix in a ply (Abbey, 2009).
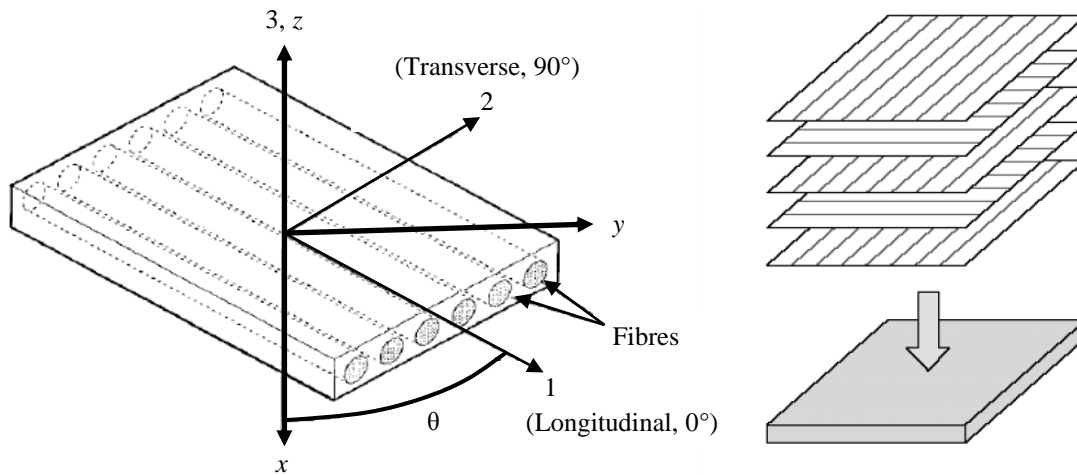
Figure 2-1: Typical fibre schematic, (Abbey, 2009)

The main functions of the fibres are to carry the load in a structural composite (70 to 90% of the load is carried by fibres), provide stiffness, strength, thermal stability, and other structural properties in the composite and to provide electrical conductivity or insulation, depending on the type of fibre used.

The matrix material binds the fibres together and transfers the load to the fibres. It provides rigidity and shape to the structure. The matrix isolates the fibres so that individual fibres can act separately. This stops or slows the propagation of a crack.

Material properties can be found from either datasheet sources or lab testing, but must be treated with caution due to the uncertainty associated with the current understanding of the materials and their behaviour.

In practice plies are rarely used individually, multiple angles are used in a stack of plies to tailor the performance. A stack up of plies (figure 2-1) is formed by either bonding sheets together or by some form of weaving. FEA idealisation usually assumes a 'sheet like' equivalent (Abbey, 2009).

2.2.3. Laminates

There are an infinite number of laminate types that can be developed. These materials can be categorized into three basic areas, core materials, high strength and stiffness skins and outer protective layers (Composites Institute, 1998).

Core materials typically serve the function of connecting and spacing of the skins to develop stiffness and strength in a sandwich arrangement. The key property of core materials is shear

strength to insure shear conductivity between the skins, thus the ability to sustain loads and bending. Core materials are normally wood, honeycomb and structural foams.

The outer structural layer or skins are typically metal or composite, either in combination with a core material or a multitude of high strength and stiffness layers. Composite materials offer the widest range of high strength skins with the ability to change fibre type (fibreglass, carbon and aramid) in addition to the fibre volume and orientation. Composites are well suited for large deflection applications where high strain capability and fatigue resistance are required. Composite materials in a laminate form are applied in the form of pre-cured, pre-preg or "B" stage and wet layup configurations.

The final group of lamina is made up of thermo plastic and thermo-set materials, which act as a covering to the laminate structure.

2.2.4. Macromechanical Behaviour and Classical Laminate Theory

Materials types can be considered to fall in one of three categories (Kollar, et al., 2003); Isotropic materials like metals that have the same material properties in all directions, anisotropic materials with different properties in all directions like volcanic rock or orthotropic materials which is a special case of anisotropic that has clear material directionality in three directions.

Classical laminate theory simplifies the orthotropic material by ignoring the through thickness stress, which is the plane stress assumption as in equations 2.4 and 2.5(Abbey, 2009).

$$\sigma_3 = \tau_{12} = \gamma_{23} = 0 \tag{2.4}$$

$$\therefore \varepsilon_3 = \gamma_{13} = \gamma_{23} = 0 \tag{2.5}$$

An isotropic material can be defined by any two of the three properties in the relationship

$$G = \frac{E}{2(1+v)} \tag{2.6}$$

A 2D orthotropic material using the plane stress assumption needs to consider all of the following five properties; E_1 (fibre Young's modulus), E_2 (transverse fibre Young's modulus), G_{12} (in plane shear stiffness), v_{12} primary Poisson's ratio and ρ (density, for dynamic analysis).

Considering a ply loaded in the with-fibre direction and free to contract in the transverse direction so that the transverse stress is zero, the relationship is as seen in equation 2.7.

$$\varepsilon_1 = \frac{\sigma_1}{E_1} \tag{2.7}$$

The Poisson's ratio expression linking the with-fibre and transverse fibre directions is

$$v_{ij} = -\frac{\varepsilon_j}{\varepsilon_i} \tag{2.8}$$

Applying both stresses simultaneously results in the with-fibre and transverse fibre strain

$$\varepsilon_1 = \frac{\sigma_1}{E_1} - v_{21}\frac{\sigma_2}{E_2} \;,\; \varepsilon_2 = \frac{\sigma_2}{E_2} - v_{12}\frac{\sigma_1}{E_1} \tag{2.9}$$

The in-plane shear is related by the term in equation

$$\tau_{12} = G_{12}\gamma_{12} \tag{2.10}$$

Equations 2.9 and 2.10 can be combined to form the compliance matrix $\{\varepsilon\}=[S]\{\sigma\}$. The inversion of the compliance matrix results in the reduced stiffness matrix $[Q]$. Plies however, are often applied at angles and it is thus necessary to consider these off-axis plies where the with-fibre angle can be arbitrary. The stiffness in the reference directions has to be resolved to attain the transformed reduced stiffness matrix.

The relationship between in-plane forces applied to a set of plies and the resultant in-plane strains can now be considered, as in figure 2-2.
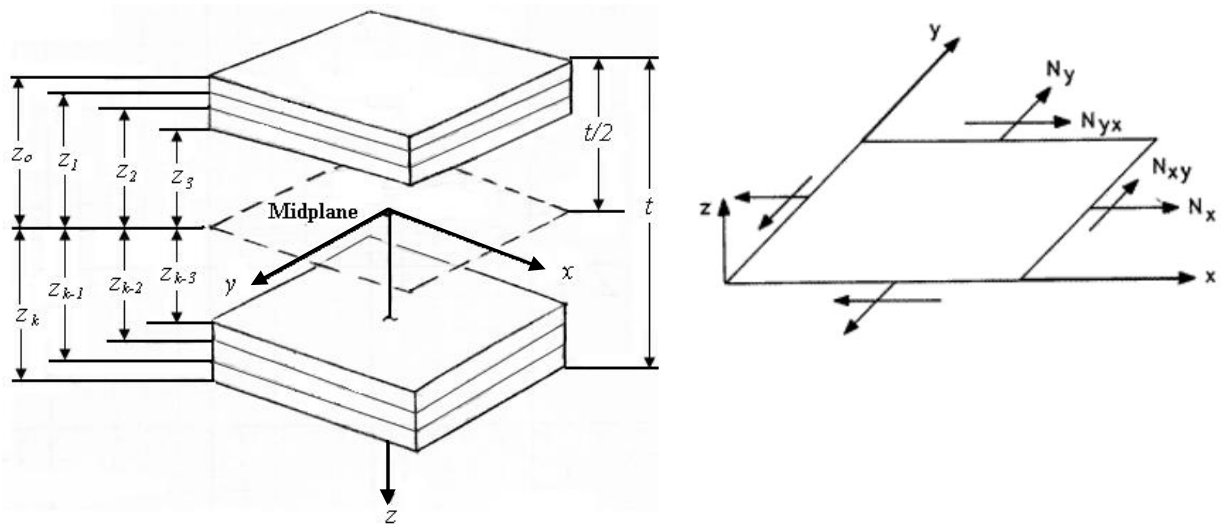
Figure 2-2: Ply Layup Definition and Applied Forces (Kriz, 2000)

The derivation is done Abbey (2009) and results in a final extensional in plane stiffness

$$\{N\} = \begin{bmatrix} A_{11} & A_{12} & A_{16} \\ A_{12} & A_{22} & A_{26} \\ A_{16} & A_{26} & A_{66} \end{bmatrix} \begin{Bmatrix} \varepsilon_x^o \\ \varepsilon_y^o \\ \gamma_{xy}^o \end{Bmatrix} \tag{2.11}$$

where $A_{ij} = \sum_{k=1}^{N} \left(\overline{Q}_{ij} \right)_k \left(Z_k - Z_{k-1} \right)$.

Out of plane forces can be considered in a similar fashion to obtain coupling stiffness and bending stiffness matrices.

2.2.5. Laminate Shorthand

The stacking shorthand for layups is [angle1/angle2/angle3….] or [0/90/45/-45/s] where s indicates symmetry. Layups can be either, balanced and symmetric, balanced only or neither balanced nor symmetric.

A symmetric layup is one where the layup is mirrored about the centre of the layup. Balanced layups require an equivalent negative and positive ply for each angle. The advantage of a balanced-symmetric layup is that the coupling effect in the coupling matrix is zero, greatly reducing computation time.

2.3. Probability

Probability is a branch of mathematics that deals with calculating the likelihood of a given event's occurrence. This makes it useful in dealing with uncertainty in design, manufacture and material properties. Uncertainty in material property values can be associated with probabilistic distributions and can be found to lie within confidence bounds. Material properties can follow a number of distributions including exponential, Weibull, lognormal extreme value and normal distributions. Normal distributions are undoubtedly the most widely used since test data like tensile test results often follow normal distributions (Montgomery and Runger, 2007).

2.3.1. Normal Distribution

A set of parameter values or numbers can be quantified by a distribution, a mathematical mean, standard deviation and coefficient of variance. The mean of a function μ is the mathematical average of a set of numbers. The standard deviation σ is a measure of how spread-out these numbers are. The coefficient of variance (COV) is used to measure dispersion and is the ratio of the standard deviation to the mean.

A linear function of normally distributed variables is also normally distributed (Montgomery, et al. 2007). An example of this is equation 2.12-2.13, relating two normally independent normal variables X_1 and X_2 (Montgomery, et al. 2007).

$$ Y = \frac{X_1}{X_2} \tag{2.12} $$

where: $X_1 \sim N\left(\mu_1, \sigma_1 \right)$ and $X_2 \sim N\left(\mu_2, \sigma_2 \right)$ such that

$$Y \sim N\left(\frac{\mu_1}{\mu_2}, \sqrt{\frac{\mu_1^2 \sigma_2^2 + \mu_2^2 \sigma_1^2}{\mu_2^4}}\right) \qquad (2.13)$$

Y is thus normally distributed with the mean $\frac{\mu_1}{\mu_2}$ and standard deviation $\sqrt{\frac{\mu_1^2 \sigma_2^2 + \mu_2^2 \sigma_1^2}{\mu_2^4}}$.

Unfortunately the distributions of the parameters are not always known or they may be non-linearly related to each other. In instances like these the Taylor series approximation can be used to determine the mean of Y from a function g

$$\mu_y \approx g\left(\mu_1, \mu_2, \ldots, \mu_n\right) \qquad (2.14)$$

and the standard deviation can be obtained from

$$\sigma_y^2 \approx \sum_{i=1}^{n} a_i^2 \sigma_i^2 + HOT \qquad (2.15)$$

where $a_i = \left.\dfrac{\partial g}{\partial x_i}\right|_{\mu_1, \mu_2, \ldots, \mu_n}$

2.3.2. Analytical Solution for the Standard Deviation of SDOF Resonance

At this point it is possible to derive an analytical solution for the standard deviation of the natural frequency ω_n of a single degree of freedom (SDOF) system as in equation 2.1.

The problem here is complicated by the square root. Thus by squaring both sides

$$\omega_n^2 = \frac{K}{M} \text{ or in terms of the mean } \mu_{\omega_n}^2 = \frac{\mu_K}{\mu_M} \qquad (2.16)$$

The standard deviation of the LHS of equation 2.16 $\dfrac{\mu_K}{\mu_M}$ is adapted from equation 2.13

$$\sigma_{\omega_n^2} = \sigma_{\frac{K}{M}} = \sqrt{\frac{\mu_k^2 \sigma_m^2 + \mu_m^2 \sigma_k^2}{\mu_m^4}} \qquad (2.17)$$

The Taylor series approximation is used to deal with the square on ω_n^2. From equation 2.15

$$\left(\sigma_{\omega_n^2}\right)^2 = a_1^2 \sigma_{\omega_n}^2 \qquad (2.18)$$

where $a_1 = \dfrac{\partial \mu_{\omega_n}^2}{\partial \mu_{\omega_n}} = 2\mu_{\omega_n}$

$$\therefore \sigma_{\omega_n^2} = \sqrt{4\mu_{\omega_n}^2 \sigma_{\omega_n}^2} \tag{2.19}$$

Finally by substituting equation 2.19 into the LHS of equation 2.17 and solving for the standard deviation of ω_n it is possible to obtain equation 2.20

$$\sigma_{\omega_n} = \frac{1}{2\mu_{\omega_n}\mu_m^2}\sqrt{\mu_k^2 \sigma_m^2 + \mu_m^2 \sigma_k^2} \tag{2.20}$$

This is a practical and simple analytical solution for the standard deviation of the natural frequency of a single degree of freedom system. A Monte-Carlo simulation was performed to test this equation and can be found in appendix A. The mean and standard deviation of the analytical solution matched that of the Monte-Carlo simulation. It is also noted that the solution follows a normal distribution.

In terms of a multi-degree of freedom (MDOF) system, the analytical solution becomes computationally tedious owing to the number of additional variable parameters and thus lengthy and difficult derivative calculations are required for Taylor's approximation. A practical solution to this is to directly apply Monte-Carlo simulation.

A Monte Carlo simulation was performed on a MDOF system and the solution of the natural frequency was found to follow a normal distribution. The results can be found in appendix A.

2.3.3. Confidence Bounds

It is possible to create confidence bounds on the mean of a population. This can be applied to define, with a percentage confidence, an interval that the natural frequencies of a system will fall in, or to define confidence bounds for mode shape deformation.

Montgomery, et al. (2007:271) defines the confidence interval on variance for a normal distribution as follows:

If $\bar{x}$ and s are the mean and standard deviation of a random sample from a normal distribution with unknown variance σ^2, a 100(1-α) % confidence interval on mean μ is given by

$$\bar{x} - t_{\alpha/2,n-1}s/\sqrt{n} \leq \mu \leq \bar{x} + t_{\alpha/2,n-1}s/\sqrt{n} \tag{2.21}$$

where $t_{\alpha/2,n-1}$ is the upper 100α/2 percentage point of the t distribution with n-1 degrees of freedom and read from tableA-3 in appendix A.

2.4. Model Updating

The main application of model updating is model validation. The common result of finite element modal analysis and modal testing is a set of modal parameters (resonance frequencies, damping and mode shapes) which characterize the linear dynamics of the structure. Ideally, the two techniques should yield the same results. In practice however, they rarely do. Model updating is a technique used to match finite element models to test data through an iterative optimization routine. This is done by adjusting the values of selected parameters such that a reference correlation coefficient is minimized (FEMtools, 2010). Most commonly used are the sensitivity-based iterative methods because they provide the highest level of control on the choice of updating parameters and targets and allowing physical interpretation of the updating results (Lauwagie, et al. 2002c).

2.4.1. General Model Updating Procedure

Finite element model updating can be used to identify structural or material properties if they are selected as global updating parameters in an inverse method. In FEMtools, parameters can be selected as local or global. Local means that each element in the FEM models is allowed to update the selected parameters independently. Global on the other hand keeps the parameters universal properties and is thus necessary for material identification.

Figure 2-3 shows the general flowchart of the inverse method to identify elastic material properties. Initial values for the elastic material properties are estimated and introduced into the FE model of the test specimen in order to compute the numerical responses.

Improved material properties can be obtained from the differences between the experimental and numerical responses and response sensitivities by solving the following least-squares problem (FEMtools, 2010)

$$\{\Delta p\} = \left[S_n \right]^{\dagger} \{\Delta f\} \tag{2.22}$$

where
$$\Delta p = \frac{p_{new} - p_{old}}{p_{old}}, \Delta f = \frac{f_{\exp} - f_{FEM}}{f_{\exp}}, \text{ and}$$

$$S_n = \begin{bmatrix}
\dfrac{\partial f_1}{\partial E_x}\dfrac{E_x}{f_1} & \dfrac{\partial f_1}{\partial E_y}\dfrac{E_y}{f_1} & \dfrac{\partial f_1}{\partial G_{xy}}\dfrac{G_{xy}}{f_1} & \dfrac{\partial f_1}{\partial \upsilon_{xy}}\dfrac{\upsilon_{xy}}{f_1} \\[2.5ex]
\dfrac{\partial f_2}{\partial E_x}\dfrac{E_x}{f_2} & \dfrac{\partial f_2}{\partial E_y}\dfrac{E_y}{f_2} & \dfrac{\partial f_2}{\partial G_{xy}}\dfrac{G_{xy}}{f_2} & \dfrac{\partial f_2}{\partial \upsilon_{xy}}\dfrac{\upsilon_{xy}}{f_2} \\[2.5ex]
\vdots & \vdots & \vdots & \vdots \\[2.5ex]
\dfrac{\partial f_m}{\partial E_x}\dfrac{E_x}{f_m} & \dfrac{\partial f_m}{\partial E_y}\dfrac{E_y}{f_m} & \dfrac{\partial f_m}{\partial G_{xy}}\dfrac{G_{xy}}{f_m} & \dfrac{\partial f_m}{\partial \upsilon_{xy}}\dfrac{\upsilon_{xy}}{f_m}
\end{bmatrix} \tag{2.23}$$

where *P* denotes a material property, *f* denotes a response and † denotes the pseudo inverse of a matrix.
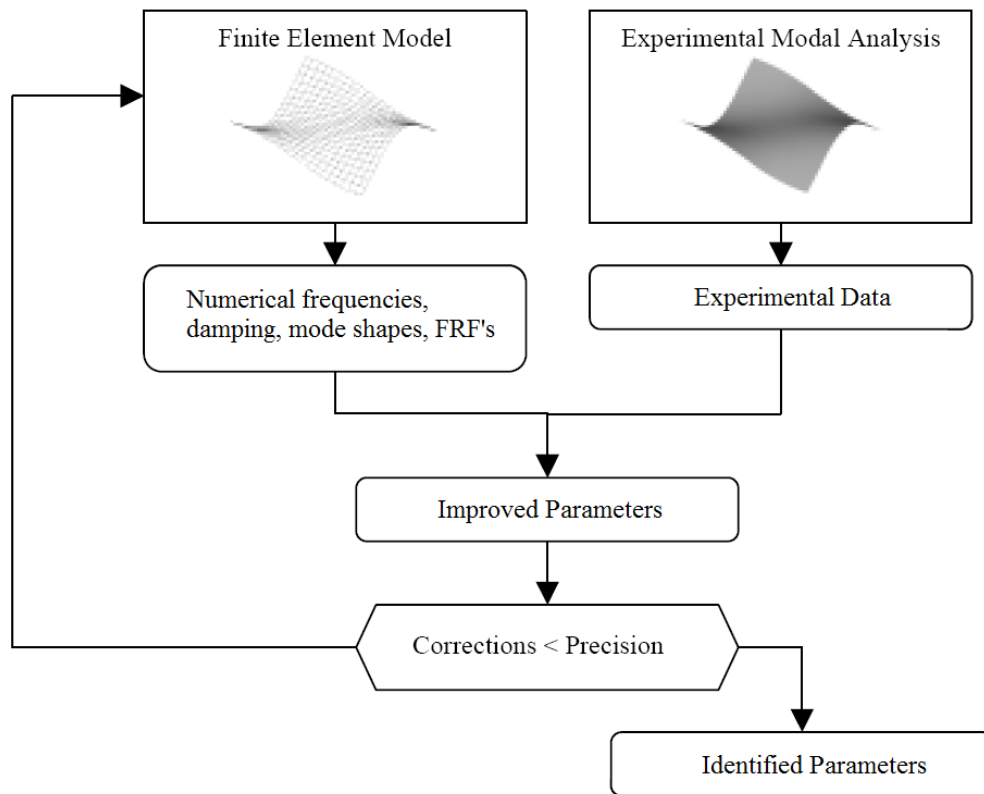
Figure 2-3: Model Updating Flow Diagram, (Lauwagie, et al. 2002c)

Note that the sensitivity matrix S_n in equation (2.23) is composed with normalised relative sensitivities. There are two distinct reasons to prefer normalised relative sensitivities over classical absolute sensitivities. Absolute sensitivities of the frequencies with respect the Young's modulus vary a few orders of magnitude from those of Poisson's ratio, while this is not the case for relative sensitivities. Therefore the sensitivity matrix with relative sensitivities will be better conditioned, leading to an increased stability of the updating routine. By normalising the sensitivities, i.e. dividing them by the relevant response, the least-squares solution (2.32) of the updating routine will minimise the relative differences between the numerical and experimental frequencies. If absolute sensitivities were used, the least-squares routine would minimise the absolute frequency differences, indirectly giving the high order modes a higher weight (Lauwagie, 2002c).

If the corrections of the material properties resulting from (2.22) are larger than the desired precision, the improved material properties are introduced into the FE-model and a new iteration is started. If the responses of the FE-model of the last iteration match the experimental responses, the material properties of the test specimen have been identified.

2.4.2. Correlation Analysis

Modal correlation analysis is the technique to quantitatively and qualitatively examine the correspondences and differences between analytically and experimentally obtained modal parameters. Correlation between any analytically and experimentally obtained responses can

be analyzed. FEMtools allows correlation for mode shapes but also static and operational shapes, and FRFs.

Global mode shape correlation methods like visual inspection, numerical mode shape correlation like modal assurance criterion and eigen-vector orthogonality can be used to compute a quantity that expresses the level of correlation (FEMtools, 2010:26).

MAC is a measure of the squared cosine of the angle between two mode shapes. To compute the MAC between an analytical (index a) and experimental mode shape (index e), the following equation is used

$$\mathrm{MAC}(\psi_a, \psi_e) = \frac{\left|\{\psi_a\}^t \{\psi_e\}\right|^2}{\left(\{\psi_a\}^t \{\psi_a\}\right)\left(\{\psi_e\}^t \{\psi_e\}\right)} \tag{2.24}$$

The MAC between all possible combinations of analytical and test modes are stored in the MAC-matrix. The off-diagonal terms of the MAC-matrix provide a means to check linear independence between modes. Two mode shapes with a value equal to 1 indicate identical modes (or perfect correlation). MAC-values are calculated by multiplying numerically and experimentally obtained modal displacements at paired DOFs.

Several correlation coefficients can be computed. They are either based on the errors on individual modal parameters selected as responses (resonance frequencies, modal displacements), global correlation information (MAC) or other response data like mass. The different components are weighted with respect to each other by using the expected relative error C_{Ri} on the response value. For example, the default expected relative error on experimental resonance frequencies is 1%.

A standard objective function for the average MAC values (MACMEAN) is given by

$$CC = 1 - \frac{1}{N}\sum_{i=1}^{N} C_{Ri} MAC_i \tag{2.25}$$

This is the average margin of the MAC-values for the paired mode shapes that correspond with N resonance frequencies selected as responses. Further correlations available in FEMtools can be found in appendix B.

2.4.3. Parameters

The functional relationship between the modal characteristics and the structural parameters can be expressed in terms of a Taylor series expansion limited to the linear term. This expansion is usually underdetermined and can be solved using a pseudo-inverse (least squares), weighted least squares or the Bayesian technique, depending on whether weighting coefficients are added or not.

In order to avoid physically impossible updated parameter values, it is possible to apply lower and upper bounds. When parameter constraints are defined, it is possible that convergence cannot be obtained to a satisfactory degree. A trade-off between physically acceptable parameter values and convergence level is then required.

2.4.4. Multi-Model Updating

Test data are usually modally and spatially truncated, and raw test data is often polluted by noise. As a result, the model updating procedure requires the solution of a highly underdetermined system of equations, i.e. the target responses can be obtained via an infinite number of combinations of updating parameter changes. However, applications like material identification require a unique solution. Materials like composite laminates require even more target responses owing to multiple types of materials that could be used in a single layup. Responses like resonant frequencies only contain information about overall stiffness and not about individual layer contribution.

The solution of an inverse identification procedure to identify the elastic properties of the layers of one single sample will not be unique, and thus meaningless. This is concluded from observing the sensitivity matrix of the inverse problem. Note that the number of materials that are used in the different layers determines the number of unknown parameters and not the number of plies. Thus in 2.26 the number of block columns of the sensitivity matrix equals the number of materials used and not the number of material layers.

$$S_n = \begin{bmatrix} \overbrace{\dfrac{\partial f_1}{\partial E_{x,1}}\dfrac{E_{x,1}}{f_1} & \dfrac{\partial f_1}{\partial E_{y,1}}\dfrac{E_{y,1}}{f_1} & \dfrac{\partial f_1}{\partial G_{xy,1}}\dfrac{G_{xy,1}}{f_1} & \dfrac{\partial f_1}{\partial \upsilon_{xy,1}}\dfrac{\upsilon_{xy,1}}{f_1}}^{\text{Material 1}} & \overbrace{\dfrac{\partial f_1}{\partial E_{x,n}}\dfrac{E_{x,n}}{f_1} & \dfrac{\partial f_1}{\partial E_{y,n}}\dfrac{E_{y,n}}{f_1} & \dfrac{\partial f_1}{\partial G_{xy,n}}\dfrac{G_{xy,n}}{f_1} & \dfrac{\partial f_1}{\partial \upsilon_{xy,n}}\dfrac{\upsilon_{xy,n}}{f_1}}^{\text{Material n}} \\ \dfrac{\partial f_2}{\partial E_{x,1}}\dfrac{E_{x,1}}{f_2} & \dfrac{\partial f_2}{\partial E_{y,1}}\dfrac{E_{y,1}}{f_2} & \dfrac{\partial f_2}{\partial G_{xy,1}}\dfrac{G_{xy,1}}{f_2} & \dfrac{\partial f_2}{\partial \upsilon_{xy,1}}\dfrac{\upsilon_{xy,1}}{f_2} & \cdots & \dfrac{\partial f_2}{\partial E_{x,n}}\dfrac{E_{x,n}}{f_2} & \dfrac{\partial f_2}{\partial E_{y,n}}\dfrac{E_{y,n}}{f_2} & \dfrac{\partial f_2}{\partial G_{xy,n}}\dfrac{G_{xy,n}}{f_2} & \dfrac{\partial f_2}{\partial \upsilon_{xy,n}}\dfrac{\upsilon_{xy,n}}{f_2} \\ \vdots & \vdots & \vdots & \vdots & & \vdots & \vdots & \vdots & \vdots \\ \dfrac{\partial f_m}{\partial E_{x,1}}\dfrac{E_{x,1}}{f_m} & \dfrac{\partial f_m}{\partial E_{y,1}}\dfrac{E_{y,1}}{f_m} & \dfrac{\partial f_m}{\partial G_{xy,1}}\dfrac{G_{xy,1}}{f_m} & \dfrac{\partial f_m}{\partial \upsilon_{xy,1}}\dfrac{\upsilon_{xy,1}}{f_m} & & \dfrac{\partial f_m}{\partial E_{x,n}}\dfrac{E_{x,n}}{f_m} & \dfrac{\partial f_m}{\partial E_{y,n}}\dfrac{E_{y,n}}{f_m} & \dfrac{\partial f_m}{\partial G_{xy,n}}\dfrac{G_{xy,n}}{f_m} & \dfrac{\partial f_m}{\partial \upsilon_{xy,n}}\dfrac{\upsilon_{xy,n}}{f_m} \end{bmatrix}$$

(2.26)

The linear dependency of the columns of the sensitivity matrix can be interpreted in the following way. A variation of $E_{x,1}$ may change the different responses in the same way as a variation of $E_{x,n}$. Therefore, a change of $E_{x,1}$ can be completely compensated by an appropriate adaptation of $E_{x,n}$, and the FE-model with the adapted material properties will have exactly the same responses as the initial FE-model. Eventually, this mechanism will result in an infinite number of possible solutions for the inverse problem.

The non-uniqueness of the solution can be solved by using responses measured on a number of test samples with different layer geometry. In each of the responses, the contribution of the different layers will be different, making it possible to separate the measured overall stiffness into the desired layer stiffness. In the case of layered materials, the single model updating

routine of the standard material identification procedure has to be replaced by a multi-model updating routine as developed by Lauwagie, et al. (2002c).

The global sensitivity matrix of this multi-model procedure is presented in equation (2.27), and contains one block column for every different material used in the samples, and one block row for every tested sample (or FE model). The improved material properties are still obtained with equation (2.22).

$$
S_n = \begin{bmatrix}
\begin{array}{c} model-1 \end{array}\begin{cases}
\begin{array}{ccc}
\overbrace{\dfrac{\partial f_{1,1}}{\partial E_{x,1}}\dfrac{E_{x,1}}{f_{1,1}} & \cdots & \dfrac{\partial f_{1,1}}{\partial \nu_{xy,1}}\dfrac{\nu_{xy,1}}{f_{1,1}}}^{Material-1} \\
\vdots & \ddots & \vdots \\
\dfrac{\partial f_{m,1}}{\partial E_{x,1}}\dfrac{E_{x,1}}{f_{m,1}} & \cdots & \dfrac{\partial f_{m,1}}{\partial \nu_{xy,1}}\dfrac{\nu_{xy,1}}{f_{m,1}}
\end{array}
\end{cases} & \cdots &
\begin{array}{ccc}
\overbrace{\dfrac{\partial f_{1,1}}{\partial E_{x,n}}\dfrac{E_{x,n}}{f_{1,1}} & \cdots & \dfrac{\partial f_{1,1}}{\partial \nu_{xy,n}}\dfrac{\nu_{xy,n}}{f_{1}}}^{Material-n} \\
\vdots & \ddots & \vdots \\
\dfrac{\partial f_{m,1}}{\partial E_{x,n}}\dfrac{E_{x,n}}{f_{m,1}} & \cdots & \dfrac{\partial f_{m,1}}{\partial \nu_{xy,n}}\dfrac{\nu_{xy,n}}{f_{m,1}}
\end{array} \\[2em]
\vdots & \ddots & \vdots \\[1em]
\begin{array}{c} model-k \end{array}\begin{cases}
\begin{array}{ccc}
\dfrac{\partial f_{1,k}}{\partial E_{x,1}}\dfrac{E_{x,1}}{f_{1,k}} & \cdots & \dfrac{\partial f_{1,k}}{\partial \nu_{xy,1}}\dfrac{\nu_{xy,1}}{f_{1,k}} \\
\vdots & \ddots & \vdots \\
\dfrac{\partial f_{m,k}}{\partial E_{x,1}}\dfrac{E_{x,1}}{f_{m,k}} & \cdots & \dfrac{\partial f_{m}}{\partial \nu_{xy,1}}\dfrac{\nu_{xy,1}}{f_{m,k}}
\end{array}
\end{cases} & \cdots &
\begin{array}{ccc}
\dfrac{\partial f_{1,k}}{\partial E_{x,n}}\dfrac{E_{x,n}}{f_{1,k}} & \cdots & \dfrac{\partial f_{1,k}}{\partial \nu_{xy,n}}\dfrac{\nu_{xy,n}}{f_{1,k}} \\
\vdots & \ddots & \vdots \\
\dfrac{\partial f_{m,k}}{\partial E_{x,n}}\dfrac{E_{x,n}}{f_{m,k}} & \cdots & \dfrac{\partial f_{m}}{\partial \nu_{xy,n}}\dfrac{\nu_{xy,n}}{f_{m,k}}
\end{array}
\end{bmatrix}
$$

(2.27)

3. Manufacturing, Specifications and Materials Testing

This chapter includes two main aspects of this dissertation, manufacture and destructive materials testing. Both Fibrelam and the composite UAV wings specifications are presented and structural material properties are attained through tensile testing and retrieved, when available, from materials data sheets.

3.1. Manufacturing

Unique to the composites industry is the ability to create a product from many different manufacturing processes. Each of the fabrication processes has characteristics that define the type of products to be produced. Many techniques exist for the production of composites and laminates including hand layup, resin transfer moulding (RTM), Vacuum assisted transfer moulding (VARTM), pultrusion, filament winding and autoclave moulding.

The most efficient manufacturing process for a composite product takes into consideration user needs, performance requirements, product size, surface complexity, appearance production rate and volume, materials tooling and equipment (Shook, 1986).The main process considered here is autoclave moulding for the production of laminates.

Autoclave moulding is a modification of pressure-bag and vacuum-bag moulding. This advanced composite process produces denser, void free mouldings because higher heat and pressure are used for curing. Autoclave size however limits component size (Rosato, 1997).

3.1.1. Fibrelam Sandwich Panels

Fibrelam 1200 panels were obtained from Aerosud Pty Ltd. in cut panel sizes of 1000×200 mm, as an easily accessible composite component, for initial familiarization and testing. After vibration testing, the panels where cut to 520×200 mm and re-tested for multi-model updating purposes. Fibrelam 1200 is a sandwich panel designed for use in aircraft interior furnishing structures such as galleys, partitions and stowage compartments (Hexcel, 2010).

Fibrelam 1200 comprises an aramid honeycomb core bonded between woven [0/90] glass fibre/phenolic composite skin weaves as presented in figure 3-1. The panel used for testing in this dissertation has a grade 6 honeycomb core of 48 kg/m^{3}and 3 mm cell size.
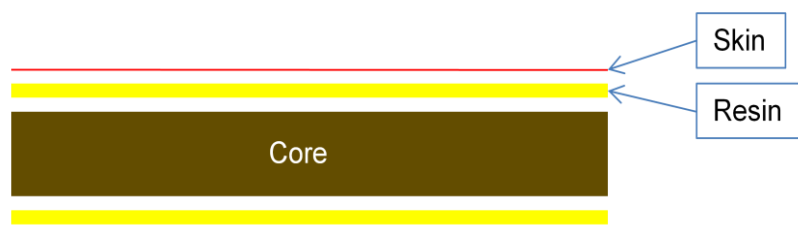
Figure 3-1: Fibrelam 1200 Construction

3.1.1.1.   Fibrelam Skins

A long beam flexure test (figure3-2) performed by the manufacturer of the panels can provide information about the lengthwise skin elastic modulus $E_{x, skin}$ of the panel:

$$E_{x,skin} = \frac{11Ps^3}{384dwt(h-t)^2}$$

(3.1)
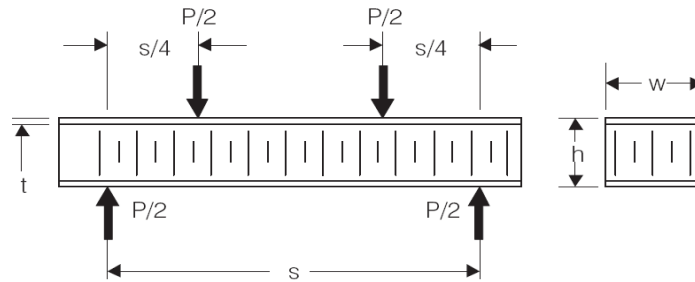
Figure 3-2: Long Beam Flexure-test on Fibrelam 1200 (Hexcel, 2007a)

Component size values for the flexure test are standard and are presented in table 3-1with the measured results (Hexcel, 2007a). $E_{x, skin}$ is calculated from equation 3.1 to be 16.46 GPa. This is a good indication of the result that can be expected from tensile tests performed on the skin.

Table 3-1: Flexure-test Standard Values

Grade 6 Fibrelam 1200			
Parameter	**Symbol**	**Value**	**Unit**
Span	s	508	mm
Load	P	445	N
Mid-span deflection	d	13	mm
Skin thickness	t	0.7	mm
Panel width	w	76	mm
Panel thickness	h	12.8	mm

Unfortunately other material properties like transverse elastic modulus ($E_{y, skin}$) and poisons ratio are difficult to obtain, and if available are still to be used with caution. Thus tensile testing was necessary to obtain reliable skin properties. The resin used to bond the skin and core is also difficult to remove from the skin before tensile testing and is thus assumed part of the skin.

3.1.1.2.   Fibrelam Core

Honeycomb cores are modelled according to the classical laminate theory in this dissertation as a simplification because the purpose of the Fibrelam analysis is for familiarization with composites. Honeycomb is however a very complicated material to model accurately and is the centre of research of many paper publications like that of Pan, Wu and Sun (2008) investigating the shear modulus and strength of honeycomb cores.

Honeycomb (A1-48-3) used for Fibrelam 1200 is a non-metallic honeycomb manufactured from high temperature resistant aramid paper formed into honeycomb structure, and coated with a phenolic resin. The combination of aramid paper and phenolic resin gives type A1 its superior strength, toughness and chemical resistance. The honeycomb cell shape is normally hexagonal for optimum mechanical properties. It can also be over expanded to produce a rectangular cell shape and provide improved drape ability for the production of curved parts (Hexcel, 2007b).

Hexcel provide datasheets for their honeycomb products that include 2D orthotropic elastic moduli, in a ribbon and expansion direction as in figure 3-3.
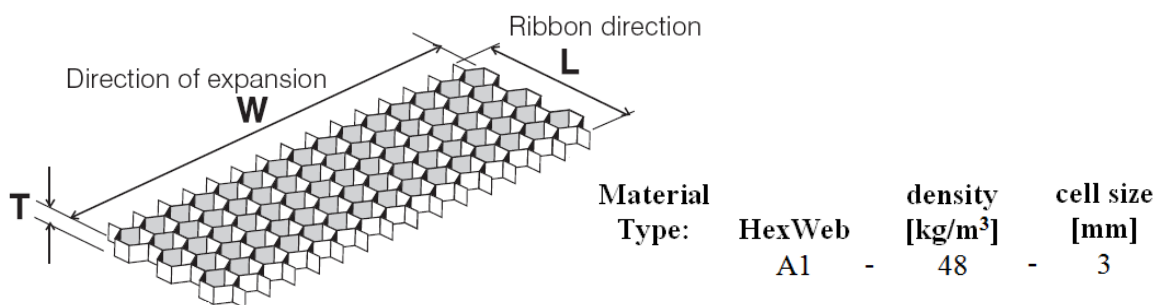
Figure 3-3: Honeycomb Core Material Description, (Hexcel, 2007b:3)

A1-48-3 has an elastic modulus of 0.04 GPa in the Ribbon direction and 0.025 GPa in the expansion direction (Hexcel, 2007b:2). Table 3-2 gives the 2D orthotropic material properties for the honeycomb.

Table 3-2: Honeycomb 2D Orthotropic Properties

Elastic Moduli [GPa]			Poisson	Density [kg/m^3]
E_1	E_2	G_{12}	v_{12}	ρ
0.04	0.025	0.01	0.2	48

3.1.2. Composite Wings

The composite wing designed by the CSIR and manufactured by Lightweight Structures Technology, is comprised of three materials; a pre-preg skin is bonded together using resin beading at the leading and trailing edges and to a foam spar near the leading edge. A cross-section of the design is presented in figure 3-4.

FT109 Glass Pre-preg Skin   2022 + Qcell Resin Beading

2202 + Qcell Resin Beading   Roha-cell Foam Spar

Figure 3-4: Composite Wing Construction

The centre of the spar was placed 52.5mm from the leading edge and is 19×35mm in dimension. The wing has a symmetric SD 8020 airfoil with a 210mm cord and is 1200mm in length. Wing dimensions were limited by autoclave size.

3.1.2.1. Wing Material Specifications

The skin of the wing is a 280gsm glass [0/90] pre-preg weave with FT109 Resin system (Epo, 2006) and black in colour. This pre-preg resin system is developed for industrial applications where mostly wet laminating system is used. FT 109 pre-pregs are dispatched under dry ice or by refrigerated transport. After the date of dispatch the pre-pregs can be stored at -18 °C for a period of at least 12months. Before processing, the pre-preg rolls, in their protective sheets, have to be conditioned to room temperature. In this context it is absolutely necessary to avoid the formation of condensation water directly on the pre-pregs. At room temperature (ca. 20 °C) the pre-pregs remain processable for 70 days.

The spar is manufactured from low density foam called Roha-cell. Roha-cell is a closed-cell rigid expanded plastic material for lightweight sandwich construction. It has excellent mechanical properties, high dimensional stability under heat, solvent resistance and low thermal conductivity. The strength and moduli values are the highest for any foamed plastic in its density range.

Roha-cell is manufactured by the hot forming of methacrylic acid/methacrylonitrile copolymer sheets. During foaming this copolymer is converted to polymethacrylimide. The foam has a density of 75.3 kg/m^{3}and an elastic modulus of 0.0903 GPa (Roha-cell, 2010).

The resin used for bonding the skins and the spar together is Epolam 2022 combined with Qcell hardener. It has an estimated cured density of 1170 kg/m3 and an elastic modulus of 3.4 GPa (Axson Technologies, 2008).

3.1.2.2. Wing Manufacturing Process

Six wings were manufactured in total of which three were embedded with mock delaminations and three were undamaged. The process was as follows: The top and bottom skins of the wing were individually manufactured in moulds in an autoclave cycle process, after which they were bonded together with the spar in place. A mould for the SD8020 airfoil was borrowed from the CSIR. Each skin was moulded in an open mould using a vacuum bag process. The process of skin manufacture was as follows:

- Mould Preparation - The mould was first prepared with Loctite PMC Frekote cleaning agent after which a release agent (Loctite 770-NC Frekote) was applied to prevent the layup sticking to the mould during curing.

- Skin Layup - It comprises a four ply symmetric layup [45/0/$_s$] or considering the weave [45/-45/0/90/$_s$]. The four layers of the skin were cut and laid on the mould. The

45° ply was placed first followed by two 0° plies and then another 45° ply. The product data sheet (PPS) can be found in appendix C.

- Vacuum Bagging - A layer of Nylon based peel ply was placed on top of the skin layup in order to keep the surface even and the top fibres together, keep the skin clean, absorb excess resin and provide a matt finish for a better bonding surface to the spar. A layer of release film (non-adhesive plastic layer) was laid over the peel ply after which, a layer of "breather cloth" was then laid.

  The release film stops resin from sticking to the breather cloth. The purpose of this cloth is to allow air to escape easily during vacuum bagging. Finally a layer of plastic (the vacuum bag) was placed over the layup and taped to the mould as to create a seal over the entire layup, as in figure 3-5. The air was then vacuumed out of the mould and checked for leaks.
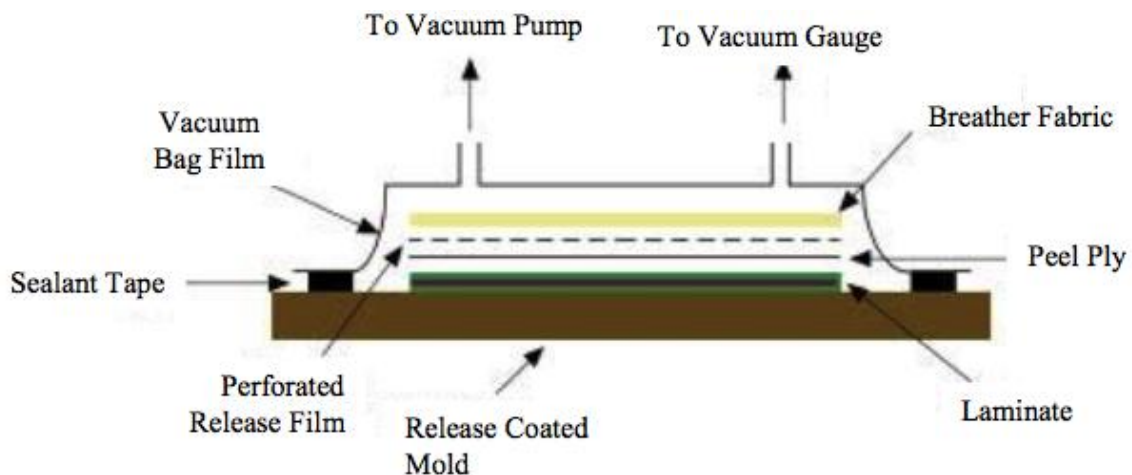
Figure 3-5: Vacuum Bag Configuration (Carbonfiberdiy, 2011)

- Autoclave- The next step was to place the mould into an autoclave oven for curing. To allow for even heating, the oven was heated to 90°C over a period of 10 minutes where it remained for a further 30 minutes. The oven was then heated to 120° over another period of 10 minutes and remained at this temperature for 2 hours.

  The entire process was performed under a controlled oven pressure of 3bar. Each skin, top and bottom, had to go through the process separately due to the limited size of the autoclave.

- Bonding - Once cured, the vacuum bagging and addition layers of cloth were removed. The edges of each skin, top and bottom, were sanded and prepared for bonding. The spar was cut to size and placed on the inside of the bottom skin, which was still in the mould. Beads of resin were laid in position (figure 3-6) after which the top skin, still in the mould, was placed over the bottom skin and spar as to enclose the wing in its final shape. The two moulds were then bolted together and the wing left to dry for 24 hours.

After vibration testing the wings where cut to lengths of 275 mm and re-tested, thereafter they were cut again to lengths of 225 mm and again re-tested for multi-model updating purposes.
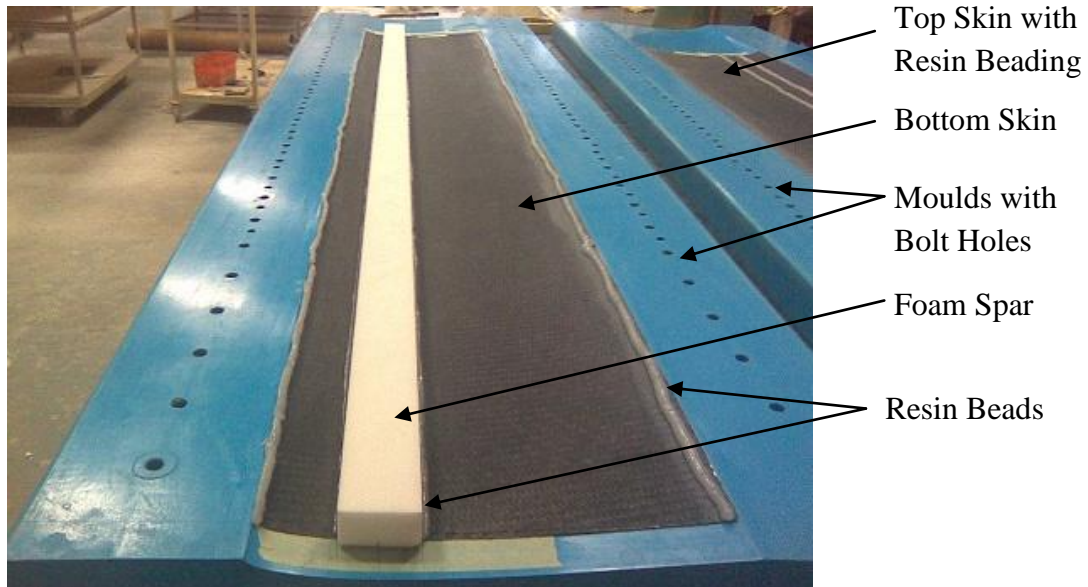
Figure 3-6: Resin Beading on the Skin and Spar

3.1.3. Manufacturing Delamination

The initial intention was to embed a layer of release film between the layers of the skin with the purpose of preventing bonding between these layers, as to form a mock delamination. The delamination, owing to stock shortage and innovation on behalf of the manufacturer, was then simulated by coating a layer of vacuum bagging plastic with the releasing agent (Frekote) and placing it between the plies of the skin layup. Figure 3-7 shows the mock delamination placed in position during the layup.
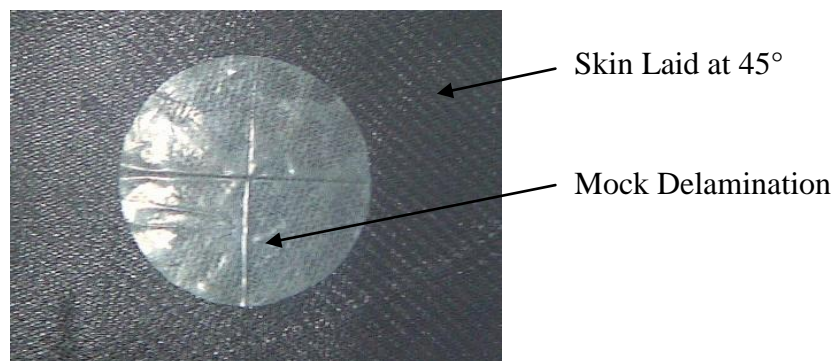
Figure 3-7: Mock Delamination

Three damaged wings were manufactured by embedding them with a delamination in the lay-up. Delamination size was increased with each wing. The delaminations were placed between the inner two layers of the skin i.e. [45°/0°/0°/delamination/45°] where the first 45° ply is the outside layer of the skin of the wing. The purpose of this is to remove the delaminations from

the location of peak bending shear, by avoiding the neutral axis (figure 3-8), as not all delaminations may occur at this convient location but still need to be detected.
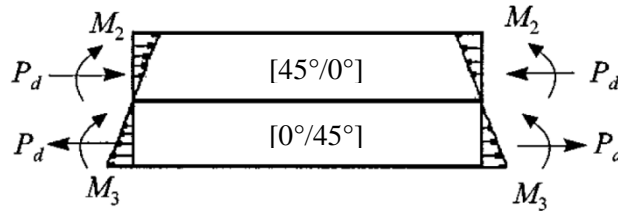
Figure 3-8: Bending Neutral Axis, (Zou, et al. 2000:362)

Figure 3-9 depicts the geometry of the delamination position and sizes. Dimensions are in millimetres.
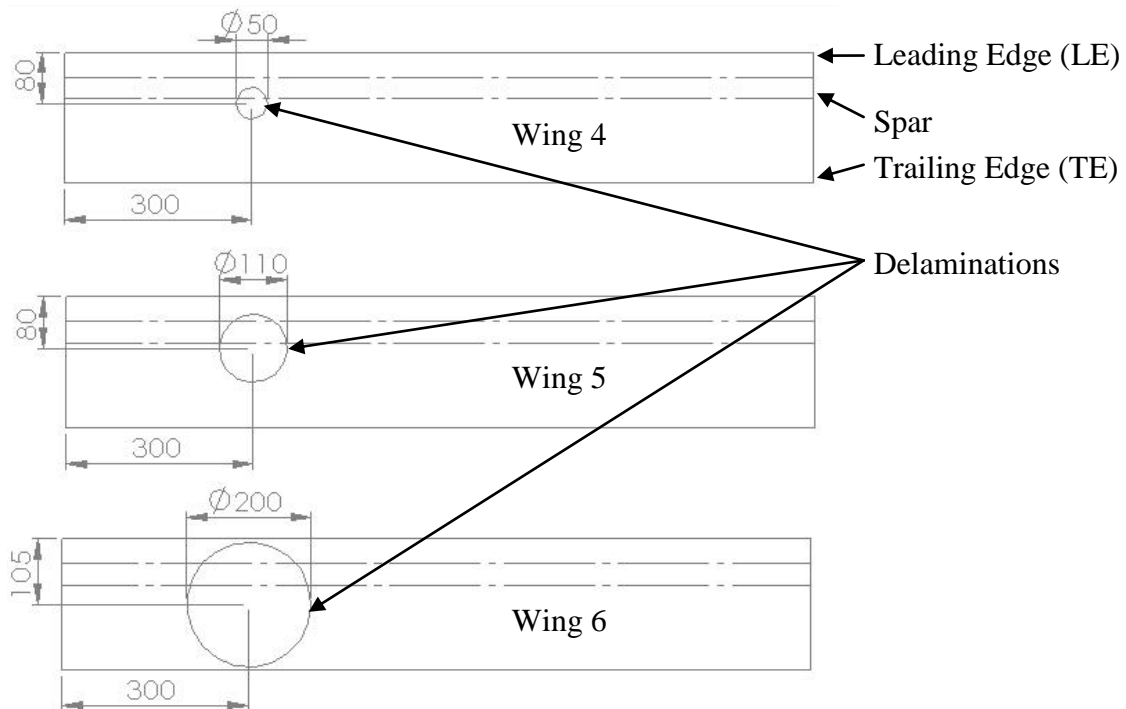
Figure 3-9: Delamination Positioning and Sizes

3.1.4. Wing Geometry Uncertainty

Several structural uncertainties arise as a result of repeatability issues during manufacturing. Apart from those of material properties, considered in this dissertation, many geometrical uncertainty issues have surfaced. These pertain mainly to tolerance of component placement, finishing work and application of resin quantity. In order to demonstrate these points, four wings were cut in cross-section to easily display the wing profiles. Consider first figure 3-10 depicting the leading edges of the wings.

- Component Placement Tolerance - Immediately noticeable in figure 3-10 is the variance in distance that the spars are placed from the leading edge d_n. This uncertainty will present variance in the structural stiffness across the chord length of the profile.

- Foam Spar Finishing - Another repeatability issue is the finishing of the leading edge corners of the foam spars. Note that the spar corners for wings 1, 3 and 4 are filleted but not so for wing 2. The idea behind the taper of the spar was to prevent interference

with the aerofoil profile, and as a result uses more resin beading, but this has clearly become an inconsistency.
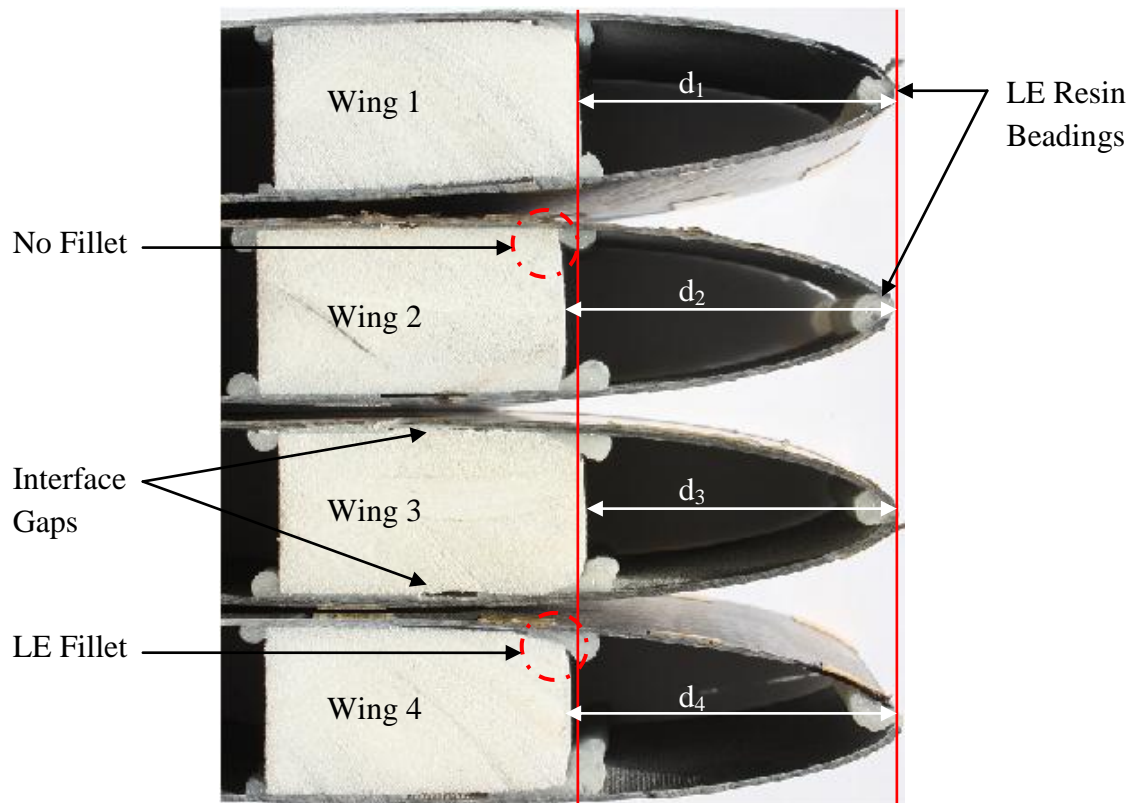
Figure 3-10: Leading Edge Geometrical Uncertainty

- <u>Spar-Skin Interface</u> - The interface between the spars and the skins is that of resin beadings. This interface is however not present along the entire width of the spars i.e. there are gaps left in the interface. The effect of such a gap is likely one of damping. These gaps are also not consistently the same size between wings and in fact vary greatly along the length of the wings as well.

- <u>Resin Beading Quantity Tolerance</u> - Finally in figure 3-10 and 3-11 it is noted that the quantity of resin applied for each beading is significantly different. It is also noted that the quantity varies along the length of the leading edges too. The result is varying mass and stiffness distribution in the beadings as depicted by the clearly visibly size difference in beading cross-section.

Figure 3-11: Trailing Edge Resin Uncertainty

Although it is possible to update a FE model to accommodate geometrical differences for a specific wing in question, it is an entirely different story to create and introduce a

probabilistic distribution of geometrical variance. As is noted later, the effect of the isotropic material property variances (resin beads and foam spar) is insignificant in relation to that of the orthotropic skins for these wings. Also, the gap left in the interface is not likely a problem faced by UAV wings in service but rather a design flaw inherent specifically to these wings.

For these reasons it was decided to treat these uncertainties in a deterministic manner. By measuring all geometrical uncertainties and using and an average value in FEM application, the geometrical uncertainty was considered resolved but still kept in mind when discussing results.

3.2. Destructive Experimental Testing

The Sasol labs at the University of Pretoria are equipped with advanced and precise measuring equipment making quality testing easily accessible to students. The latest in the arsenal of equipment is a state of the art Digital Image Correlation System (DICS) which captures digital images to evaluate full field strain patterns. Amongst other equipment, there is also a Polytec Scanning Laser Vibrometer that precisely measures vibration responses for evaluation of FRFs and modal analysis.

Tensile testing is considered in this chapter to determine material properties used to develop FE models and create a probabilistic material database. These tests are performed on both Fibrelam panels and Composite UAV wings.

Owing to variability of composite material properties, data sheet information should always be treated with caution. In fact, it is best to perform your own tests to determine the material properties. This is however not a trivial task, especially when dealing with composites. Fortunately ASTM D 3039 and ASTM D 3518 provide standard test methods for tensile and shear properties of composite materials respectively. For the purposes of this dissertation, it is necessary to determine the elastic moduli E_1, E_2, shear modulus G_{12}, Poisson's ratio ν_{12} and density ρ of 2D orthotropic materials.

3.2.1. ASTM D 3039 Specifications

ASTM D 3039 is a test method to determine the in-plane tensile properties of polymer matrix composites reinforced by high-modulus fibres. A thin flat strip of material having a constant rectangular cross section is mounted in the grips of a mechanical testing machine and monotonically loaded in tension while recording load. If the coupon strain is monitored then the stress-strain response of the material can be determined, from which the tensile modulus of elasticity and Poisson's ratio can be derived. Tensile test were therefore performed on the laminate skins of the Fibrelam panels and the UAV wing pre-preg skins.

Typical hazards of tensile testing composite laminates include:

- Material and Specimen Preparation- Poor material fabrication practices, lack of control of fibre alignment, and damage induced by improper coupon machining are known causes of high material data scatter in composites.

- <u>Gripping</u> - A high percentage of grip-induced failures, especially when combined with high material data scatter, is an indicator of specimen gripping problems.

- <u>System Alignment</u>- Excessive bending will cause premature failure, as well as highly inaccurate modulus of elasticity determination. Bending may occur as a result of misaligned grips or from specimens themselves if improperly installed in the grips or out-of-tolerance caused by poor specimen preparation.

- <u>Edge Effects</u>- Premature failure and lower stiffness's are observed as a result of edge softening in laminates resulting in high edge stresses and failure. Because of this, the strength and modulus can be drastically underestimated.

Design of mechanical test coupons (figure 3-12), especially those using end tabs, remains to a large extent an art rather than a science, with no industry consensus on how to approach the engineering of the gripping interface. The key factor in the selection of specimen tolerances and gripping methods is the successful introduction of load into the specimen and the prevention of premature failure as a result of a significant discontinuity. It was found, through trial and error, that 1.5mm thick aluminium tabs resulted in acceptable failure modes that occurred with reasonable frequency for both Fibrelam and the composite wing skins.
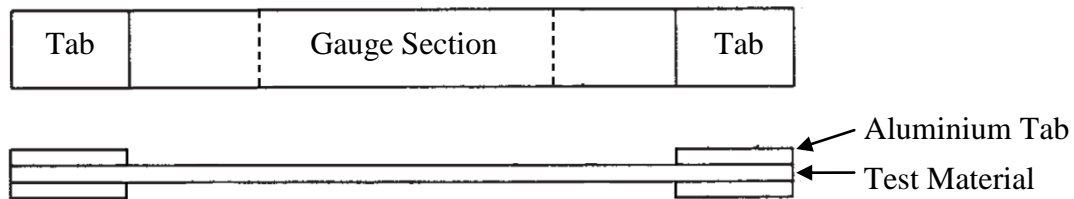
Figure 3-12: Test Coupon Configuration

The specimen width and thickness is selected to promote failure in the gauge section and assure that the specimen contains a sufficient number of fibres in the cross section to be statistically representative of the bulk material. The gage section is kept as far from the grips as reasonably possible and provides a significant amount of material under stress and therefore produces a more statistically significant result. The gauge section is typically considered to start a tabs length away from the tabs at each end.

The mode of failure is defined as a 3 character code presented in table3-3.

Table 3-3: Failure Mode Code

1st Character		2nd Character		3rd Character	
Failure Type	Code	Failure Area	Code	Failure Location	Code
Angled	A	Inside grip/tab	I	Bottom	B
Edge Delamination	D	At grip/tab	A	Top	T
Grip/Tab	G	<1W from grip/tab	W	Left	L
Lateral	L	Gauge	G	Right	R
Mulit-mode	M(xyz)	Multiple areas	M	Middle	M
Long/Splitting	S	Various	V	Various	V
Explosive	X	Unknown	U	Unknown	U
Other	O				

The standards specify that at least five specimens per test condition should be tested unless valid results can be gained through the use of fewer specimens.

Figure 3-13 presents a typical and acceptable failure mode. Figure 3-14 shows a failure outside the gauge section and data from a test like this should be considered with caution. The failure in figure 3-15is inside the grip and the data from this test cannot be used.
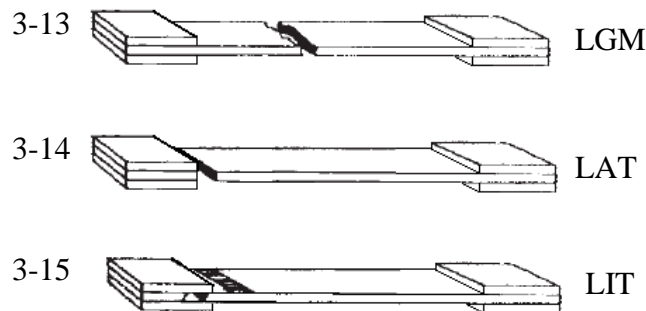
Figure 3-13, 3-14 and 3-15: Tensile Coupon Failure modes, (ASTM D3039, 2002)

3.2.2. ASTM D 3518 Specifications

ASTM D 3518 is a test method that determines the in-plane shear response of polymer matrix composite materials reinforced by high modulus fibres. The test procedure and preparation of tensile coupon specimens is identical to that of ASTM D 3039 except that the coupons are manufactured such that the fibres lie at an angle of 45° to the applied tensile force direction, as depicted in figure 3-16.
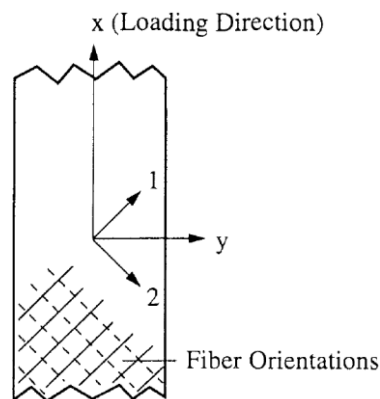
Figure 3-16: 45° Tensile Coupon (ASTM D3518, 2001)

3.2.3. Tensile Coupon Preparation

Preparation of tensile test coupons is a tedious and time consuming activity owing to the care that must be taken to manufacture both to standard specification and to avoid pre-test damage such as edge singularities that can cause high stress concentrations.

3.2.3.1. Fibrelam Coupon Preparation

Of the four Fibrelam panels tested, test coupons used for determining the material properties of the Fibrelam skins were cut from panels 1 and 4. The skins were cautiously removed from the honeycomb to avoid skin damage using a sharp cutting blade. The resin that bonds the skins to the honeycomb was left on the skins to avoid unnecessary damage being inflicted on the coupons. The assumption is therefore that the resin forms part of the Fibrelam skins.

The coupons were then cut from the skins, as in figure 3-17, by means of a sharp blade and steel ruler taking precautions to avoid notches, undercuts or delaminations. Rough or uneven surfaces and edges where then sanded to remove any singularities. Coupon dimensions were approximately 200×30×0.7 mm. The dimensions of each coupon were measured individually before testing, to eliminate manufacture error. The gauge section had a length of 80 mm.

End tabs where then bonded to the ends of the coupons. These where cut from 1.5mm thick aluminium sheets. Each tab was 30×30×1.5 mm.

Strain gauges where then bonded in place. Bonding of strain gauges requires clean and precise work. The application area is first cleaned with acetone to remove dirt and oils. The gauge is then bonded to the application area with an adhesive, provided by the gauge manufacturer, with applied constant pressure for a period of a minute. Figure 3-18shows a 350 Ohm Biaxial Strain Gauge bonded to a Fibrelam tensile test coupon.
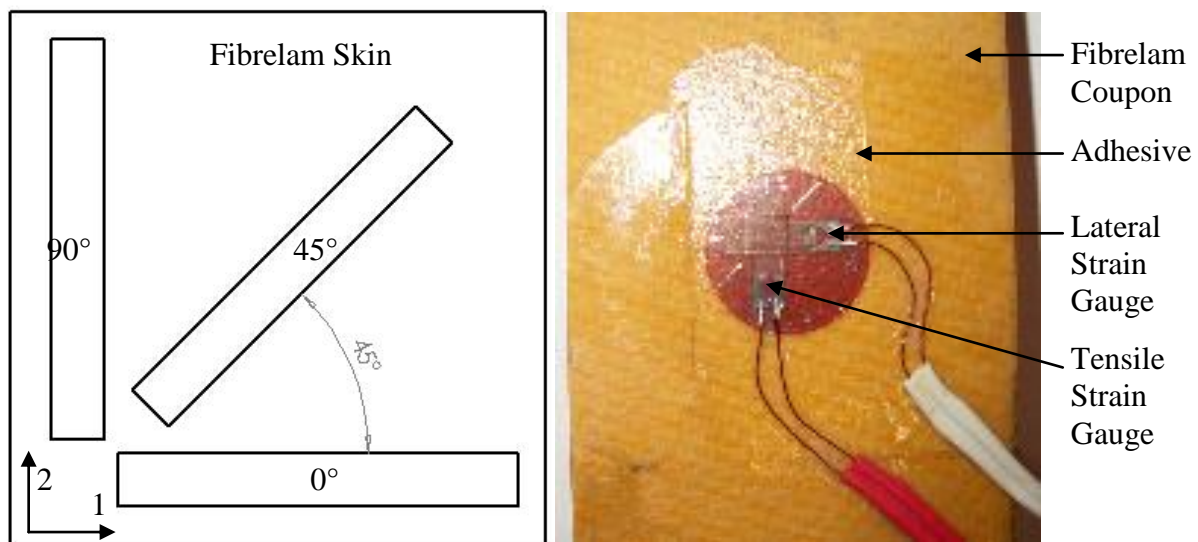
Figure 3-17 and 3-18: Coupon Cut Orientation and Bonded Strain Gauge

Coupons where prepared for two Fibrelam panels. Since each test condition requires 5 coupons and E_1 and v_{12} can be determined form 0° coupons, E_2 from 90° coupons and G_{12} from the 45° coupons, a total of 15 tensile coupons where required for each Fibrelam panel.

3.2.3.2. UAV Pre-preg Coupon Preparation

The preparation of the UAV pre-preg coupons was similar to that of the Fibrelam coupons except that they had to be cured and consisted of only a single ply of [0°/90°] weave pre-preg. Since a minimum of 6 data points are required to form a natural distribution of a material property, 6 sets of 5 coupons where needed for each test condition. 0°, 90° and 45° coupons where cut from a single ply sheet. The variability introduced by each curing cycle was taken into account by curing each ply sheet for each of the six sets separately. Thus 15 coupons where required from each set of which there were 6 separately cured sheets, giving a total of 90 tensile test coupons for the UAV pre-preg, 30 for each angle.

Strain Gauges are unfortunately very expensive and not re-usable. The digital image correlation system, despite a large initial capital layout, is thus a cost-effective solution to record strain for large quantities of tensile tests. Homogeneous surfaces however require specific test surface preparation for this system.

A stochastic pattern was sprayed onto the surface of the pre-pre coupons in order for the software to be able to identify changes between digital images. Figure 3-19 depicts a stochastic pattern sprayed onto a pre-preg coupon. The colour of the pre-preg is black and contrast was achieved with a gloss white spray paint.

Figure 3-19: Stochastic Spray Pattern

End tabs where also necessary in this case and again aluminium was used. End tab dimensions where 35×25×1.5 mm.

The coupon dimensions were 250×25×0.25 mm, thus giving an estimated gauge length of 110 mm. The ply thickness was measured after curing, using a vernier. These values where adapted from the coupon size used for Fibrelam to try and induce more acceptable failure modes to occur. Table 3-4 summarises the coupon dimensions.

Table 3-4: Coupon Dimension Summary

Material	Length	Width	Thickness	Gauge Section	Units
Fibrelam Skin	200	30	0.7	80	mm
UAV Pre-preg Ply	250	25	0.25	110	mm
End Tabs - Fibrelam	30	30	1.5	*	mm
End Tabs - UAV Pre-preg	35	25	1.5	*	mm

3.2.4. Tensile Test Equipment

Equipment necessary for tensile testing include a tensile machine to apply the load and a load cell for load measurement. In the case of the Fibrelam tensile tests, strain gauges and a strain recording device where used. Material tests on the wing pre-preg however made use of a digital image correlation system to record strain. These are discussed below.

The *Lloyd EZ50* advanced materials testing machine incorporates an extensive range of features making it ideal for performing complex as well as routine testing applications up to 50 kN (Lloyd Instruments LTD, 1999). This machine located in the University of Pretoria, Civil Engineering Laboratory incorporates Lloyd Instruments NEXYGEN data analysis and applications software to process load and strain signals to provide stress-strain curves. This machine was used for Fibrelam skin material testing.

The *Hydropuls PSA* materials testing machine in the Sasol Laboratory for Structural Mechanics was used for applying tensile force to the UAV pre-preg coupons.

A *5 Ton Load Cell* was available for use as a measurement device for applied tensile load. Measurements obtained in volts are converted to Newton with a calibration factor of 10 kN/V. This calibration factor was determined by loading the tensile machine with calibrated masses.

350 Ohm Biaxial Strain Gauges, code: KFG-5-350-D16-11, allow for simultaneous measurement of tensile as well as lateral strain values.

Spider8 is an electronic measuring system for PCs for electric measurement of mechanical variables such as strain, force, pressure etc. Spider8 is connected to the computer via the printer port or via an RS232 interface and is then ready for immediate use (HBM, 2003).

The *Digital Image Correlation System* (figure 3-22), recently purchased by the University of Pretoria Sasol Laboratory, is a non-contact optical 3D deformation measuring system. ARAMIS software recognises the surface structure in digital camera images and allocates coordinates to image pixels. Digital images taken throughout the test are then compared to calculate displacements (GOM mbH, 2009).

3.2.5. Tensile Test Setup – Fibrelam Skin

An overview of the tensile test setup for Fibrelam coupons is depicted in figure 3-20. The equipment consisted of the EZ50 materials testing machine, the Spider8 data recorder, a 5 ton load cell, strain gauges and "dummy" strain gauges.

"Dummy" strain gauges where placed on Fibrelam panels and connected to the setup via half bridges as in figure 3-21. This configuration cancelled out the effects due to temperature variation. The load signal from the Load-cell was connected to the 1st channel of the Spider8. The lateral strain gauge signal was sent to channel 2 and the tensile signal to channel 3, both in bridge configuration.
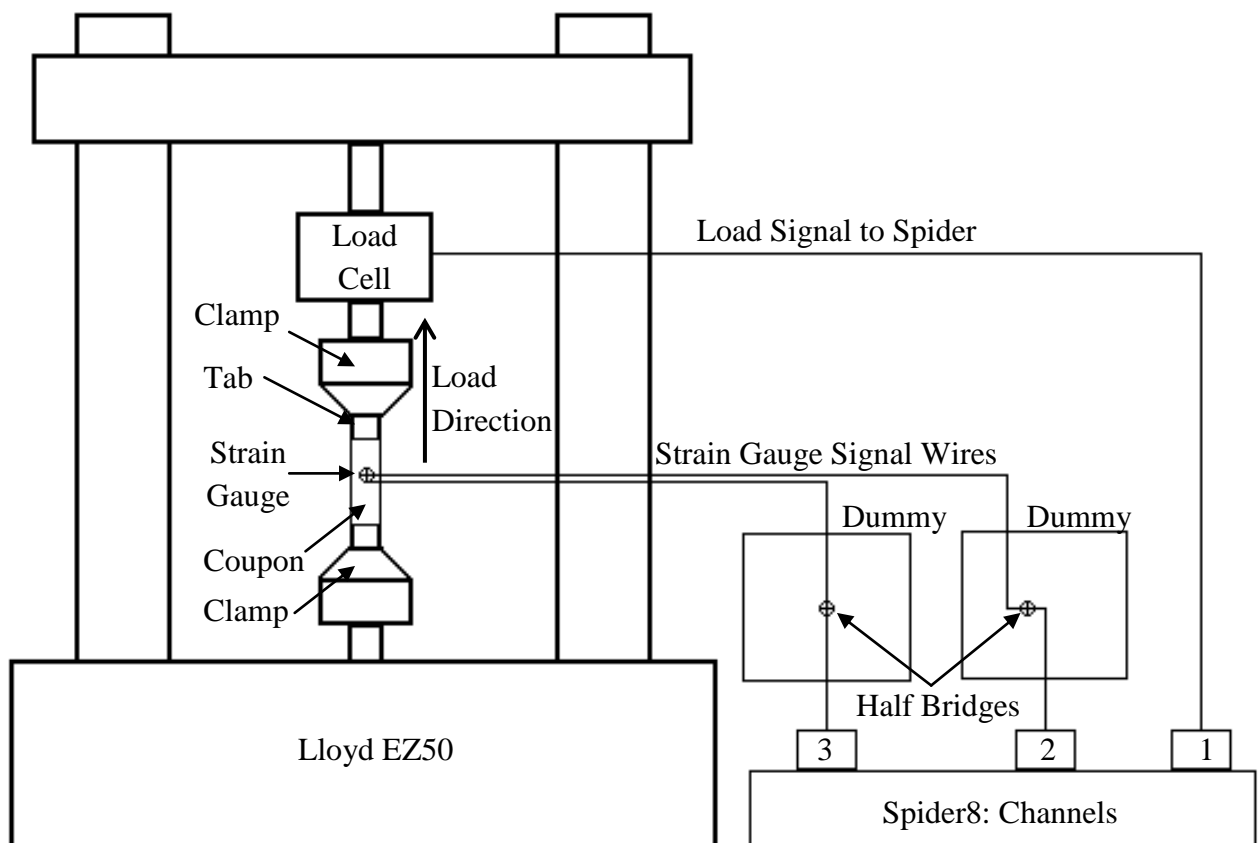
Figure 3-20: Overview of the Tensile Test Setup for Fibrelam Coupons
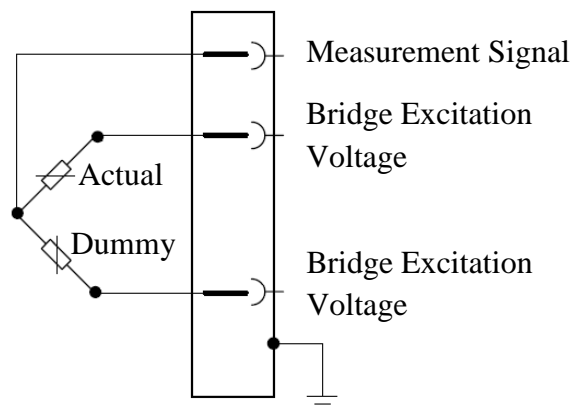
Figure 3-21: Half Bridge Configuration, Channel 2 and 3

The coupons were clamped at the top and bottom ends, on the end tabs, using manual tightening clamps. There is no specification as to how tight clamping must be done but this was figured out through trial and error.

The main function of the clamps is to provide a gripping area for the tensile machine on the coupons without slippage. Care must be taken not to over tighten as this causes stress concentrations at the grips and result in bad failure modes.

3.2.6. Tensile Test Setup - UAV Pre-preg

An overview of the tensile test setup for UAV pre-preg coupons is depicted in figure 3-22. The equipment consisted of the Hydropuls materials testing machine, the digital image correlation system and a load cell.
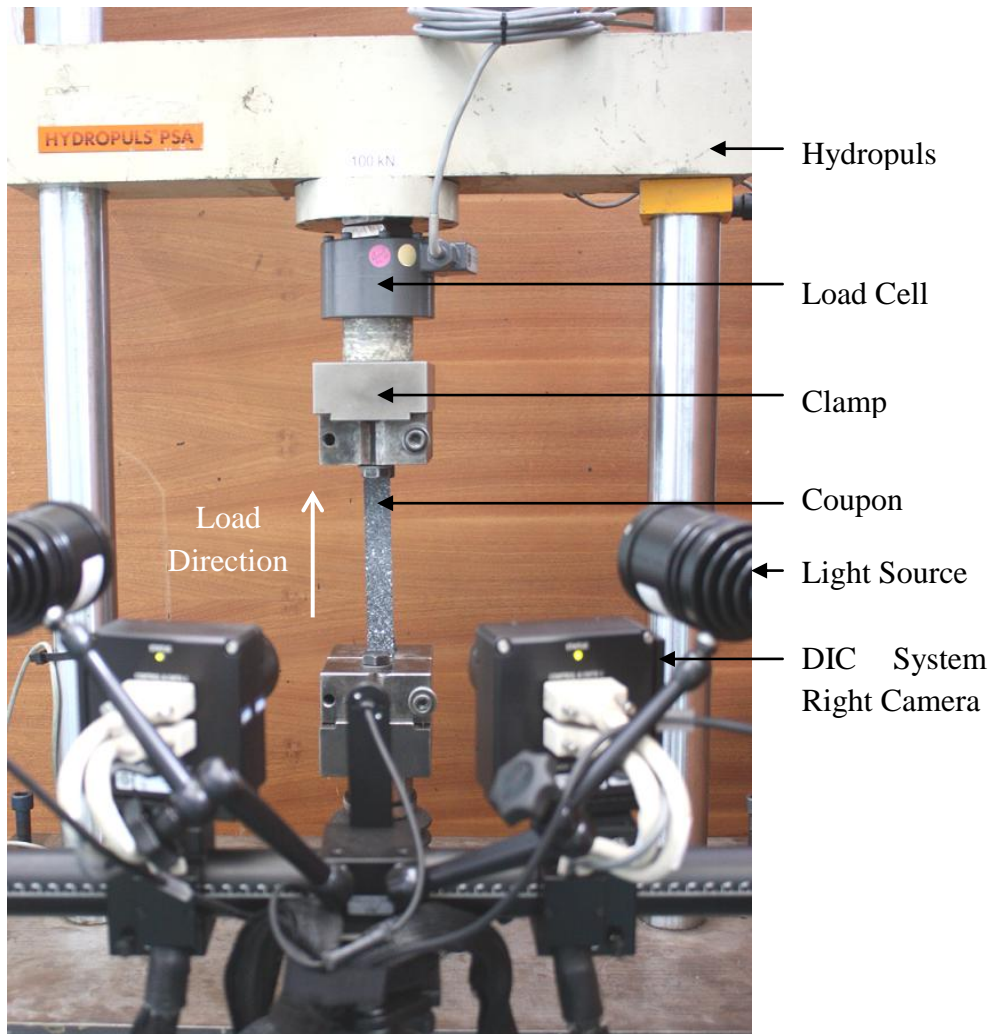
Figure 3-22: Overview of the Tensile Test Setup for UAV Pre-preg Coupons

The procedure for testing was the same as that for Fibrelam except that the strain gauges and Spider8 where replaced by the DIC System.

3.2.6.1. Calibration and Settings

Calibration of the DIC system is crucial to obtaining useable results and must be performed before commencing with testing or if cameras are moved or accidently bumped during testing. The left and right cameras are first focused and then aligned using a calibration panel, as in figure 3-23.

The speed of testing was set to attain an early constant strain rate in the gage section. The strain rate was selected so as to produce failure within 1 to 10 min, in accordance with ASTM.
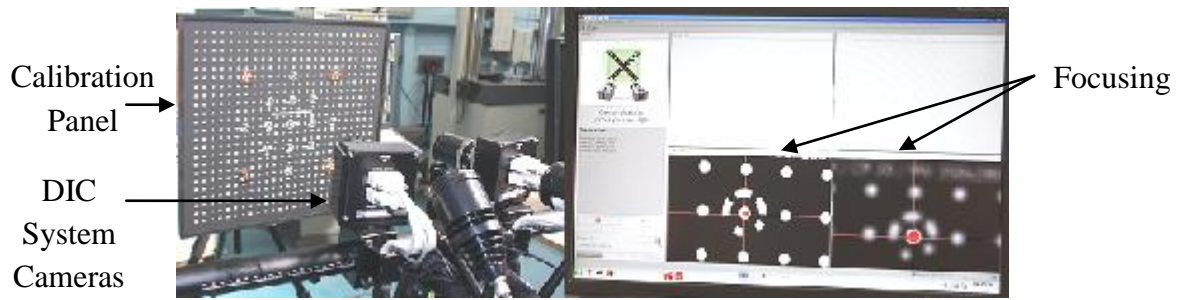
Figure 3-23: DICS Calibration
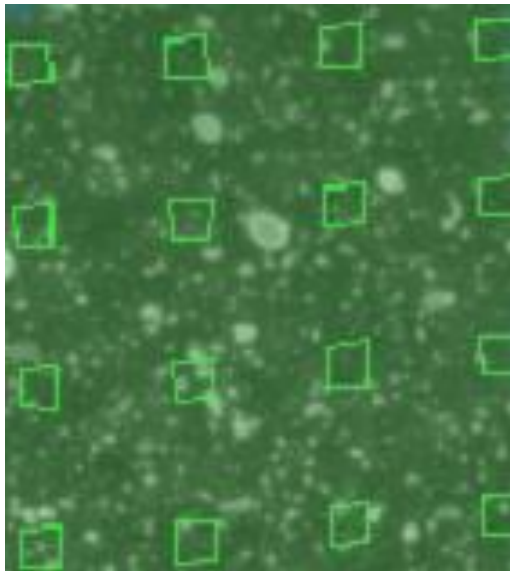
Figure 3-24: Pixel Facets

During testing, the cameras can be triggered to take the digital images in a number of ways. In this instance, the voltage signal from the load cell was used as the trigger because this provided a constant rate of images due to the constant strain rate requirement by ASTM. One image was taken for every increase of 100mV. Up to 200 images where taken per test depending on stiffness (elasticity) and breaking strength of the coupon being tested.

During computation, ARAMIS observes the deformation of the coupon surface through the images by means of various square or rectangular image details (facets). Figure 3-24 shows the identification these pixel facets.

The first image taken was used as reference and thus assumed to have zero strain. Load associated with this image was thus set to zero at this reference, despite a 100kN pretension.

3.2.7. Density

The density of the Fibrelam skin (including the bonding resin) was calculated from the weight and volume of skin panels (before they were cut into tensile coupons). Similarly the UAV pre-preg density was calculated from each batch coupon plate. The density values for the UAV pre-preg is given in table 3-5 and that of the Fibrelam in table 3-7.

Table 3-5: UAV pre-preg Density Result (ρ) from 6 Batches

Individual Batch Result ρ [kg/m^3]						[kg/m^3]		
Batch 1	Batch 2	Batch 3	Batch 4	Batch 5	Batch 6	Mean	Std dev	COV
1063	960	1117	900	1176	1303	1087	134	12%

3.2.8. Fibrelam Tensile Results

Fibrelam panels have two main material components; the skins (consisting of aramid fibres, resin matrix and the resin that bonds the skin to the core) and the honeycomb core. Tensile tests were performed on the aramid skins and the results are discussed. The honeycomb was however not material tested but data rather taken from available manufacturer datasheets

(Hexcel, 2007b) to limit excessive material testing as the Fibrelam panels were only for procedure familiarisation. Refer to table 3-2 for property values.

Figure 3-25 depicts the stress vs. tensile-strain and stress vs. lateral-strain curves from a 0° tensile test coupon.
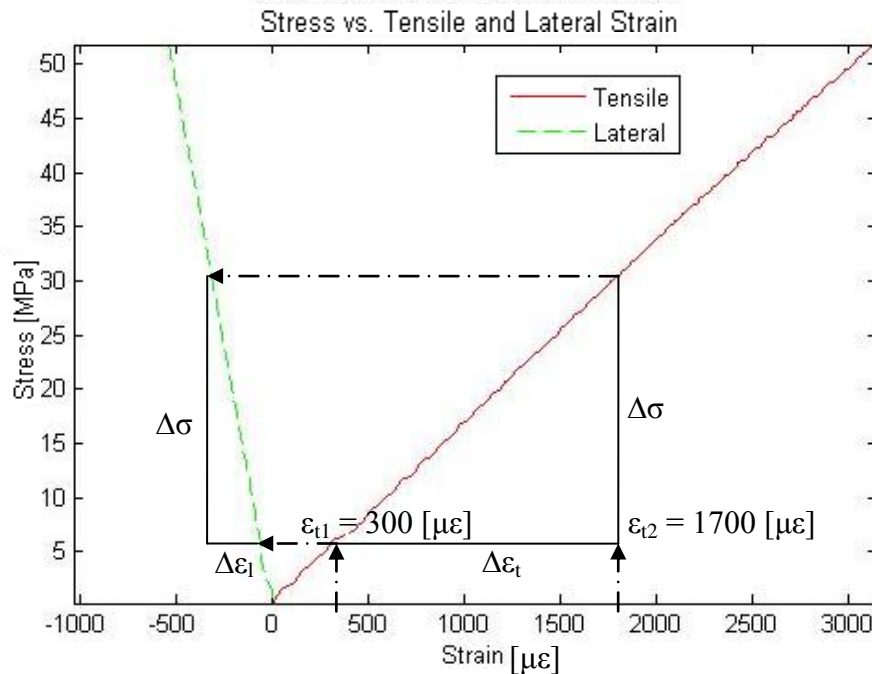
Figure 3-25: Stress vs. Tensile and Lateral Strain

The elastic moduli (E_1 and E_2) of the Fibrelam skins were calculated from equation 3.2 applied to the 0° and 90° test coupons respectively.

$$E = \frac{\Delta\sigma}{\Delta\varepsilon} \qquad (3.2)$$

where E is the tensile modulus of elasticity, given in terms of GPa, $\Delta\sigma$ is the difference in applied tensile stress between two strain points that lie in the chord modulus region (figure 3-25) and $\Delta\varepsilon$ is the difference between two strain points in the chord modulus region.

As recommended by ASTM, the moduli calculations were taken from the linear region of the curves. For all tensile direction cases, $\Delta\varepsilon_t$ was calculated using $\Delta\varepsilon_{t2} = 0.0017$ and $\Delta\varepsilon_{t1} = 0.0003$ or the closest possible data point. The corresponding stresses where found and used in equation 3.2 to calculate E.

Poisson's ratio (ν_{12}) was obtained from the transverse strain ε_t at each of the two longitudinal strain points ε_l, as applied to a 0° coupon:

$$\nu = -\frac{\Delta\varepsilon_t}{\Delta\varepsilon_l} \qquad (3.3)$$

where $\Delta \varepsilon_t$ is the difference between two longitudinal strain and $\Delta \varepsilon_l$ is the difference in lateral strain between the two longitudinal strain points.

The stress values used to determine $\Delta \sigma$ for the elastic moduli were used to find the corresponding lateral strain values as depicted by the flow in the figure.

Finally G_{12} was calculated from equation 3.6 and using stress-strain data from the 45° tensile test coupons. Table 3-7 summarises the mean Fibrelam skin tensile test results. Firstly the shear stress present in the test coupon was calculated from equation 3.4

$$\tau_{12} = \frac{P}{2A} \qquad (3.4)$$

where P is the load in Newton, applied in the tensile direction and A is the coupon cross sectional area in accordance with ASTM D 3039.

The Shear strain was then calculated from equation 3.5

$$\gamma_{12} = \varepsilon_x - \varepsilon_y \qquad (3.5)$$

where ε_x is the longitudinal normal strain and ε_y is the lateral normal strain

Now the shear modulus could be determined:

$$G_{12} = \frac{\Delta \tau_{12}}{\Delta \gamma_{12}} \qquad (3.6)$$

where $\Delta \tau_{12}$ is the difference in applied shear stress between the two shear strain points and $\Delta \gamma_{12}$ is the difference between the two shear strain points.

Table 3-6 presents the 0° tensile test results for modulus of elasticity E_1 on Fibrelam panels 1 and 4. The mean, standard deviation (Std dev) and coefficient of variance (COV) is given for each panel. The estimated modulus value from the long beam bending test is given at the datasheet value. Codes are presented for the mode of failure for each coupon (refer to table 3-6). Those highlighted in dark green are excellent failures while those in light green are acceptable.

The mean values obtained for E_1 are exceptionally close to that specified by the material datasheet, panel 1 results only differing by 1.3%. Due to a connection problem, no strain gauge signals where recorded for the first two coupons of panel 4.

A summary of the mean Fibrelam 2D orthotropic properties is given in table 3-7.Further results are discussed in appendix D.

Table 3-6: Fibrelam Modulus of Elasticity (E_1)

Coupon #	Panel 1 [GPa]		Panel 4 [GPa]	
1	17.16	AWT	N/A	AWT
2	17.06	LWT	N/A	LWB
3	16.42	LGM	17.45	AWB
4	16.40	LWT	15.50	LWT
5	16.30	AWT	17.78	LWT
	Mean	16.67	Mean	16.91
	Std dev	0.41	Std dev	1.23
	COV	2.5%	COV	7.3%
	datasheet:	16.46	datasheet:	16.46
	% diff Panel 1	1.3%	% diff panel 4	2.7%

Table 3-7: Fibrelam 2D Orthotropic Properties

Property	E_1	E_2	G_{12}	v_{12}	ρ
Units	[GPa]				[kg/m^3]
Panel 1	16.67	16.79	3.16	0.18	1546.64
Panel 4	16.91	17.55	3.64	0.17	1538.35

3.2.9. UAV Tensile Results

Figure 3-26 shows some of the typical failure modes of the UAV pre-preg coupons.
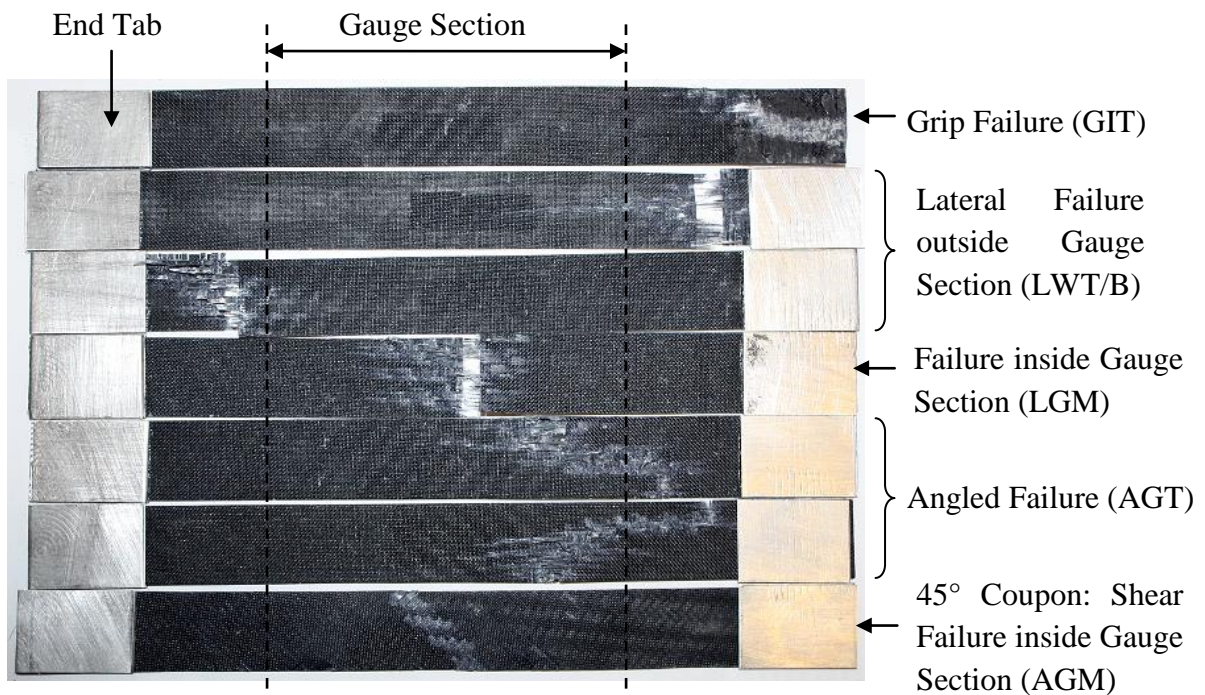
Figure 3-26: UAV Tensile test Coupon Failures

Results from failure of the grips or end tabs had to be discarded and the coupon remanufactured for testing. Failures outside the gauge section where used if the failure did not extend into the grip area. Results were ideally used from coupons that failed in the gauge section.

The digital image correlation system revealed coupon failure from edge singularities despite caution taken during coupon manufacture (figure 3-27).
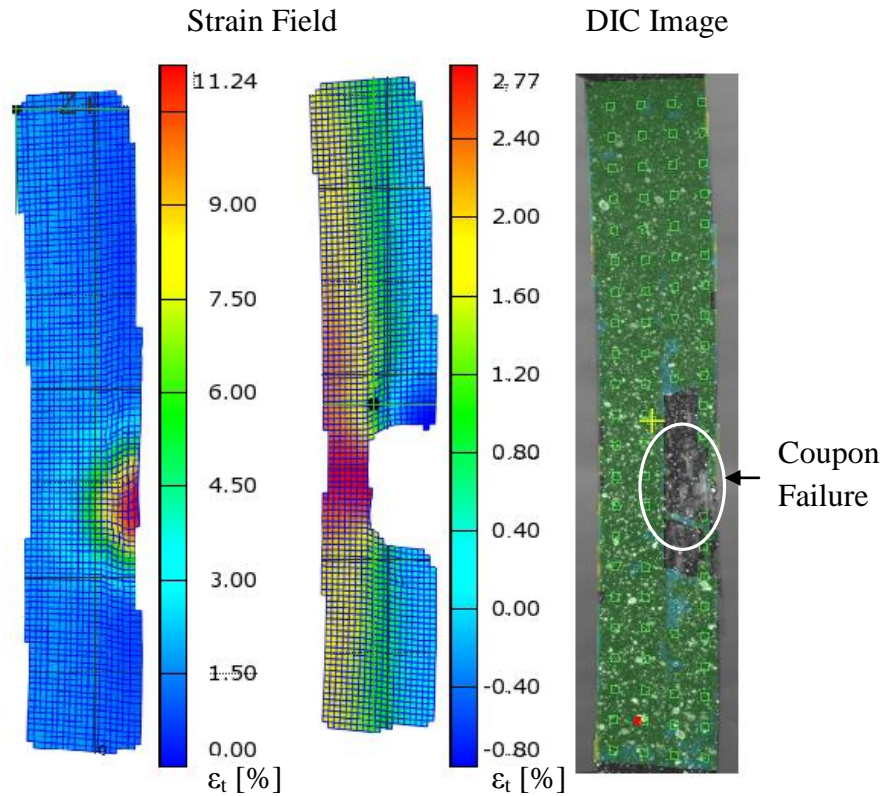
Figure 3-27: DIC system Strain Field of Tensile Coupon and Edge Singularity

The stress-strain graphs for all the 0° and 90° UAV skin ply tensile coupons are each superimposed in figure 3-28.
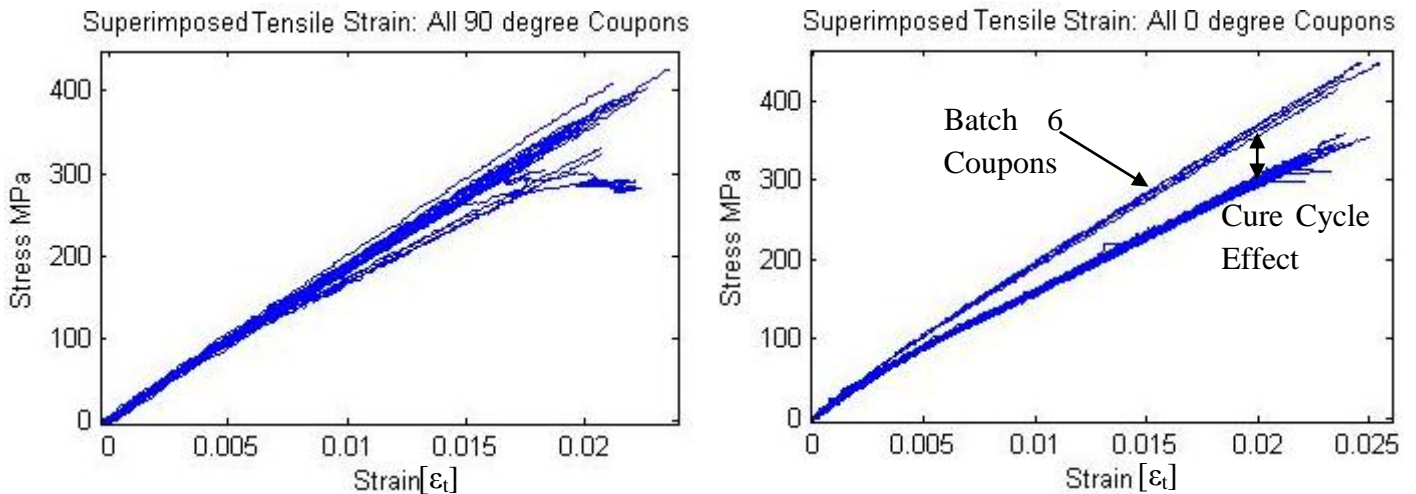
Figure 3-28: Superimposed Stress vs. Tensile Strain Results for 0° and 90° Coupons

The 0° coupon graph shows the effect of curing on the material tensile properties. Batch 6 seems to have a much higher ultimate tensile strength despite being cut from the same roll of pre-preg. Fortunately these effects seem lesser in the linear elastic region but it is still important to take the curing cycle variations into account, which is why each batch was cured separately

The shear stress-strain graphs for the UAV skin plies are shown in figure 3-29.These coupons where cut at 45° angles and failed in shear.
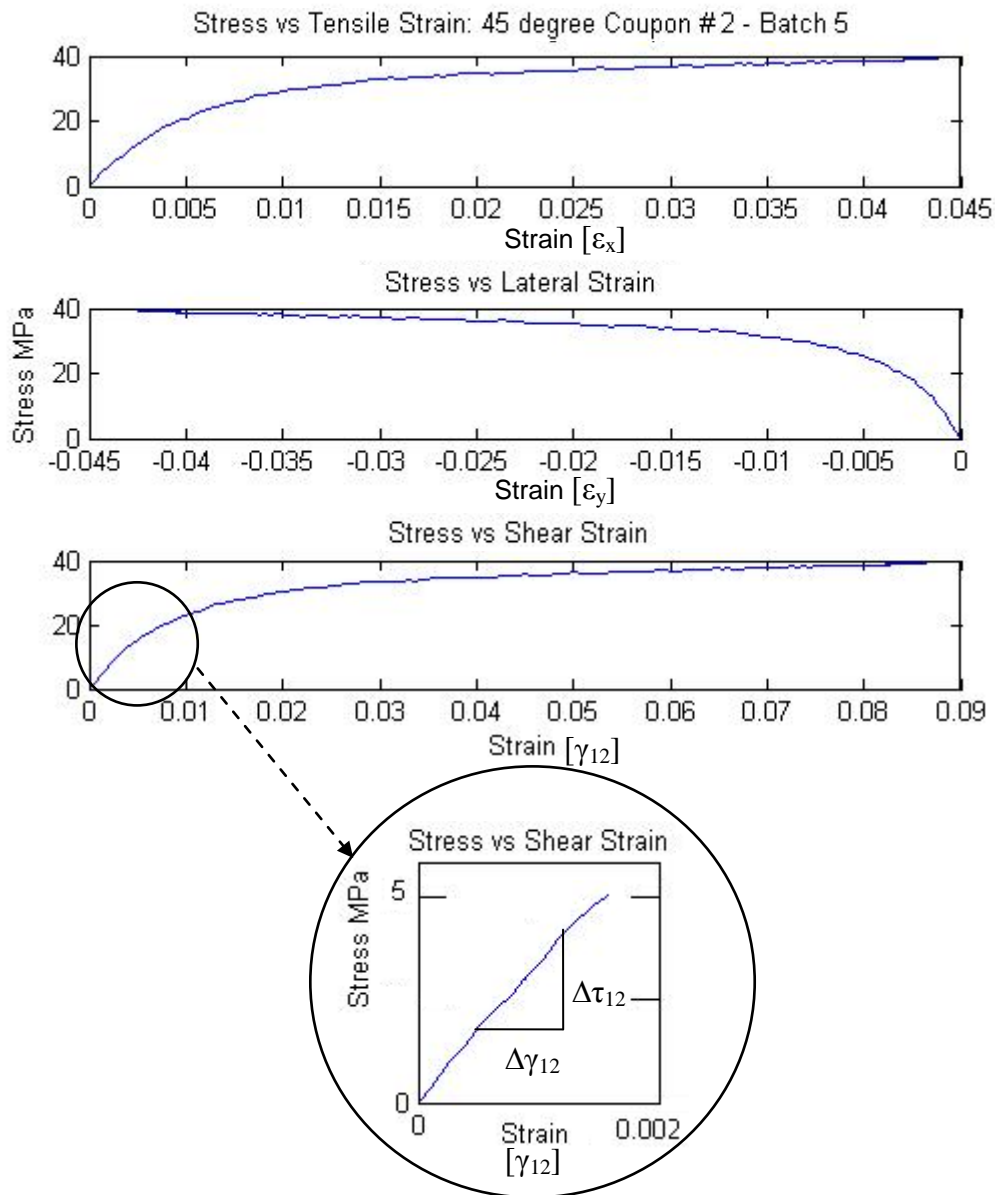
Figure 3-29: Shear Stress vs. Strain Results for a 45° Tensile Coupon

Note the lower stress gradients here as compared to the 0° coupons in figure 3-28. These graphs show extreme elasticity due to a phenomenon called scissoring. Scissoring occurs when cross fibres of angle cut coupons pull together and give the illusion of strain. Kellas, Morton and Jackson (1993) suggest that a general rule of thumb for this is that a fibre rotation of 1° takes place for every 2 % of strain. This is the principal rationale for terminating tests at a large strain level. ASTM suggests terminating data reporting at 5 % calculated shear strain;

this limits fibre scissoring to about 1.5°. Fortunately the required linear region lies below these strain levels.

The elastic moduli E_1 and E_2 were calculated similarly to that of the Fibrelam coupons. Table 3-8 gives the E_1 values of each of the 5 coupons for 6 0° batches.

Table 3-8: UAV pre-preg Elastic Modulus Tensile test Result (E_1) from 0° coupons

| Batch # | Individual Coupon Result: Elastic Modulus E1 [GPa] | | | | | Batch Result [GPa] | | |
	Coupon 1	Coupon 2	Coupon 3	Coupon 4	Coupon 5	Mean	Std dev	COV
1	19.31	17.88	18.70	18.61	18.36	18.57	0.52	2.82%
2	19.22	18.63	18.20	18.53	18.59	18.63	0.43	2.30%
3	19.03	20.23	18.85	18.61	18.08	18.96	0.61	3.21%
4	16.71	17.49	18.12	19.66	18.13	18.02	1.02	5.67%
5	16.80	18.89	19.37	17.42	17.98	18.09	1.00	5.55%
6	16.98	20.67	20.29	20.47	19.79	19.64	1.48	7.52%

The mean values hover around 18-19 GPa. Values vary by up to 7% which is fairly low when considering composite materials. Values are often expected to vary by up to 20% or more. This low variability is due to the repeatable nature of pre-pregs. The post manufacture cure cycles definitely have an effect as can be seen with batch 6 which has a higher variation in comparison to other batches. The mean and standard deviation from each of the 6 batches can now be used to estimate a distribution for E_1.

The assumption that material properties follow a normal distribution is verified by figure 3-30. The graph on the left is a normal probability plot. The purpose is to graphically assess whether the data could come from a normal distribution. If the data is normal, the plot will be linear. Other distribution types will introduce curvature in the plot. The linear fit in the case of E_1 is 95.8%. The graph on the right is a typical histogram plot showing normal distribution behaviour of the fit superimposed over E_1 data.
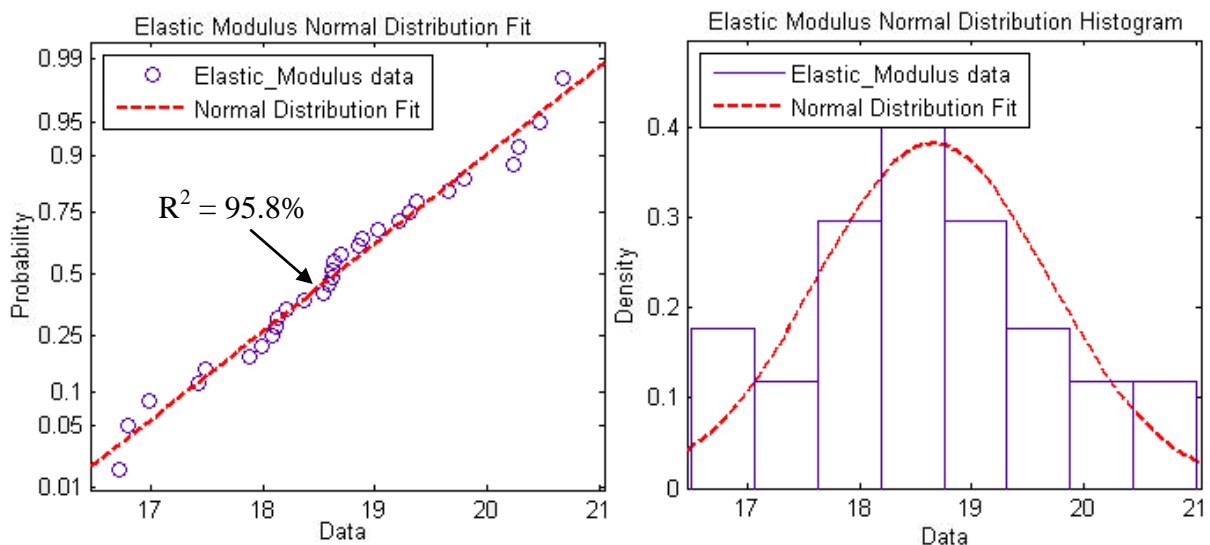
Figure 3-30: Normal Distribution Verification for E_1 Data

Table 3-9 summarises the final mean values derived from the 6 batch means, for initial use in FEM. Further results can be found in appendix D. Resin beads (Axson Technologies, 2008) and the foam spar (Roha-cell, 2010) are assumed isotropic and properties taken from datasheets. Isotropic shear moduli can be calculated from equation 2.6. Resin Poisson's ratio is an estimate due to a lack of datasheet info and requires updating.

Table 3-9: UAV Wing 2D Orthotropic Properties

Property	E_1	E_2	G_{12}	v_{12}	ρ
Units	[GPa]				[kg/m^3]
Skin Ply	18.65	20.21	3.34	0.16	1087
Resin Beads	3.40	*	1.41	0.20	1170
Foam Spar	0.09	*	0.03	0.30	75

4. Vibration Testing and Modal Analysis

In this chapter the non-destructive aspect of the experimental testing is dealt with. Vibration response data is first collected and analysed. Setup configuration is covered and explained after which the applied signal processing is discussed and frequency domain results are presented. In the second section the acquired vibration data is post-processed through modal analysis and modal parameters are presented and discussed.

4.1. Vibration Testing

Vibration testing was performed in this case to ascertain the structural frequency response functions of Fibrelam panels and UAV wings. This was done by exciting the structure and measuring the resulting response. In order to obtain optimal results, the equipment had to be selected carefully to avoid adverse effects.

4.1.1. Vibration Test Equipment

Equipment necessary for vibration testing includes an excitation device (actuator or modal hammer with a force transducer) and a response measurement device (laser vibrometer).

Force transducers that are bonded to the structure have the effect of adding mass. In the case of composites where the structure is light, the added mass effect is large. The advantage that modal hammers have over bonded transducers (like that excited by a vibro-pet) is that they are not fixed to the structure and thus have no added mass effect. Figure 4-1 shows two superimposed FRFs measured from a Fibrelam panel.
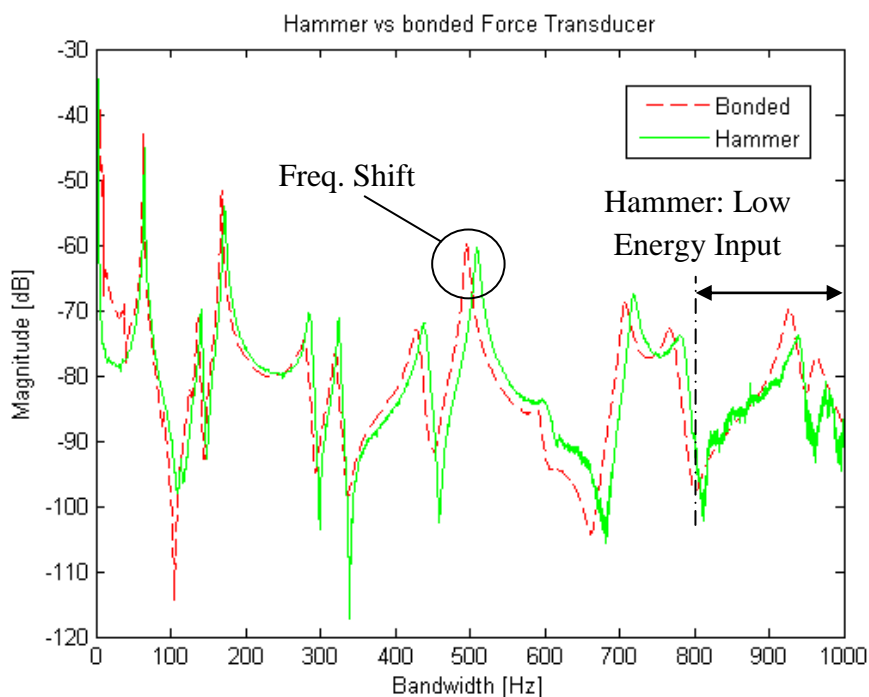
Figure 4-1: Mass Effect of Bonded Force Transducer

The shift in peaks to the left (approximately 3% shift) of the FRF excited by the bonded transducer as compared to that of the modal hammer indicates the presence this mass effect. Note also though that the FRF produced by the hammer test is more noisy since it is more difficult to operate and often more difficult to provide enough energy to excite higher frequency modes with.

The type of tip used for modal hammers depends on frequency of the targeted bandwidth. Commonly steel tips work best for higher frequencies while softer nylon or rubber tips are used for low to medium frequency bandwidths. In the case of composites however, it was found that a steel tip was necessary to introduce enough energy to excite even medium to low order modes. The reason for this is the high values of the resonant frequencies resulting from high stiffness to mass ratios of the composite structures.

Response recording devices such as accelerometers that need to be bonded to the structure are also disadvantaged by the addition of mass. Another difficulty is that if a large area of the structure has to be measured, either a large number of accelerometers need to be mounted or they must be moved over the surface as testing progresses. The Polytec 400 is a non-contact velocity response recording instrument. This therefore adds no mass to the structure and a large number of points can be measured over a large area in an automated fashion.

The scanning laser head is capable of manoeuvring the laser over the structure's surface by adjusting the angles of reflective mirrors. The Doppler shift is used to determine the velocity of the measured structure by comparing a reference beam and the beam reflected back from the vibrating structure (Polytec, 2008).

4.1.2. Test Structure Preparation

There is not much in the way of preparation of a structure for vibration testing, especially when compared to that of tensile test coupons. The main concern is that of laser reflectivity off the structure surface. Appendix E explores the comparison between different reflective surface preparations on a Fibrelam panel.

The best option is to use reflective stickers. It is then necessary to determine the density of scan points. There needs to be enough points to accurately capture the modes but scanning too many points can become very time consuming and generate excessive data.

Figure 4-2 shows the layout of 264 reflective stickers placed on the top surface of a UAV wing. The Fibrelam panels only had 64 stickers due to less complicated deformations. On the wings, each sticker size was approximately 10×10 mm in size. 11 stickers where placed in a column along the profile and 24 rows of these along the length of the wing.
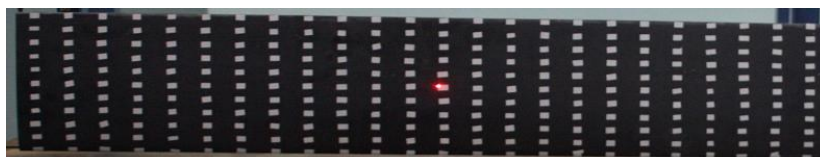
Figure 4-2: Scanning Head Schematic

The reason for placing scan points more densely along the profile of the wing was due to the structure being essentially a uniform hollow tube with a support beam running along its length, near the leading edge. Thus the vibration response was expected to vary more from leading to trailing edge than it would along its length.

4.1.3. Vibration Test Setup

A schematic of the test setup is shown by figure 4-3. The test structure (both Fibrelam panel and UAV wing) was suspended from a rigid frame using elastic rubber strips. The effect is that of added damping. This is unfortunately the most practically possible way to simulate free-free boundary conditions short of removing gravity. In the case of the UAV wing, the wing was suspended horizontally from the trailing edge at each end, as in figure 4-4. The Fibrelam panels where hung in a similar fashion, except that there was no trailing edge.
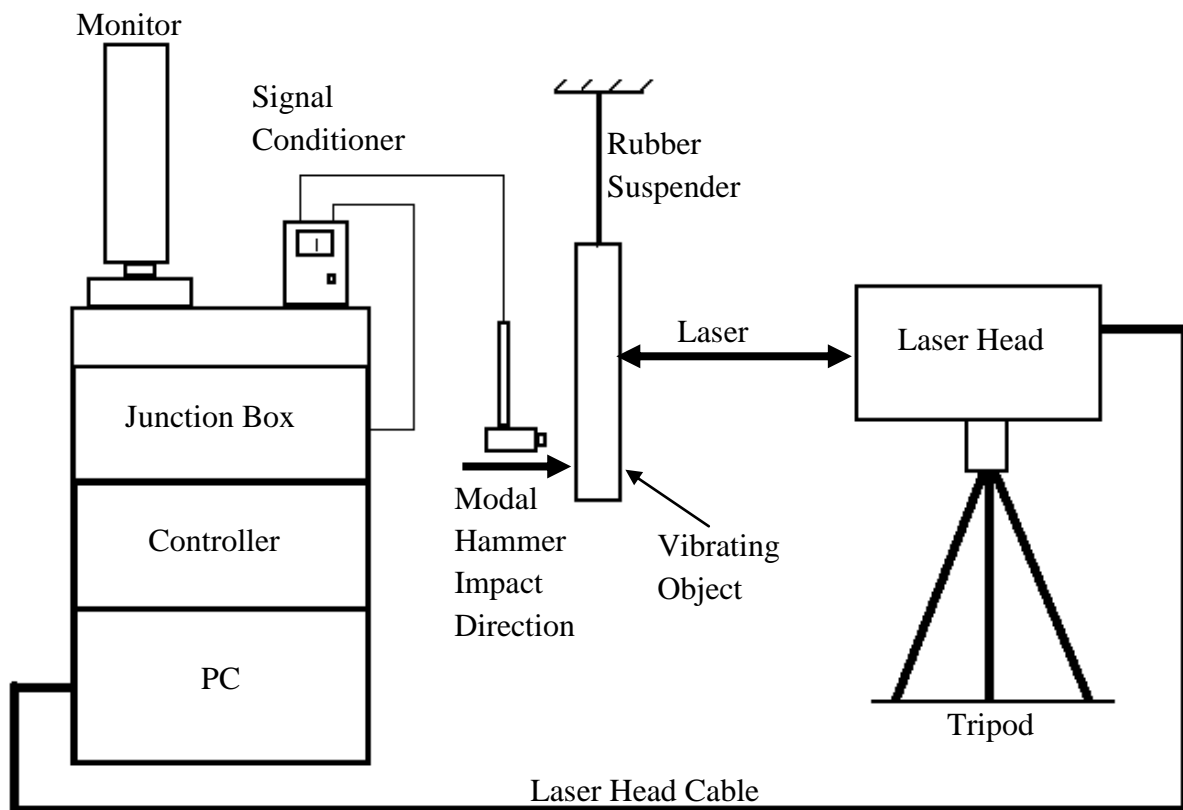
Figure 4-3: Scanning Head Schematic

The laser scanning head was mounted on a tripod and directed at the test structure. The first step was to position the laser at an optimal stand-off distance from the structure. Due to the length of laser's light wave, optimal distances were calculated from equation 4.1

$$\text{Optimal stand-off distance} = 99 \text{ mm} + (n.L) \text{ mm} \qquad (4.1)$$

where $n = 0,1,2 \dots$ and $L = 204$ mm $\pm$ 1 mm

i.e. optimal stand-off distances are 99, 303, 507, …,1323, … mm (Polytec, 2008). The distance was set to 1323 mm so that the laser head camera could view the entire test surface.

This is important because the angle at which the laser can scan (away from being perpendicular to the structure) is 26 degrees, thus it must be placed far enough back.
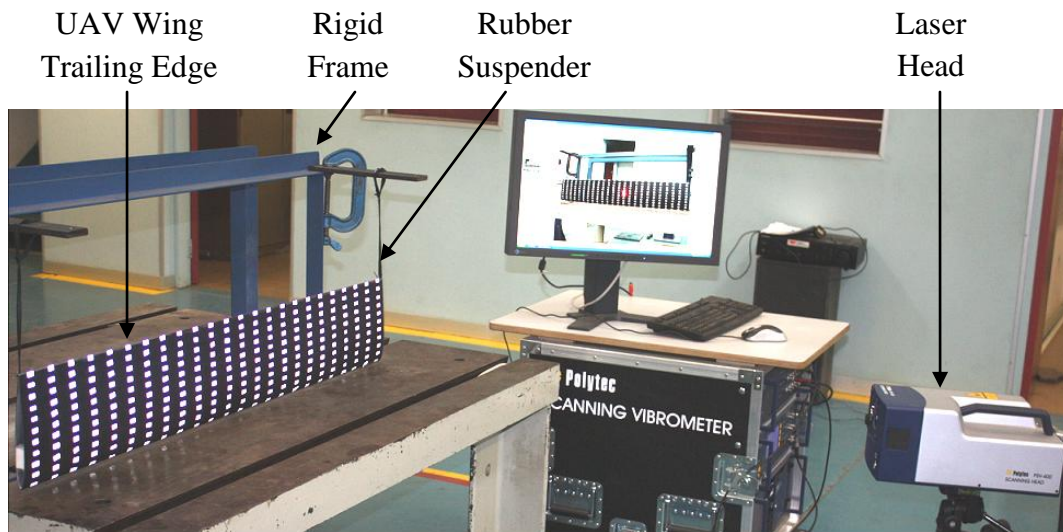
Figure 4-4: Photograph of UAV Wing Vibration Test Setup

The camera then had to be focused so that scan point coordinates (stickers) could be correlated with the image from the laser head on the monitor. The scan points are manually defined on the monitor using the mouse. This lets the scanner know where all the desired scan points are on the structure. It is possible to automatically create a grid and specify scan point densities using the software, but since each structure hangs slightly differently in each setup (due to slight mass differences, precision of placing the suspenders etc.) the camera must be refocused for each test setup and the scan points must then be readjusted to match the sticker positions. Figure 4-5 shows a test setup requiring scan point correlation-adjustment.
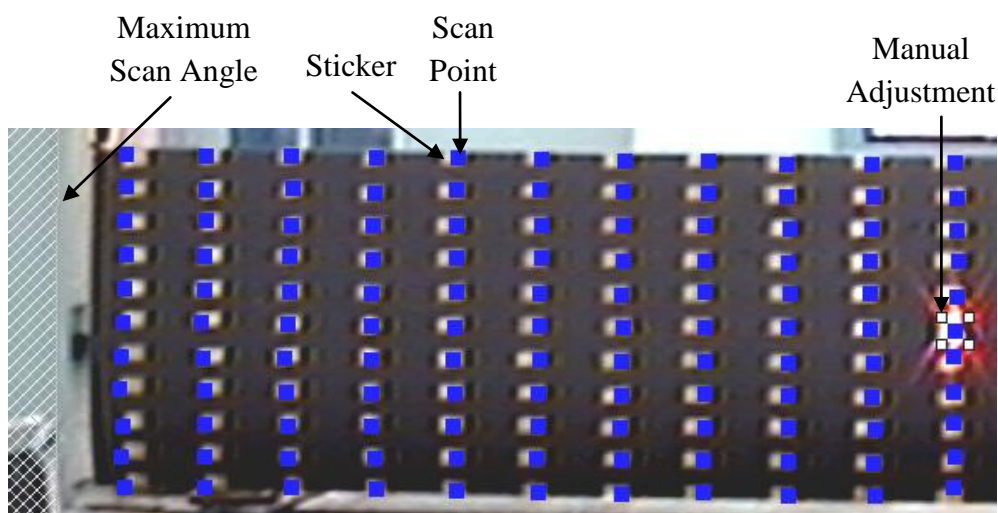
Figure 4-5: Scan Point Correlation

The structures were struck by a modal hammer from the back, in the direction of the laser head. This position for impact was chosen so that the hammer would not interfere with the line of sight of the laser head during scanning. The reference signal from the hammer is sent through the signal conditioner and the gain kept at 1. The laser systems junction box receives the reference signal from the hammer and sends it to the controller which sends a trigger to

the laser head (from the PC) to start scanning on impact. A trigger is fundamental to successful testing in that it prevents phase shifts occurring between the hammer impact and response recorded. The result of testing without a trigger is noise.

Calibration of the Scanning laser head is a default manufacturer setting but any auxiliary equipment needs to be calibrated. The modal hammer used (SN 8132) has a calibration sensitivity of 2.15 mV/N.

4.1.4. Vibration Test Settings

The frequency bandwidth over which vibration data was collected for the structures was selected based on the number of modes required and the amount of energy that could be introduced to excite those modes. Modes become more complicated and more difficult to simulate accurately in finite element models with an increase in modal order. The bandwidths in table 4-1 were used and contain information for at least 6 mode shapes.

Table 4-1: Vibration Sampling Settings

Structure	Bandwidth [Hz]	Sampling Freq. [Hz]	Sampling Time [s]	Resolution [Hz]
Fibrelam	0-1000	2560	1.6	0.625
UAV Wing	0-400	1024	4	0.25

Some light signal processing was also performed using the laser vibrometer system software. A high pass filter of 10 Hz was used on the response signal to eliminate the backwards and forewords swaying of the test structures (rigid body modes) from the FRFs. This was applied to the UAV wing vibration tests.

An exponential window was used on the forcing function from the modal hammer to eliminate the possibility of leakage. Care also had to be taken to make sure a single impact was made with the hammer for each measurement. Figure 4-6 depicts the forcing function in the time domain of a double hit on a wing. Figure 4-7 shows the result of the double hit on the magnitude of the transfer function in the frequency domain.
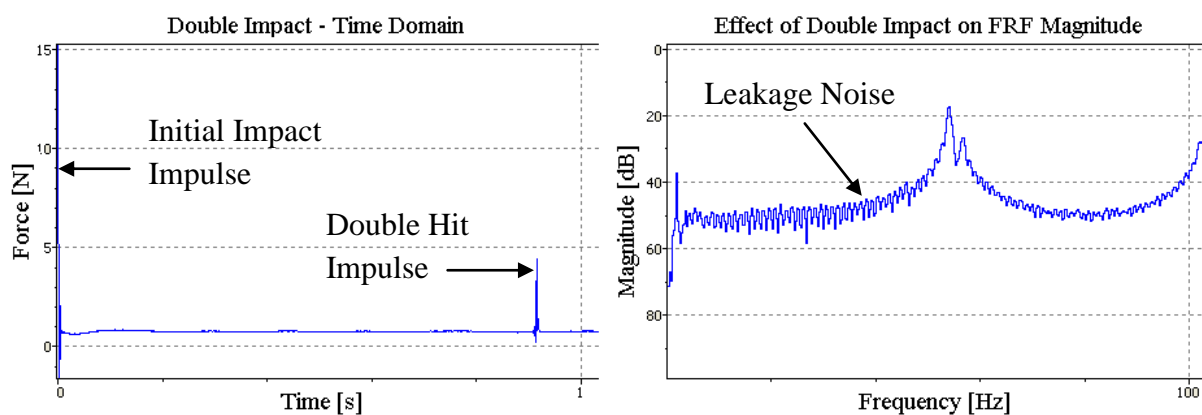
Figure 4-6 and 4-7: Modal Hammer Double Hit in the time and frequency domains

Five complex averages (since a trigger was used and excitation was deterministic) were used to attain better quality FRFs. This means that the structure had to be impacted and the response measured 5 times for each scan point. The average response was then used. This improved the signal-to-noise ratios of the spectra.

To further improve signal quality, Speckle tracking was used. This is a method by which the scan point is moved slightly (by about 1μm) for each average, in an attempt to find better laser reflectivity(Polytec, 2008).

4.1.5. Vibration Results Fibrelam

Five Fibrelam panels were prepared for vibration testing. Panel 3 was discarded due to core damage. Since the panels were all "off cuts", there was no definite knowledge about manufacture, grade or damage. Initially 4 panels where scanned, the superimposed FRF results for scan point 1 of 64 are shown in figure 4-8. These were done with a bonded force transducer and vibro-pet setup through which a periodic chirp was sent for actuation. The purpose figure 4-8 is to observe repeatability of the panels. The corresponding phase plots are also given and verify resonances and anti-resonances with phase shifts.
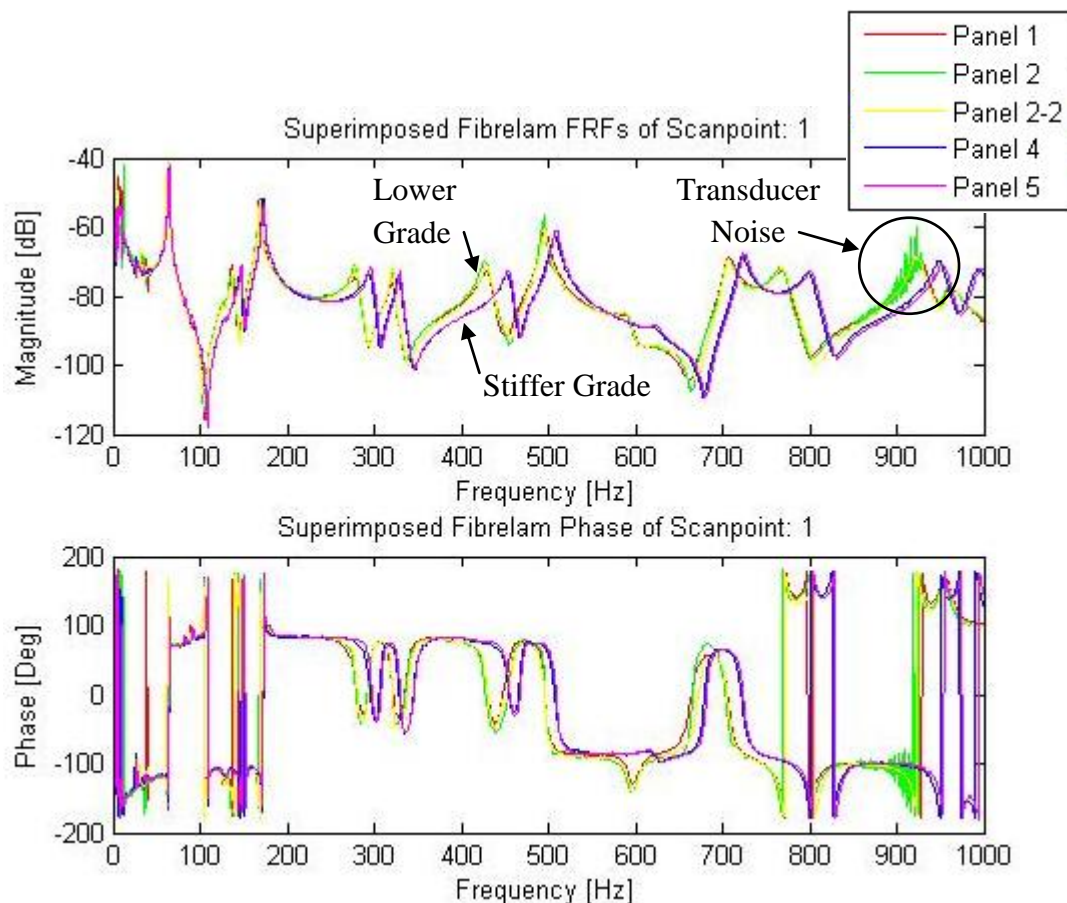
Figure 4-8: Superimposed Fibrelam FRFs

It is observed that panels 1 and 2 show very close correlation and likewise for panels 4 and 5 but these are shifted to the right in comparison to the first 2. A possible explanation for this is

the orientation at which the panel skins where applied to the honeycomb resulting in reversed 1 and 2 direction stiffness.

There was a gradual failure of the force transducer during the testing of panel 2 which resulted in noise at around 900 Hz. The panel was rescanned and labelled panel 2-2. It was then observed that there was a change in peak magnitude for some resonances despite panels 2 and 2-2 being the same panel. There were no frequency shifts and thus it was noted that the effect was from damping introduced by the rubber suspenders.

Since the bonded transducer has appreciable mass effect, panel 1 was re-scanned with a modal hammer setup. The hammer was capable of imparting enough energy to easily excite modes below 700 Hz (refer to figure 4-1).

4.1.6. Vibration Results UAV Wings

Six wings were scanned over a bandwidth of 0-400 Hz. The first 6 modes lay below 160 Hz for undamaged wings 1 and 3. Due to damage on wing 2, repeatability of the UAV wings could only be observed by comparison of wings 1 and 3. Superposition of the FRFs of these 2 wings in figure 4-9, is however sufficient enough to indicate a large degree of variability.
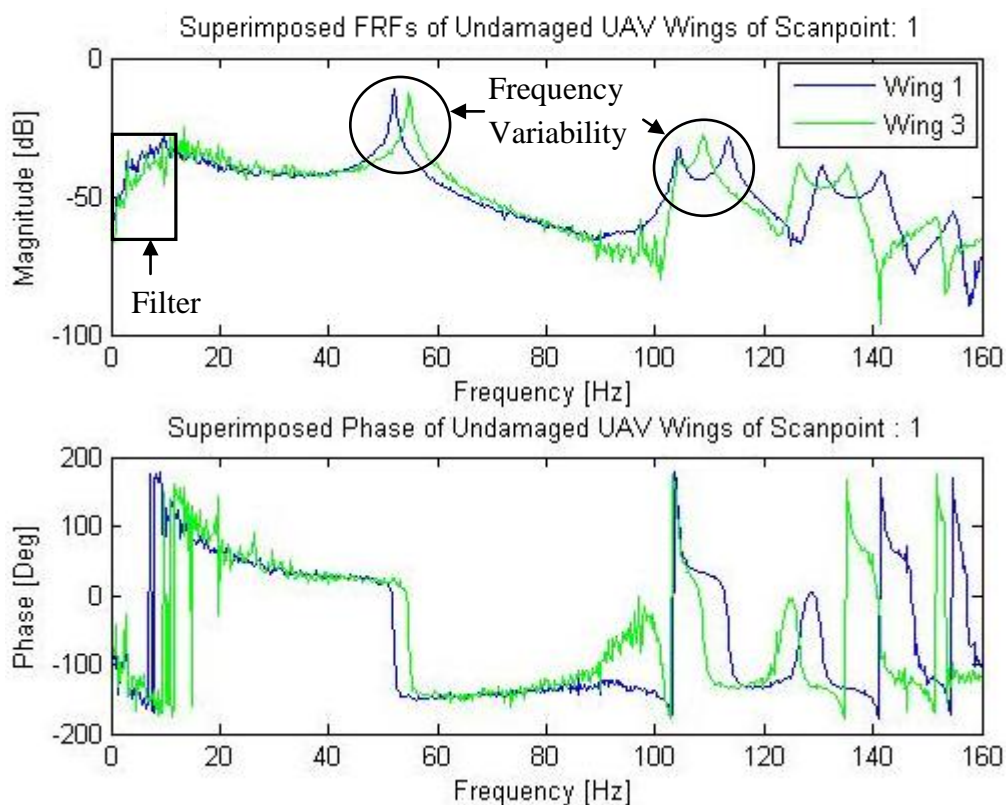
Figure 4-9: Superimposed FRFs of Undamaged UAV Wings

Note the effect of the 10 Hz high pass filter, in eliminating rigid body modes, applied to the response signal. This filter did not affect the results but simply removed the low frequency "sway" from the response signal.

As a matter of interest, the wings were scanned on the bottom skin and compared to the result from the top skin (figure 4-10). Good correlation was expected due to the symmetric shape of the airfoil. It was found that the FRFs did correlate well for most scan points.
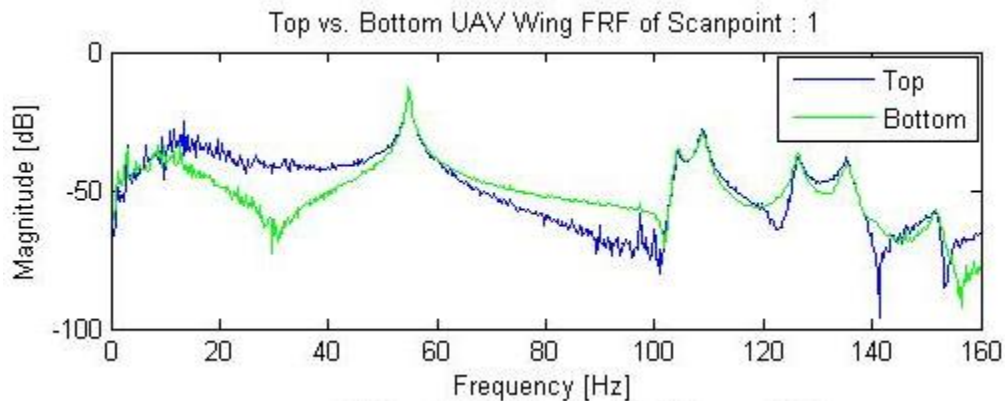
Figure 4-10: Superimposed Top vs. Bottom FRFs of UAV Wing 3

It is not possible to see the effect of delamination directly from observation of the FRFs. Figure 4-11superimposes the FRFs for damaged wings 4-6 and undamaged wings 1 and 3. In observing the shifts in resonance frequency between wings, it is clear that the effect of delamination is outweighed by the variability of material properties and wing manufacture.

Although the first peak seems to show a shift pattern suggesting loss of stiffness from delamination, it is not the case for all resonant frequencies. As a result, frequency shift is eliminated as a possible method of delamination detection (refer also to table 4-4 for modal analysis frequency values).
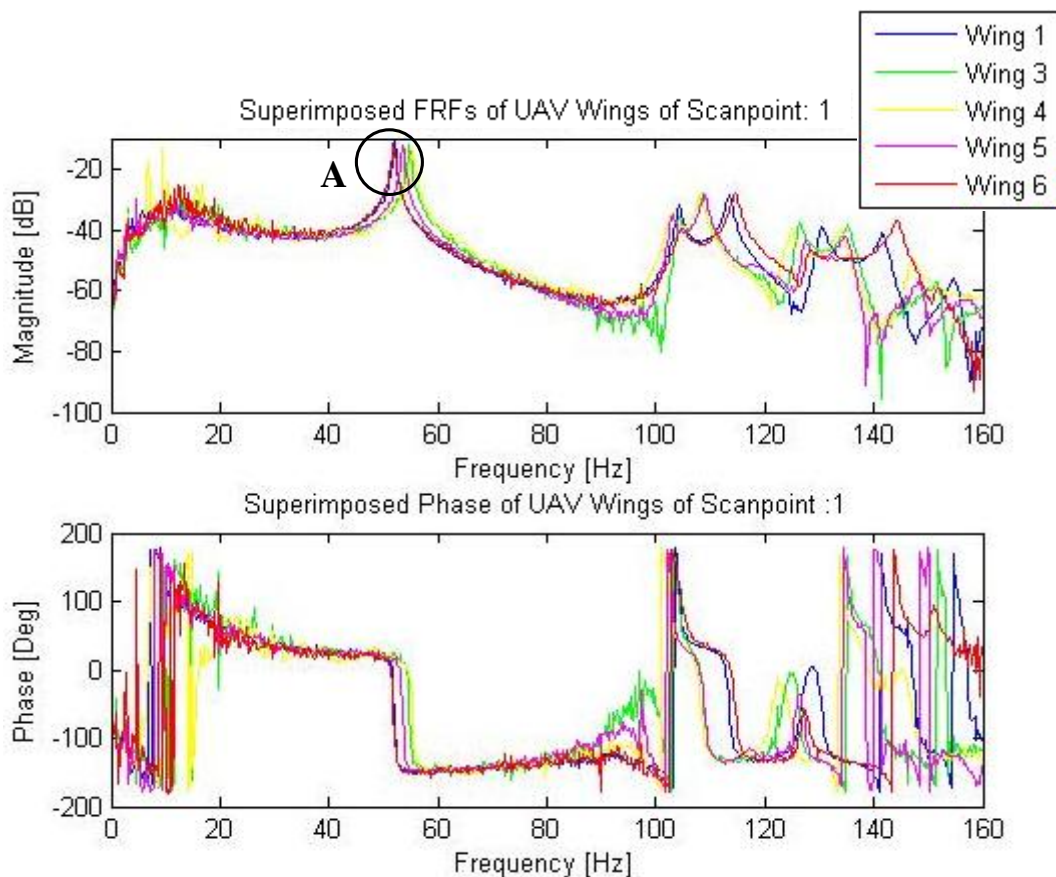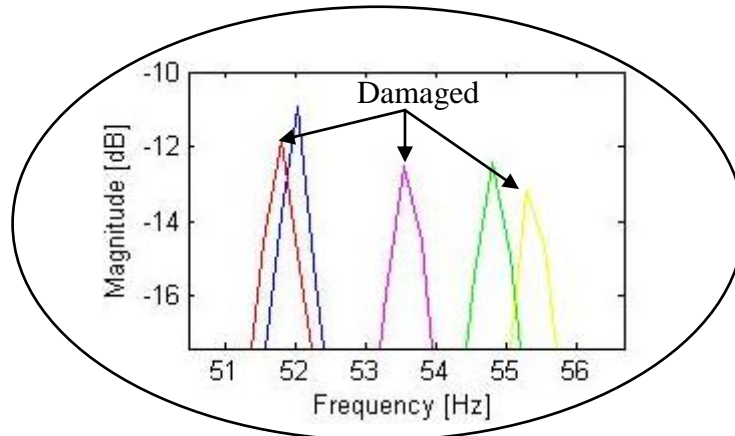
Figure 4-11: Superimposed FRFs of all UAV Wings

4.2. Modal Analysis

The use of OROS Modal 2 Analysis Software greatly simplifies the modal analysis procedure. It is capable of handling experimental modal analysis (EMA) where excitation and response data are available and operational modal analysis (OMA) where the excitation is not known.

EMA identification methods can be classified as SISO (single input single output), SIMO (single input multiple output) and MIMO (multiple input multiple output) according to different numbers of inputs and outputs.

FRFs are generally utilized for EMA in the frequency domain, and are estimated from the excitation and response signals. Then the modal parameters are identified by constructing the parametric or nonparametric models of the FRFs and curve fitting them.

4.2.1. OROS SIMO Procedure

Since the Polytec scanning laser vibrometer used to capture the responses scans several measurement points that all share the same point of excitation, a single input multiple output algorithm is required. Rational Fraction Orthogonal Polynomials (RFOP) is a SIMO modal identification algorithm in the frequency domain suitable for EMA.

The structure geometry and FRF Data is first drawn into OROS. A bandwidth is then selected that contains at least one resonant frequency as in figure 4-12. This is the modal identification function (MIF) in OROS. The denominator order is entered (this is usually easy to estimate from the FRF) and is twice the modal order which is 1 in this case.

The MIF is a collective FRF over the whole range of scan point FRF's. The MIF bandwidth is best selected in the low magnitude dips between modes. ORIOS then identifies the selected mode and generates a synthesized FRF (for each scan point FRF). Figure4-13 below shows the Synthesized FRF for the first scan point on an Undamaged UAV wing. From these synthesized FRF's the modal parameters are determined.
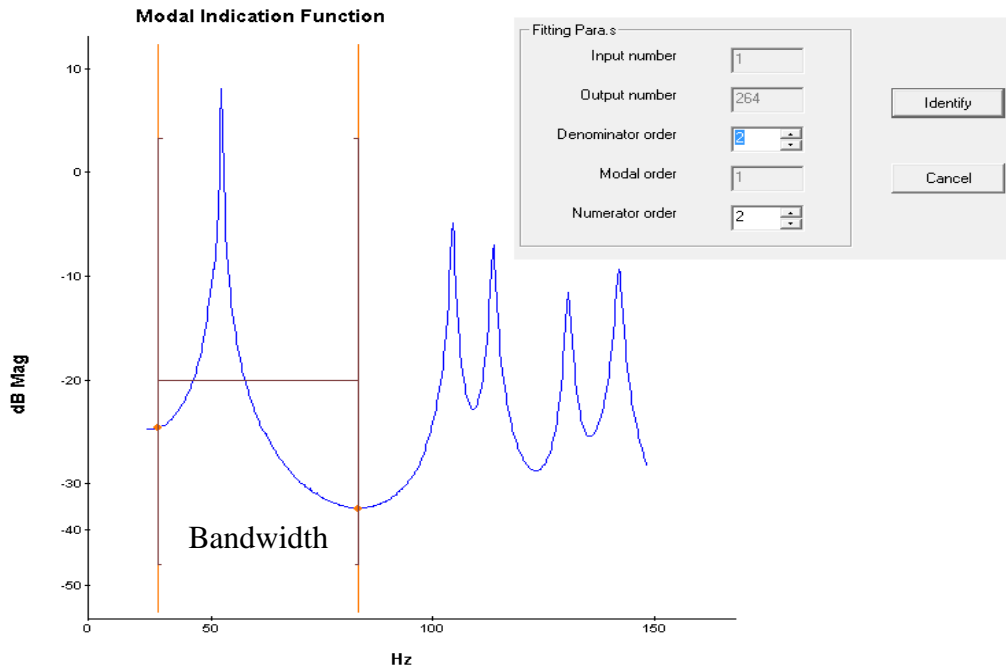
Figure 4-12: Modal Identification Function (MIF)
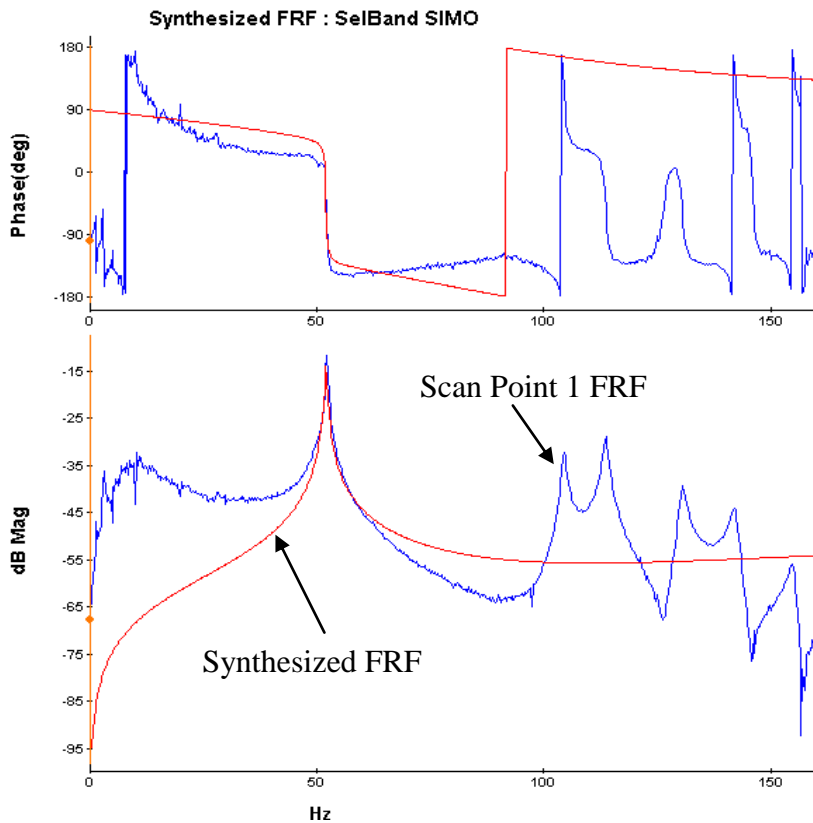
Figure 4-13: Synthesized FRF

OROS also has a broad band modal analysis algorithm (EMA BroBand) which is capable of analysing the modes over a very broad bandwidth simultaneously.

4.2.2. Fibrelam Modal Analysis Results

Each scan point was numbered according to creation order, by the laser vibrometer, from point 1 at the top left to the last point on the bottom right. Figure 4-14 is the geometry for the full size (1000×200 mm) Fibrelam.
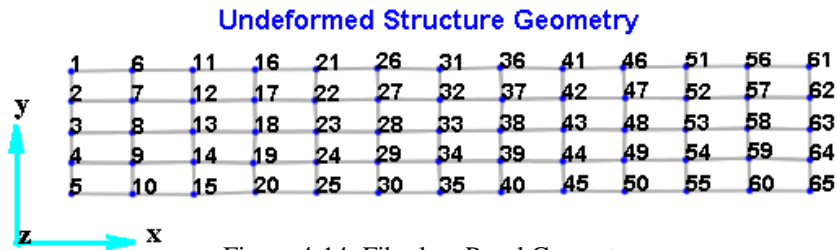
Figure 4-14: Fibrelam Panel Geometry

4.2.2.1. Original Size Fibrelam Panels

Table 4-2 gives the modal frequency and damping values first the first 6 full size Fibrelam panel mode shapes attained with a modal hammer setup for Fibrelam Panel 1.

Table 4-2: Fibrelam Modal Parameters

Mode #	Frequency (Hz)	Damping (%)	Type
Mode 1	64.11	0.36	Bending
Mode 2	140.61	0.96	Torsional
Mode 3	171.67	0.73	Bending
Mode 4	286.64	1.3	Torsional
Mode 5	324.85	0.67	Bending
Mode 6	439.53	1.23	Torsional

The first 6 natural frequencies lie below 500 Hz for this panel. The damping factors are a little higher than the typical values of bare composite materials, generally around 0.2-0.3% (Irvine, 2004). This is likely due to the expanded structure of the honeycomb.

The first six modes (figure 4-15) are typical in shape of free-free transverse beam vibration. Modes 1, 3 and 5 are lateral bending modes with 2, 3 and 4 nodal lines respectively.
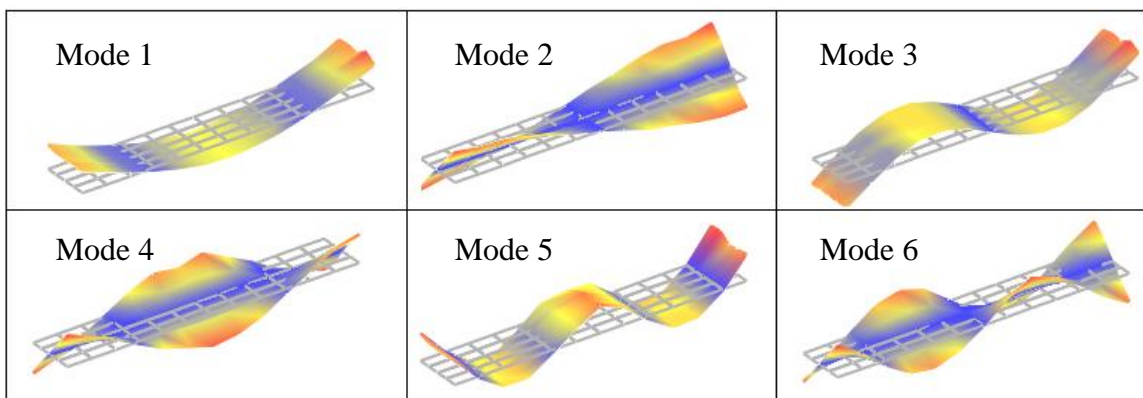
Figure 4-15: Fibrelam Modes (Full Size Panel)

Modes 2, 4 and 6 are torsional modes of increasing complexity. It can clearly be seen though that these are experimental modes which depict unexpected mode patterns at the structure ends. Since the structures tend to sway back and forth during testing there is loss of laser reflectivity and in some instances the laser may even move off the structure completely as in the case with scan points close to the edge.

4.2.2.2. Small Size Fibrelam Panels

The small size Fibrelam panel was cut from the one above and tested for use in multi-model updating. Table 4-3gives the modal frequency and damping values first the first 7 smaller size Fibrelam panel mode shapes attained with a modal hammer setup for Fibrelam Panel 1.

Table 4-3: Fibrelam Modal Parameters

Mode #	Frequency (Hz)	Damping (%)	Type
Mode 1	233.98	0.96	Bending
Mode 2	272.54	1.29	Torsional
Mode 3	563.75	0.95	Torsional
Mode 4	588.74	0.62	Bending

The first 6 natural frequencies now lie below 230-590 Hz for this panel. The reason for this is simply the smaller size resulting in a stiffer structure. The damping factors slightly higher than for the longer beam but still seem reasonable.

The first four modes (figure 4-16) are again typical in shape of free-free transverse beam vibration. Modes 1 and 4 are lateral bending modes with 2 and 3 nodal lines respectively. Modes 2 and 3 are torsional modes.
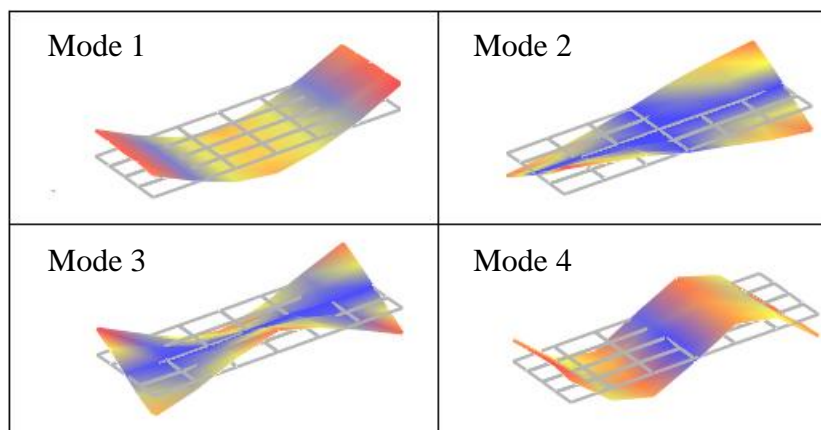
Figure 4-16: Fibrelam Modes (Small Panel)

4.2.3. UAV Wing Modal Analysis Results

Consider the wing profile in figure4-17. The modal analysis results of the vibration measurements taken with the laser vibrometer on the top and bottom skins of the wing are discussed here. Figures depict the modes of wing 1 (undamaged). Note that due to the nature of the structure, the magnitude of the modes dynamics vary along the wing profile, from the leading edge (LE) to the trailing edge (TE), with variation of structure stiffness.
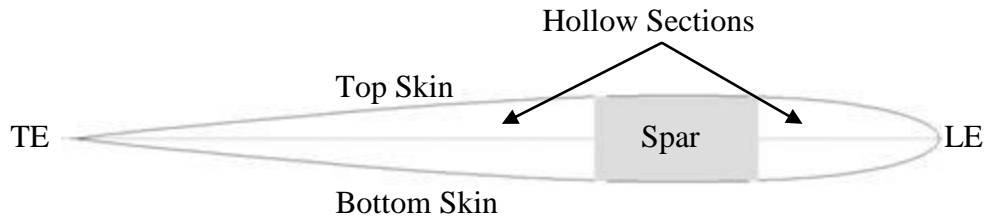
Figure 4-17: UAV Aerofoil Cross-section

Tables4-4and 4-5give the modal parameter values for the first 6 modes of wings 1, 3, 4, 5 and 6 scanned on the top skin. Wing 2 is discussed in appendix E.

Table 4-4: Natural Frequencies (ω_n) [Hz]

Wing #	1	3	4	5	6
Mode 1	52.2	55.0	55.6	53.8	52.1
Mode 2	104.4	104.4	103.4	103.1	104.6
Mode 3	113.6	109.0	108.3	109.1	114.7
Mode 4	130.6	126.5	124.7	127.4	128.2
Mode 5	141.9	135.6	134.2	135.1	144.4
Mode 6	155.0	151.8	147.2	148.6	152.5

Table 4-5: Modal Damping Factor %

Wing #	1	3	4	5	6
Mode 1	0.37	0.44	0.46	0.43	0.45
Mode 2	0.43	0.46	0.46	0.46	0.75
Mode 3	0.45	0.49	0.52	0.54	0.56
Mode 4	0.44	0.46	0.60	0.51	0.73
Mode 5	0.49	0.52	0.55	0.60	0.60
Mode 6	0.34	0.30	0.55	0.40	0.68

The frequencies seem somewhat scattered but all lie below 160 Hz which is much lower than that of the stiffer Fibrelam panel, likely due to the honeycomb structure. There is no frequency pattern as a result of delamination damage. The modal damping factors however do seem show to show a general increase in value relating to delamination. This is in accordance with observations by Keye (2006) who used modal damping factors as a delamination detection technique. The effects seem to grow with delamination size (i.e. increase from wings 4 to 6) and are more sensitive in higher order modes as they tend to be more sensitive to changes than lower order modes (Keye, 2006:201).

4.2.3.1. Wing Mode 1: Bending

The first UAV wing mode is a 1st order bending mode with magnitude variation along the wing profile. Figure 4-18a is an isometric view and 4-18b is a top view of the mode. Images are that of wing 1.The magnitude of dynamic deformation is the most consistent along the leading edge and near the spar. Here the shape is typical of a 1st order bending mode.

The shape however, becomes more complex towards the trailing edge, moving away from the spar, where the skins are able to deform more freely. The area in the centre of the wing towards the TE shows more skin dynamics as a result. Other areas of high dynamic magnitude are near the ends of the wings, also due to low structural stiffness.

There are two nodal lines, each roughly a quarter wing length's distance from each end. This is the area where the delaminations were placed in the damaged wings. Mode 1 is therefore not useful for detection of damage in this area.

a) Isometric View
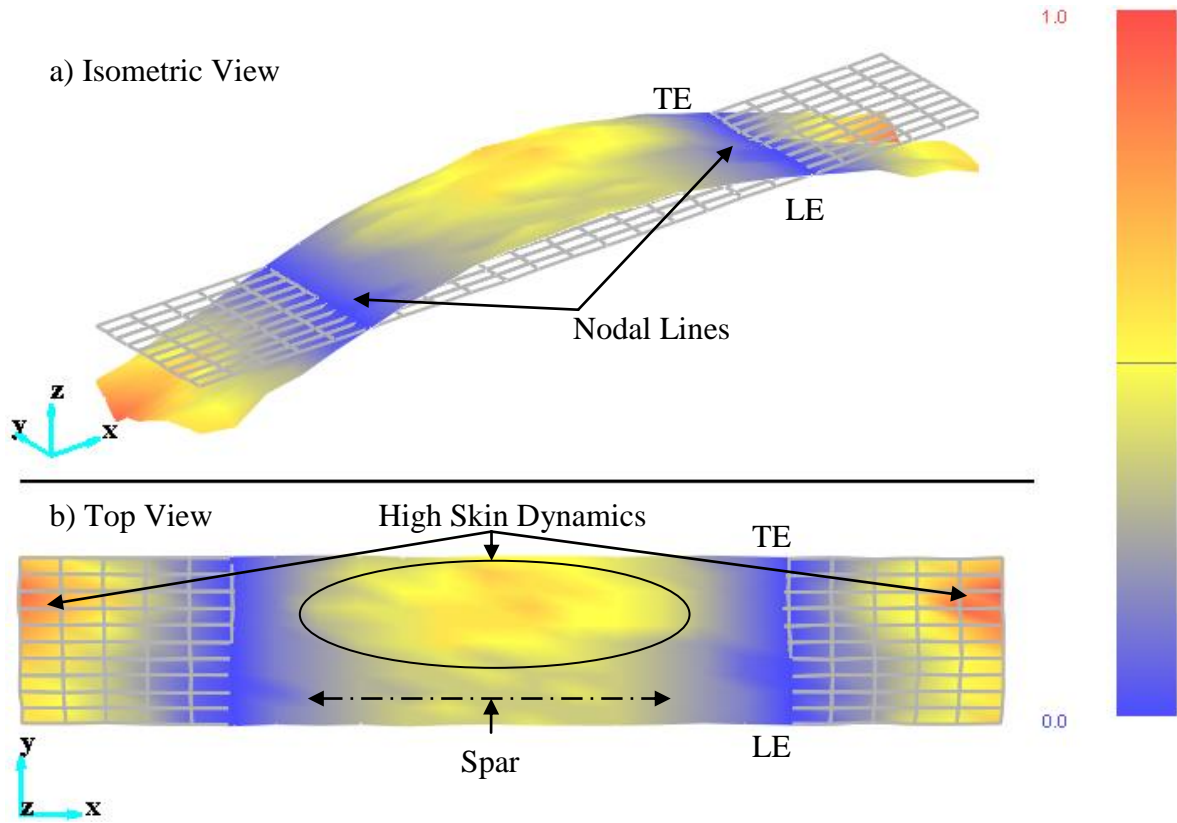
b) Top View

Figure 4-18: Wing Mode 1, Isometric and Top View

4.2.3.2. Wing Mode 2: Bending

a) Isometric View
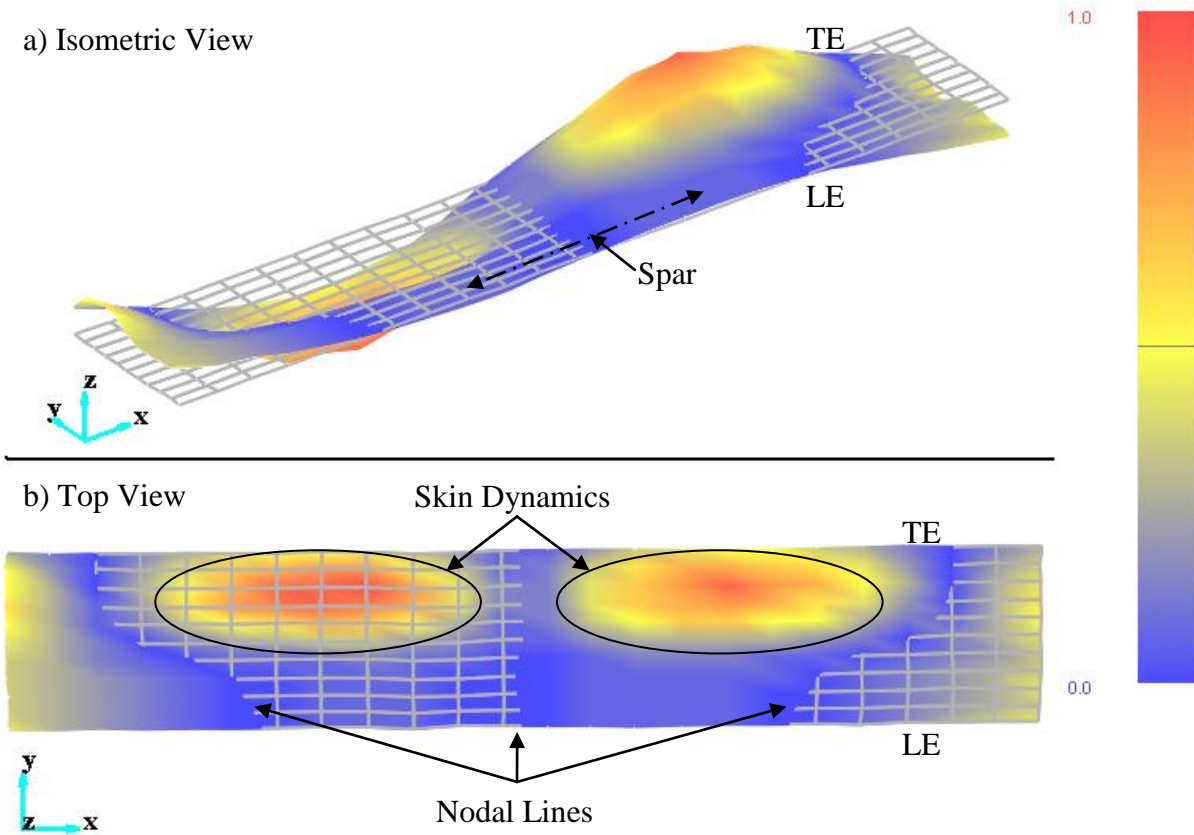
b) Top View

Figure 4-19: Wing Mode 2, Isometric and Top View

The second UAV wing mode is a 2nd order bending mode. There are three nodal lines, two of which are diagonal across the profile and one in the centre.

The shape again becomes more complex towards the trailing edge. Note the two areas of significant skin dynamics. This mode will excite the area of delamination on the pre-damaged wings.

4.2.3.3. Wing Mode 3: Torsional

The third UAV wing mode (figure 4-20) is a 1st order torsional mode. There is a nodal line across the profile in the centre of the wing and one on each end of the wing. The possibility of torsional modes is due to the two 45° plies in the skin giving torsional stiffness to the wing. UAV skins are usually sandwich panels for this reason. This mode will excite the area of delamination on the pre-damaged wings but likely not as significantly as mode 2.
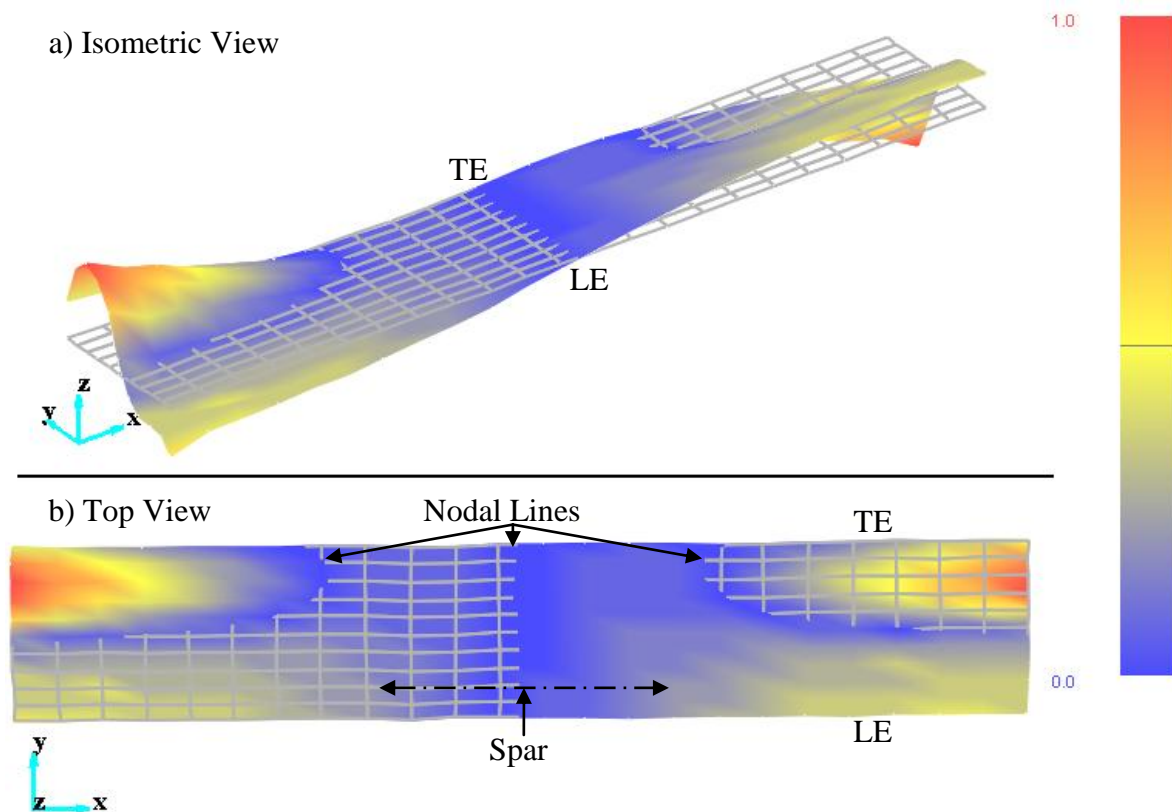
Figure 4-20: Wing Mode 3, Isometric and Top View

4.2.3.4. Wing Mode 4: Bending

The fourth UAV wing mode (figure 4-21) is a combination of a 3rd and 1st order bending mode. It is clear that the modes become more complex with order. The skins clearly show complicated behaviour but the leading edge is excited in 1st order bending due to its increased stiffness from the spar and leading edge shape. The tapered trailing edge offers little stiffness and excites as a 3rd order bending mode.
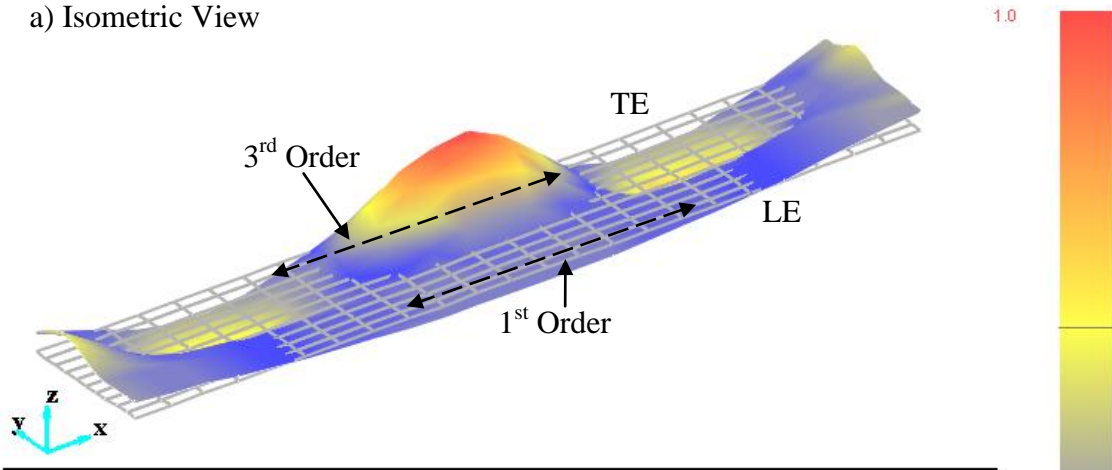
a) Isometric View
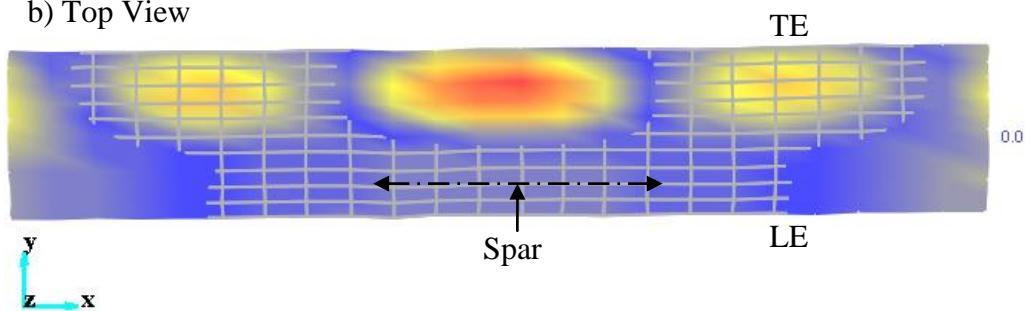
Figure 4-21: Wing Mode 4, Isometric and Top View

4.2.3.5.   Wing Mode 5: Bending
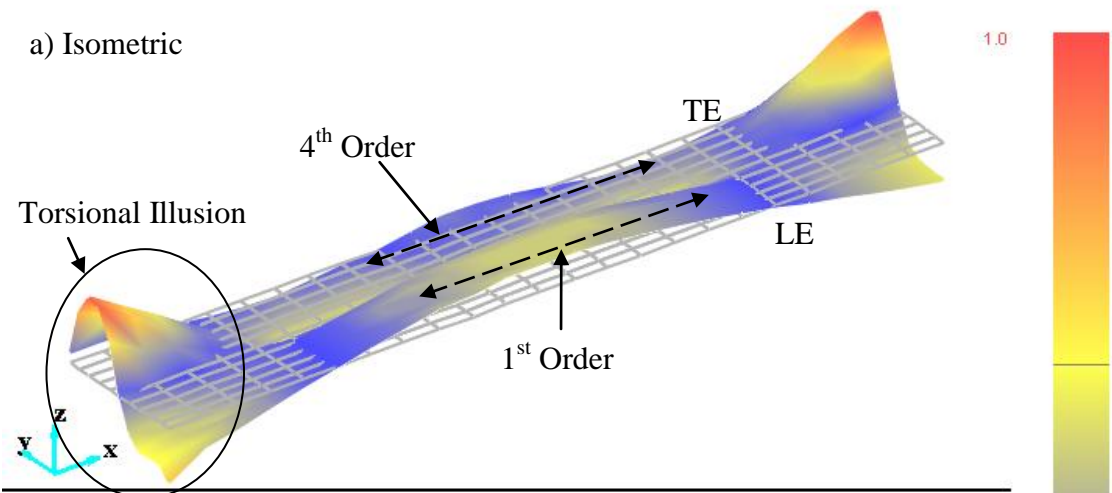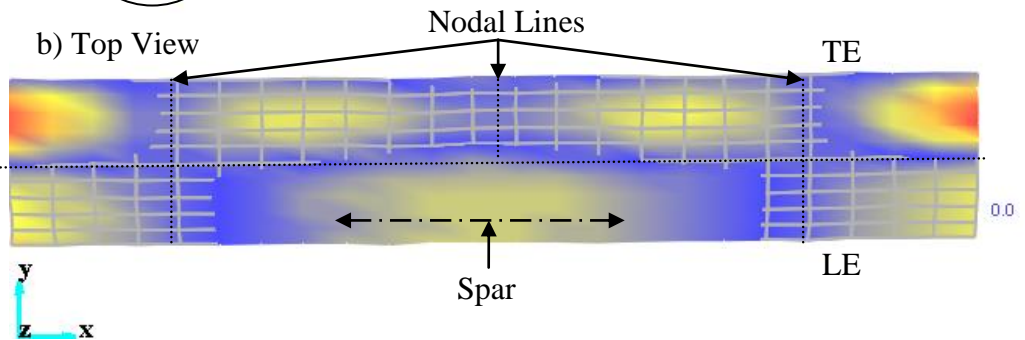
Figure 4-22: Wing Mode 5, Isometric and Top View

The fifth mode (figure 4-22) exhibits the behaviour of a 4th order bending mode while the leading edge is that of a first order bending mode out of phase with the skin by 180° (similar to that of mode 4). This gives the illusion of a torsional mode at the ends of the wing since the magnitude of dynamic behaviour of the leading edge is more appreciable in relation to the skin dynamics, as opposed to the case in mode 4.

It is quite clear that the UAV pre-preg skins are the major dynamic components in this wing design. The skins of common UAVs are sandwich panels which offer more stiffness and will thus likely see higher resonant frequencies and more complex dynamic participation from structural components like the spar in lower order modes.

4.2.3.6. Wing Mode 6: Bending

The sixth mode (figure 4-23) is another bending mode (6th order) and exhibits more complicated skin dynamics than other modes. It is the last mode considered in this modal analysis.
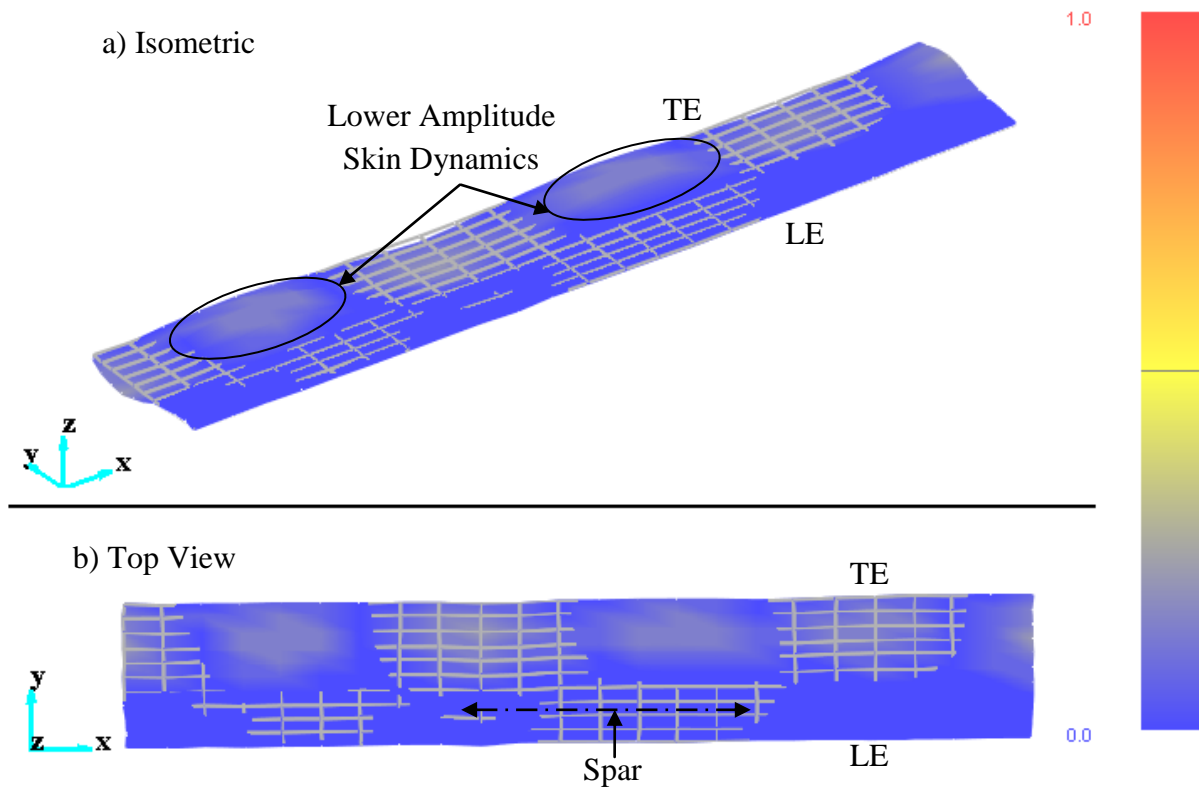
Figure 4-23: Wing Mode 6, Isometric and Top View

5. FE Modelling and Updating

This chapter presents the procedure followed for modelling the Fibrelam and UAV structures as well as updating them to more accurately represent experimental test results. This chapter aims at creating a FE model representative of a standard wing that can be used as a basis for Monte Carlo simulation.

5.1. Finite Element Modelling

Finite element analysis (FEA) is a numerical technique for finding approximate solutions of partial differential equations (PDE) as well as of integral equations. The solution approach is based either on eliminating the differential equation completely (steady state problems), or rendering the PDE into an approximating system of ordinary differential equations, which are then numerically integrated using standard techniques such as Euler's method, Runge-Kutta, etc. The Finite Element Method is a good choice for solving partial differential equations over complicated domains like cars and aircraft.

5.1.1. Elements

The selection of elements in a FEM model is of great importance. All degrees of freedom need to be accounted for while still maintaining as small a model as possible in order to minimize use of solver resources.

In terms of Fibrelam panels, the layup can be captured by a single laminate represented by a layer of quad shell elements. The UAV wings however require a combination of element types. Solid elements easily represent the isotropic characteristic of the resin beads and Roha-cell spar. The skin is approximated using thin shell theory.

5.1.1.1. Shell Elements

Shell elements are either 1D or 2D plane elements and boundary conditions can be applied to the edge or curve of the element. They are especially useful in replacing solid elements in 3D structures were the aspect ratio of thin surfaces are less that 10:1 (Chapelle and Bathe, 2000).

In Patran, the Laminate model is used to describe laminated solids and shells. The orientation of each layer is defined by a single constant angle. Each layer may be a unique material and have a unique constant thickness. The Laminate model uses classical lamination theory to calculate the membrane, bending and membrane-bending coupling stiffness matrices for a laminated shell (MSC, 2008).

In terms of composite laminates, it is recommended not to use mid-noded (second order) elements. The rationale behind this is that the material coordinate system is element shape dependent. Considering figure 5-1, the direction of the x axis of the material coordinate system (x_m) is found by projection of the user defined coordinate system onto the element at

G1. The direction of x_m is calculated by rotating theta degrees from the parametric axis resulting in the direction of x_m to change based on element shape (MSC, 2007).

For this reason, 4 noded quad elements (Q4), with 6 degrees of freedom per node, were used and assigned shell element properties in which the laminates were constructed.
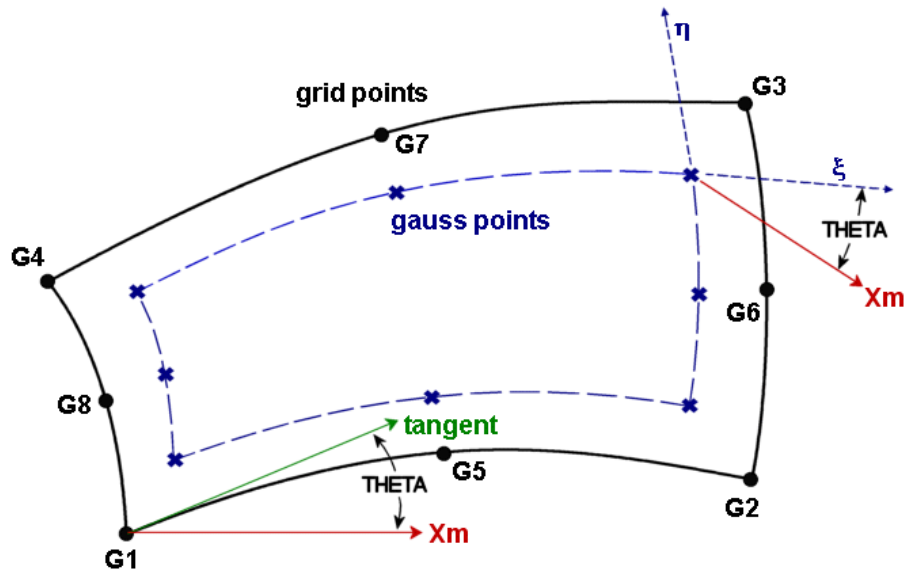
Figure 5-1: Material Coordinate Affected by Mid-noded Q8 Element

5.1.1.2. Solid Elements

Solid elements are 3 dimensional and only have 3 translational degrees of freedom per node. An 8 noded element thus has 24 degrees of freedom of which 6 are rigid body modes. Rotation can be fully accounted for by constraining each of the 3 translational degrees of freedom (Bathe, 1996).

5.1.2. Fibrelam FEA Model

The Fibrelam model was simplified through the assumption that all the layers (skins and honeycomb core) could be represented by thin-shell and laminate theory using 2D orthotropic properties. Two FEM models were developed for multi-model updating and differ only in dimension. These match the geometry of Fibrelam panel 1 which was vibration tested with the modal hammer setup.

5.1.2.1. Geometry and Meshing

The Fibrelam model is depicted by figure 5-2. A single layer of Q4 elements are defined in the x-y plane to represent the rectangular geometry of the panel.

Rectangular Fibrelam Geometry with Q4 Element Mesh
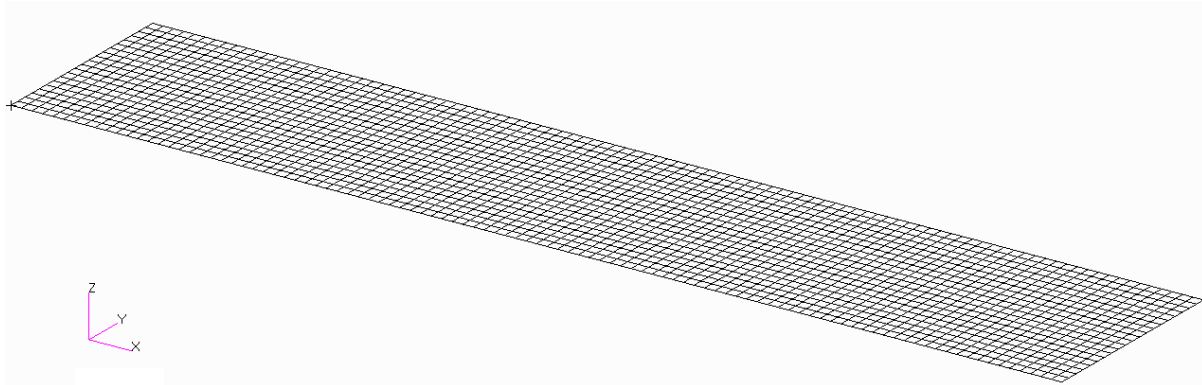
Figure 5-2: Material Coordinate Affected by Mid-noded Q8 Element

There are no constrained degrees of freedom in order to simulate free-free boundary conditions, the result of which is 6 rigid body modes.

The global element coordinate system was defined with the x axis along the length of the panel (global x direction) and the y direction transverse to it (along the global y direction) as in figure 5-3. This was done in correlation with 0° and 90 °orientation of the tensile coupons manufacture from the panel skins.
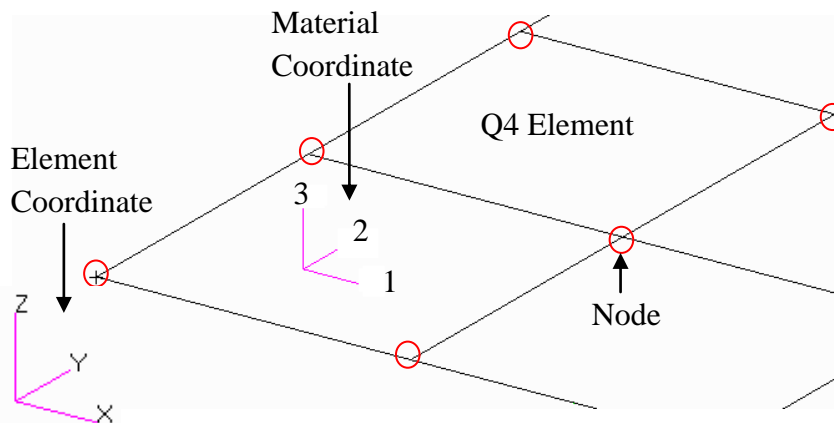
Figure 5-3: Material Coordinate Definition

5.1.2.2.   Material Definition

The definition of the laminate material is done in two steps. Each material is defined as a 2D orthotropic ply. These are then stacked into a composite laminate with necessary orientation and thickness.

4.1.1.1.   Fibrelam: 2D Orthotropic Definition

The two main components of the Fibrelam being the skins and the honeycomb, two materials thus have to be defined. Under the assumption that both the top and bottom skins are from the same batch and have undergone the same manufacturing cycles, the properties are summarised in table 5-1 below. Properties from panel 1 were used.

Table 5-1: 2D Orthotropic Fibrelam Properties

Property	E_1	E_2	G_{12}	v_{12}	ρ
Units	[GPa]				[kg/m^3]
Fibrelam Skin	16.67	16.79	3.16	0.18	1546.64
Honeycomb	0.04	0.025	0.01	0.2	48

4.1.1.2. Fibrelam: Laminate Definition

Figure 5-4 is an extract from Patran showing the laminate layup of the panel. The orientation angle is the offset between the 0° ply direction and the material 1 axis direction. In the case of the Fibrelam panels, these coordinates coincide and thus all the ply orientations are 0°. Ply thickness is given in SI units (metres). No offset is defined and thus the elements lie in the centre of the ply thickness.

	Material Name	Thickness	Orientation
1	skin1	7.000000E-4	0.000000E+0
2	core	1.140000E-2	0.000000E+0
3	skin1	7.000000E-4	0.000000E+0

Figure 5-4: Fibrelam Ply Stacking

5.1.3. UAV Wing FEA Model

The challenge presented by the wing was that of creating an accurate SD8020 aerofoil profile and then meshing the complex structure with interfacing spar, resin beads and skins. Considering again that there are 3 different materials available for model updating and in correlation with the 3 different wing lengths that were vibration tested, 3 FE models were thus created varying only in length, the profile and chord lengths were kept intact.

5.1.3.1. Geometry

The aerofoil profile was created in the Patran interface by a Matlab generated session file. 300 individual points spread along the circumference of the aerofoil profile were extracted from XFLR5 v4.1.7. XFLR5 is a free release analysis tool for airfoils, wings and planes operating at low Reynolds numbers (Deperrios, 2009).

These extracted points were adjusted for aerofoil chord length and then defined in Patran by the session file in the x-z plane and linked to form a top and bottom skin profile. These profiles where then extruded to form skin surfaces.

5.1.3.2. Meshing

The fully meshed wing model is shown in figure 5-5. The laminate aerofoil skins were meshed with Q4 shell elements. The resin beads that bond the spar and skins of the UAV wings together were modelled using 8 noded Hexagonal (Hex8) solid elements.

The Roha-cell spar was also modelled using Hex8 solid elements because of the volume of the spar (thickness) and for sensible node equivalence between material surfaces.

UAV Wing FE Model
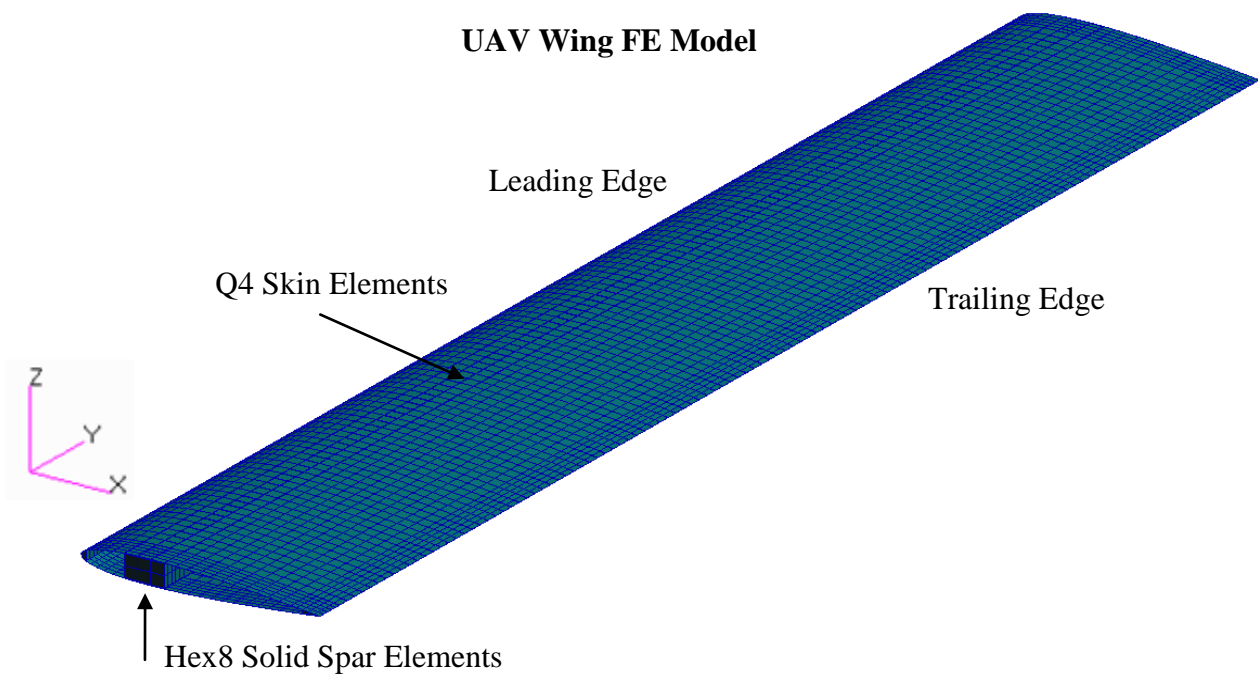
Figure 5-5: Fully Meshed UAV Wing Structure

The curve of the aerofoil at the leading edge was cause for caution. The length to width aspect ratio of shell elements (L to W) are typically required to stay within a 1 to 4 ratio. The reason for this restriction is that if the element stiffness in two directions is very different, the structural stiffness matrix has both very large numbers and almost zero numbers on the main diagonal. As a consequence the computed displacements and stresses may have little accuracy (Cook, Malkus and Plesha, 2002).

The aspect ratio of the Q4 shells was kept less than 1 to 3. Figure 5-6 shows the effect of the aerofoil shape on the element size.
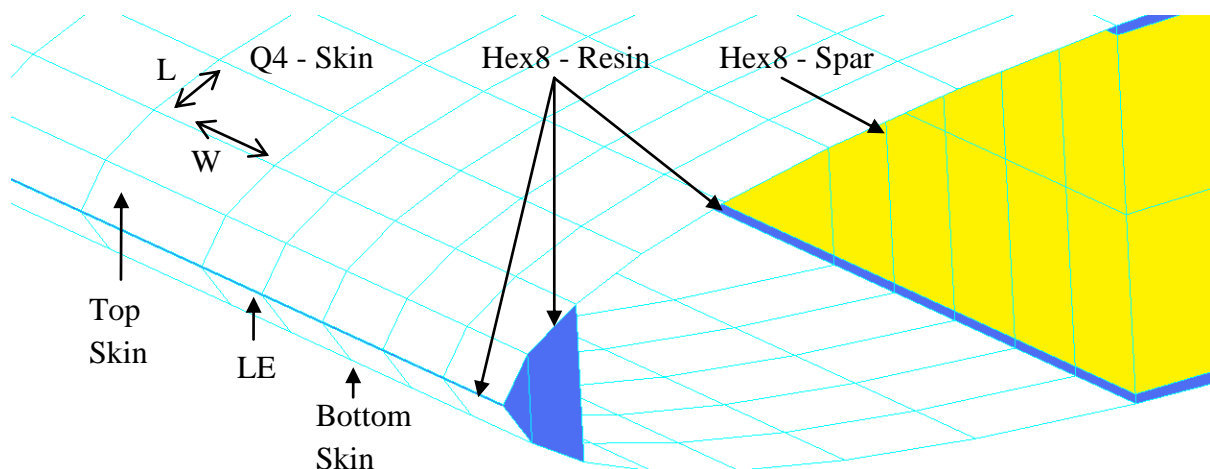
Figure 5-6: Leading Edge Meshing

In order to capture the gradient change of the curve more precisely, elements had to be made smaller in this area. Elements were allowed to be larger at the trailing edge due to a smoother slope. As a result of interaction of small and large elements, aspect ratios were affected.

Considering the aerofoil profile section in figure 5-7 below, the resin beading was modelled in all 6 areas of application.
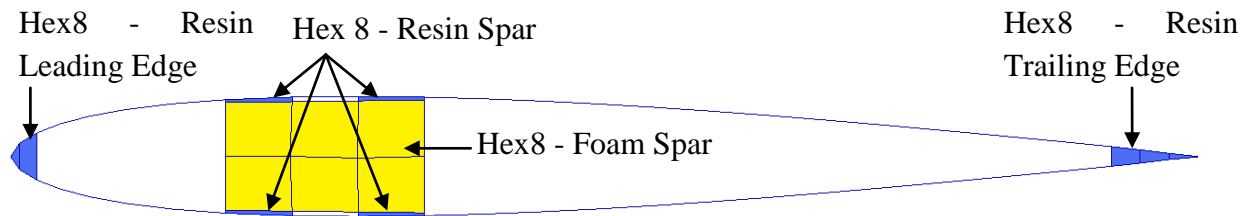
Figure 5-7: FE Model Resin Application

Hex8 solid elements were used for two main reasons. Firstly, these elements provide a distribution of the resin mass rather that to confine it to nodes on a 1D beam element. Secondly, the stiffness of the resin can be taken into account. Figure 5-8 shows a Hex8 resin element at the wings trailing edge. Note that the Q4 skin elements lie directly on top of the Hex8 resin elements and are shown apart in the figure for explanatory purpose.
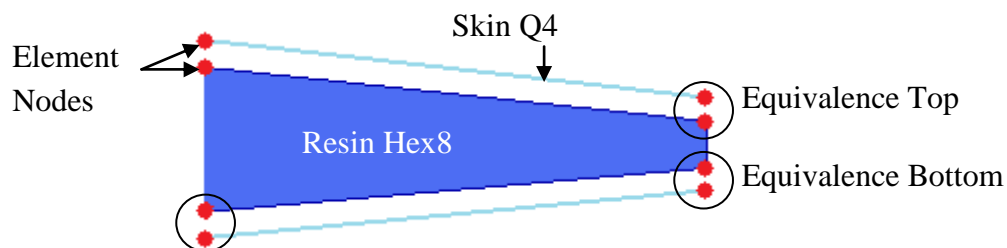
Figure 5-8: Resin Equivalence

The nodes associated with the top skin are equivalence (shared) with the nodes at the top of the resin Hex8. Similarly the bottom nodes are shared with the bottom skin. This configuration allows for the stiffness of the resin beading to be taken into account, rather than just to equivalence all nodes at the trailing edge.

In a similar fashion, the nodes at the leading edge and at the spar-skin interaction areas are linked using equivalence.

5.1.3.3.   Material Definition

Materials defined for the wing model include both isotropic and 2D orthotropic assumptions. Roha-cell foam has the same properties in all directions and is thus considered isotropic, as does the Epolam 2022 resin beads. The pre-preg glass laminate was defined in Patran in a similar fashion to the Fibrelam panel. Material properties used can be found in table 3-9.

A laminate offset was also specified. Since the Hex8 resin elements were defined directly against the skin Q4 elements, which have thickness, it was necessary to apply an outward offset to the skins in order to avoid simulating overlapping.

5.1.3.4. Convergence

The convergence of the wing FE Model was done by reducing element edge lengths by roughly 50% for each model and thus increasing the number of elements in the mesh. The purpose of this exercise is to ensure that the model approximates the actual structure with as little numerical error as possible. The average of the first 5 natural frequencies was used as a basis for model convergence. Table 5-2 gives the percentage mean frequency difference between each model and the most refined solution (model 5).

Table 5-2: UAV Wing Model Convergence

FE Model	1	2	3	4	5
Element Length [mm]	0.04	0.03	0.02	0.01	0.005
# Nodes	760	574	1586	6534	31812
# Elements	330	600	1560	6240	29760
Mean Freq. Difference	1.95%	1.78%	0.29%	0.18%	*

The 4th model converged to less that 0.2% mean frequency difference. Note the large increase in elements between model 4 and 5 with only a small frequency change. With model 5 assumed the exact solution; model 4 was selected as the converged model with an acceptable 0.18% average frequency error over the first 5 modes.

The rate of convergence, calculated from a linear log-log fit (R^2 fit value of 90%) of the average percentage difference in frequency vs. the number of additional elements per model, is a gradient of -0.6 (figure 5-9).
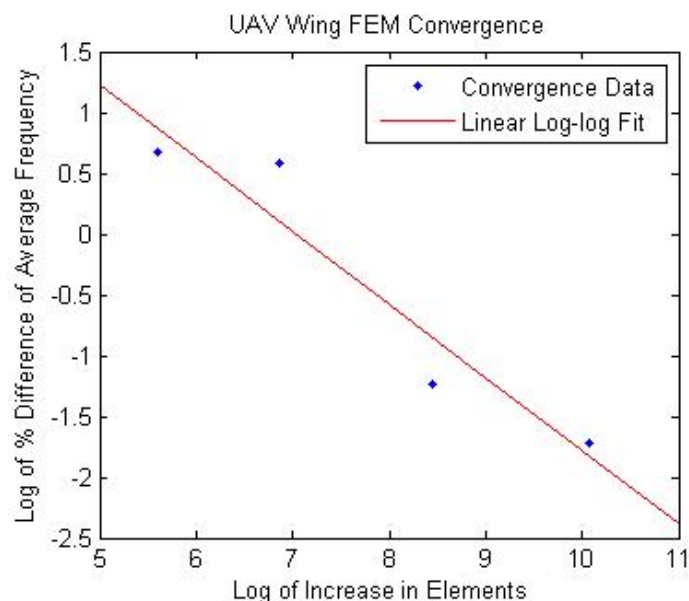
Figure 5-9: UAV FE Model Convergence Rate

FEA results are given in the next chapter and compared to modal analysis results from experimental testing sine the FEMtools solver was used for normal modes analysis.

5.2. Model Updating

The purpose of this section is to adjust the FEM models to have better correlation with experimental results. This allows for (in terms of global parameters) non-destructive material property extraction.

Model updating will help to adjust less sensitive material properties which are not defined in distributions and will not vary in Monte-Carlo simulation. The result will be FEM models with some updated but deterministic parameters not just faithfully taken from datasheets.

Since the wing pre-preg skins are now well defined, those parameters that largely affect variability of wing responses and vary largely themselves help to show model validity by comparing the updated values to well defined distributions.

Model updating was performed using the FEMtools software package. This chapter follows this procedure and presents the relevant results attained. Fibrelam update results can be found in appendix F. Only UAV wing updating is presented here.

5.2.1. Multi-model Updating

Preparation for multi-model updating has been the path linking all previous chapters. The three main structural components of the wings (skin, spar and resin beads) have necessitated manufacture and testing of three different wing geometries (length variation) and corresponding FE analysis.

5.2.1.1. FE Models

The wing FE model was imported into the FEMtools database and normal modes analysis performed using the FEMtools solver. Generation of FRFs required modal data including mode shape, frequency and an estimate modal damping factor, which was taken as 0.4% based on experimental modal results (table 4-5).

The appropriate FEM element nodes had to be correlated with the experimental measurement points (reflective stickers) in order to generate the correct FRFs. Boundary conditions relating to excitation position were defined and FRFs generated based on the modal data for the first 6 modes. Figure 5-10 is a FEMtools extract showing an FRF generated at the node corresponding to scan point 1 superimposed on the experimental FRF from scan point 1 on the undamaged UAV wing 1.

It immediately seems that the responses are similar but shape and amplitude correlation (equations B-1 and B-2, Appendix B) indicates large error of around 60%. The FE FRF is

shifted to the right of the experimental. It is possible that either stiffness has been overestimated or density values are too low or both.

None the less this figure at least shows similarity between FEA and EMA. The procedure was performed for all three model sizes. The next step was to select response parameters, keeping in mind that there needs to be at least one response per updating parameter in each of the three models.
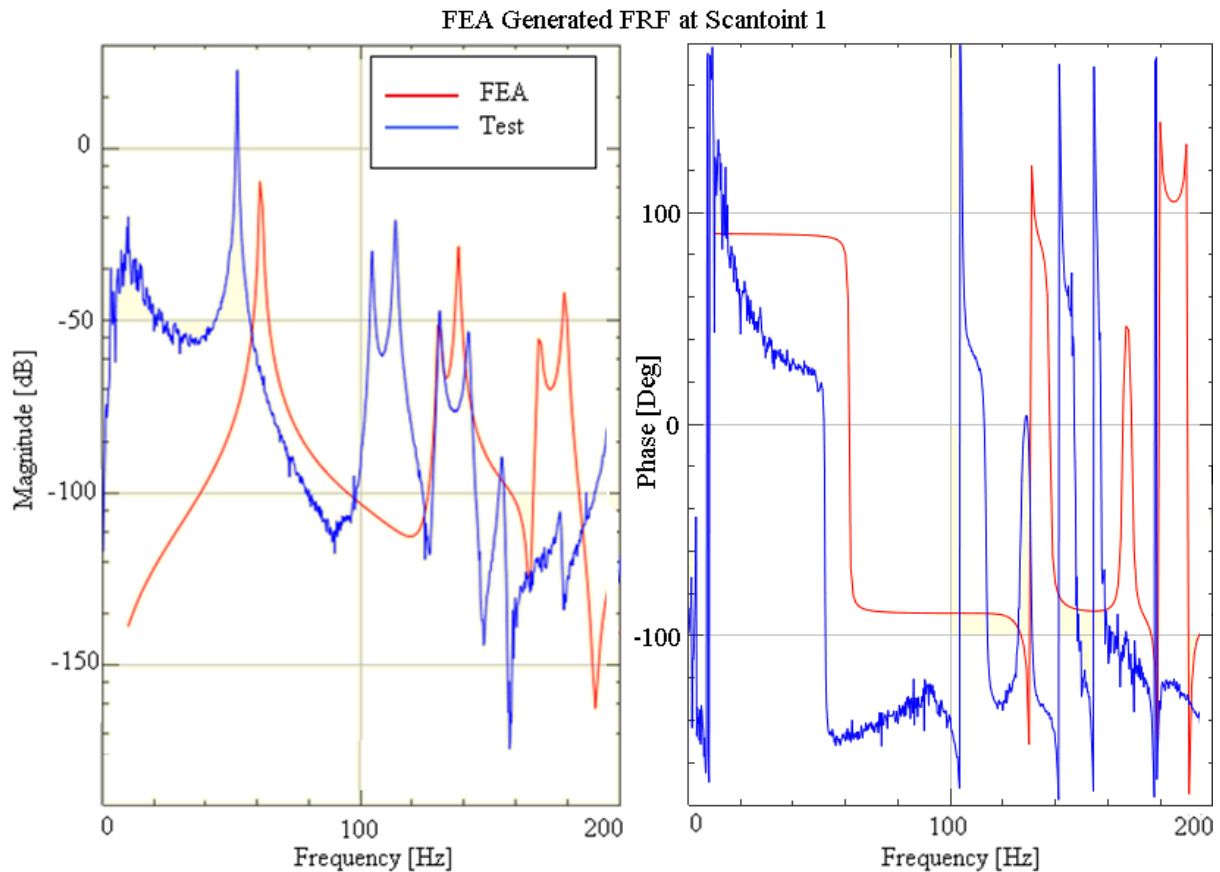
Figure 5-10: Superposition of FEM FRF on Experimental FRF

5.2.1.2. Response Selection

Possible responses are frequency, modal, MAC and FRF correlations. FRF correlation updating is useful but is expensive in solution time while using only frequencies does not supply enough response. It was therefore decided to use both frequency and modal shape response correlation.

5.2.1.3. Sensitivity Analysis and Parameter Selection

The relative-normalised sensitivity matrix in figure 5-11 shows the sensitivity of 11 global material parameters relative to 12 FEA responses of the full size FE wing model. Note update parameters are required to be the same for all models involved in a multi-model updating routine. Table 5-3 gives a list of the parameters and responses presented in figure 5-11.

The figure shows that the model responses are less sensitive to the foam and resin bead material properties than to that of the skins. Skin density and elastic moduli have the largest effect on FEA responses however foam and resin density do have some effect on mode shape response which has to be considered.

This analysis supports the approach that some update parameters can considered to be deterministic with little consequence due to their low sensitivity. It is still wise however to update them rather than trust datasheet values. Parameters that show high sensitivity are most important to update as they have now been well defined in probabilistic distributions and can validate the update result. Thus all 11 parameters in table 5-3 were updated using the multi-model updating procedure.

Table 5-3: Parameters and Responses

#	Parameter	Sym.	Response
1	Spar Elastic Modulus		Freq. 1
2	Resin Elastic Modulus	E	Freq. 2
3	Skin Density	ρ	Freq. 3
4	Foam Density	ρ	Freq. 4
5	Resin Density	ρ	Freq. 5
6	Spar Shear Modulus	G	Freq. 6
7	Resin Shear Modulus	G	Mode 1
8	Skin Elastic Modulus	E_1	Mode 2
9	Skin Elastic Modulus	E_2	Mode 3
10	Skin Shear Modulus	G_{12}	Mode 4
11	Skin Poisson	ν_{12}	Mode 5
12	*		Mode 6
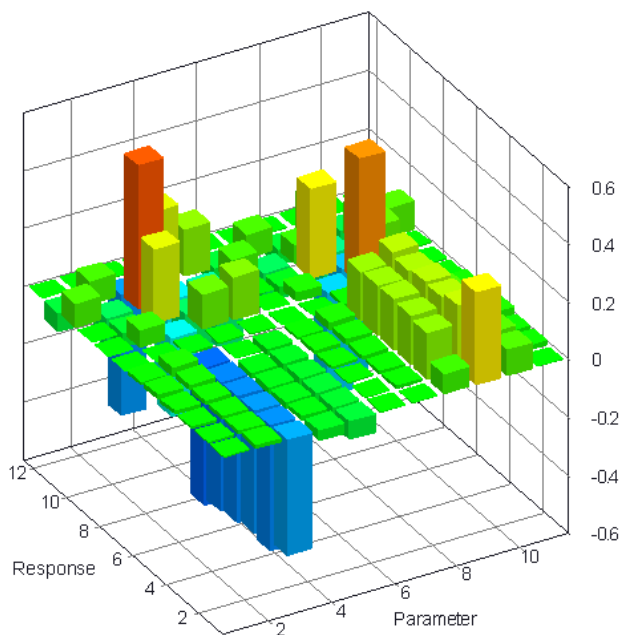
Figure 5-11: Relative-normalised Sensitivity

Note though that Poisson's ratio for isotropic materials is not selected as an updating parameter but is however still considered though its relation to elastic and shear modulus in equation 2.6.

5.2.2. Updating Result

5.2.2.1. Updating Convergence

Model updating convergence was set to obtain the best possible result within a reasonable solution time. It was discovered that the updating procedure easily attained a correlation coefficient (CCABS) difference between FEM and experimental frequencies of 2% for all three models and 1.4% for the full size model in 5 iterations. Mode shape correlation difference was 4%. Updating terminated when CCABS improvement between iterations was less that 0.1%.

Figure 5-12 depicts the frequency correlation improvement and the convergence sum of the change in material property update parameters.
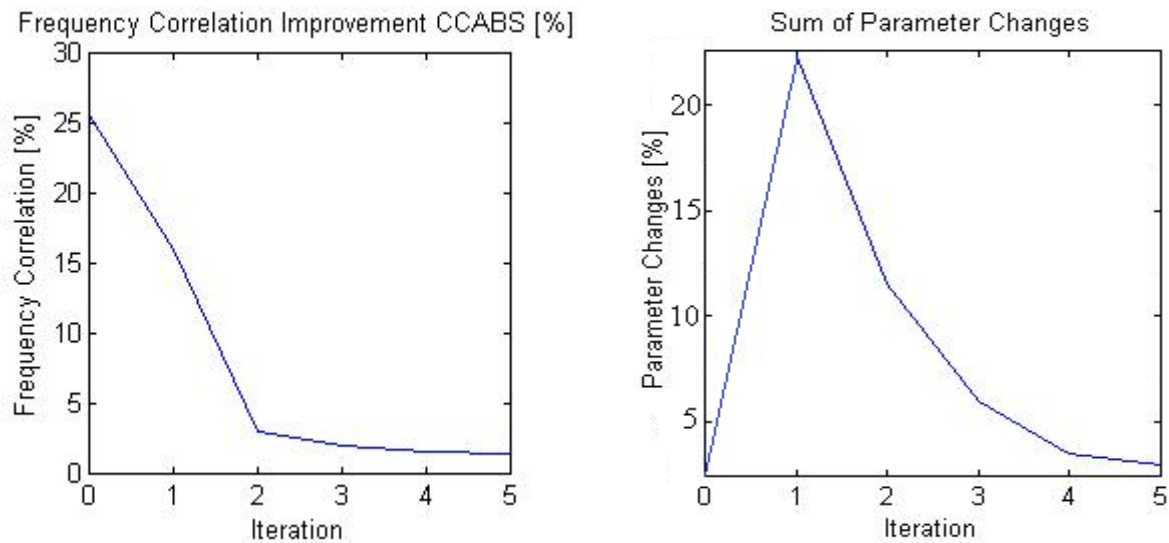
Figure 5-12: Multi-Model Updating Convergence

5.2.2.2. Updated Response

- Frequency and MAC

Table 5-4 gives the EMA and FEA values of the natural frequencies and table 5-5 the diagonal of the MAC matrices for the 6 updated modes before and after updating.

Table 5-4: Updated Natural Frequency

Mode	EMA [Hz]	FEA Before [Hz]	% Diff.	FEA After [Hz]	% Diff.
1	52.2	61.4	17.6%	50.8	2.7%
2	104.4	130.4	24.8%	103.3	1.1%
3	113.6	137.9	21.4%	112.8	0.7%
4	130.6	169.2	29.5%	132.4	1.3%
5	141.9	179.3	26.4%	142.2	0.2%
6	155.0	207.1	33.6%	158.4	2.2%

Table 5-5: Updated MAC

Mode	Before	After	Improvement
1	99.3%	99.4%	0.1%
2	92.8%	98.7%	5.9%
3	91.9%	98.1%	6.2%
4	82.7%	98.9%	16.2%
5	78.9%	98.3%	19.4%
6	94.2%	94.4%	0.2%

The average frequency error is under 2 % with only the first and last modes under 3%. This is a significant improvement from errors as large as 33 percent. The general trend is a drop in frequency to match FEA response. The modal assurance criterion also shows better

correlation between FEA and EMA mode shapes. Figure 5-13 is a graphic representation of the MAC matrices showing value decrease with modal order.
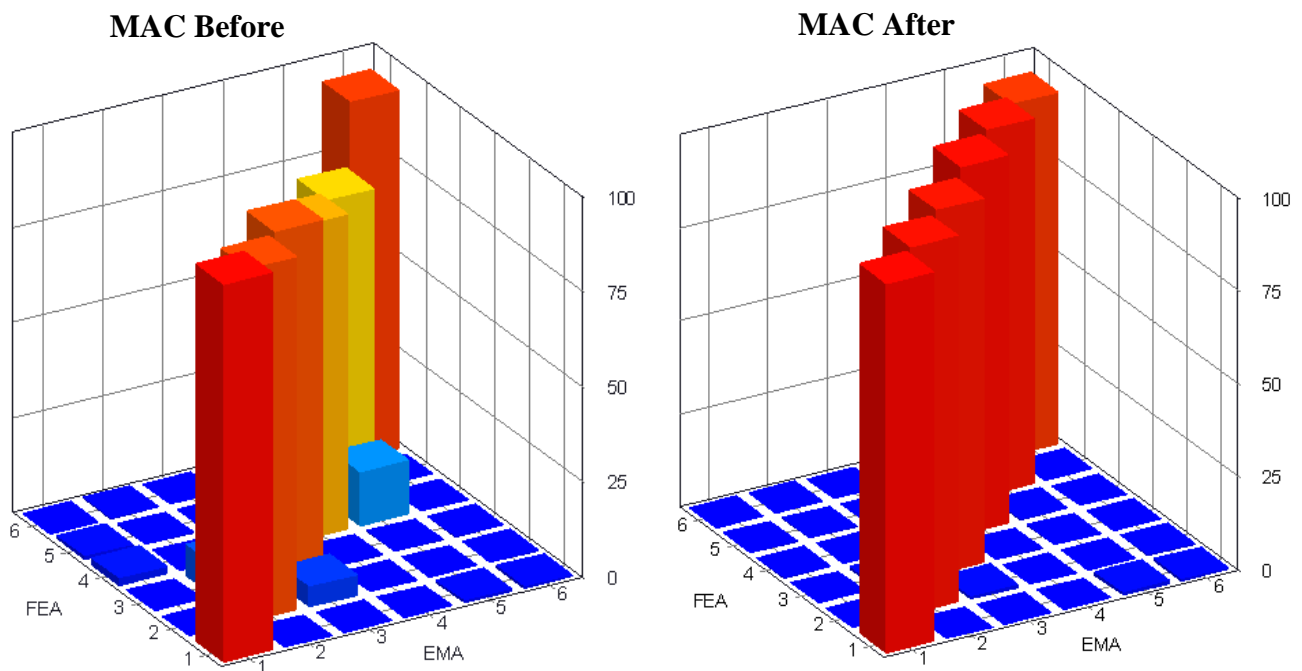
Figure 5-13: UAV Wing MAC

A superimposed graphical view (figure 5-14), of the actual modes shapes, give visual evidence of model updating. The figure is that of mode shape 2, a second order bending mode with an updated MAC value of 98.7%.
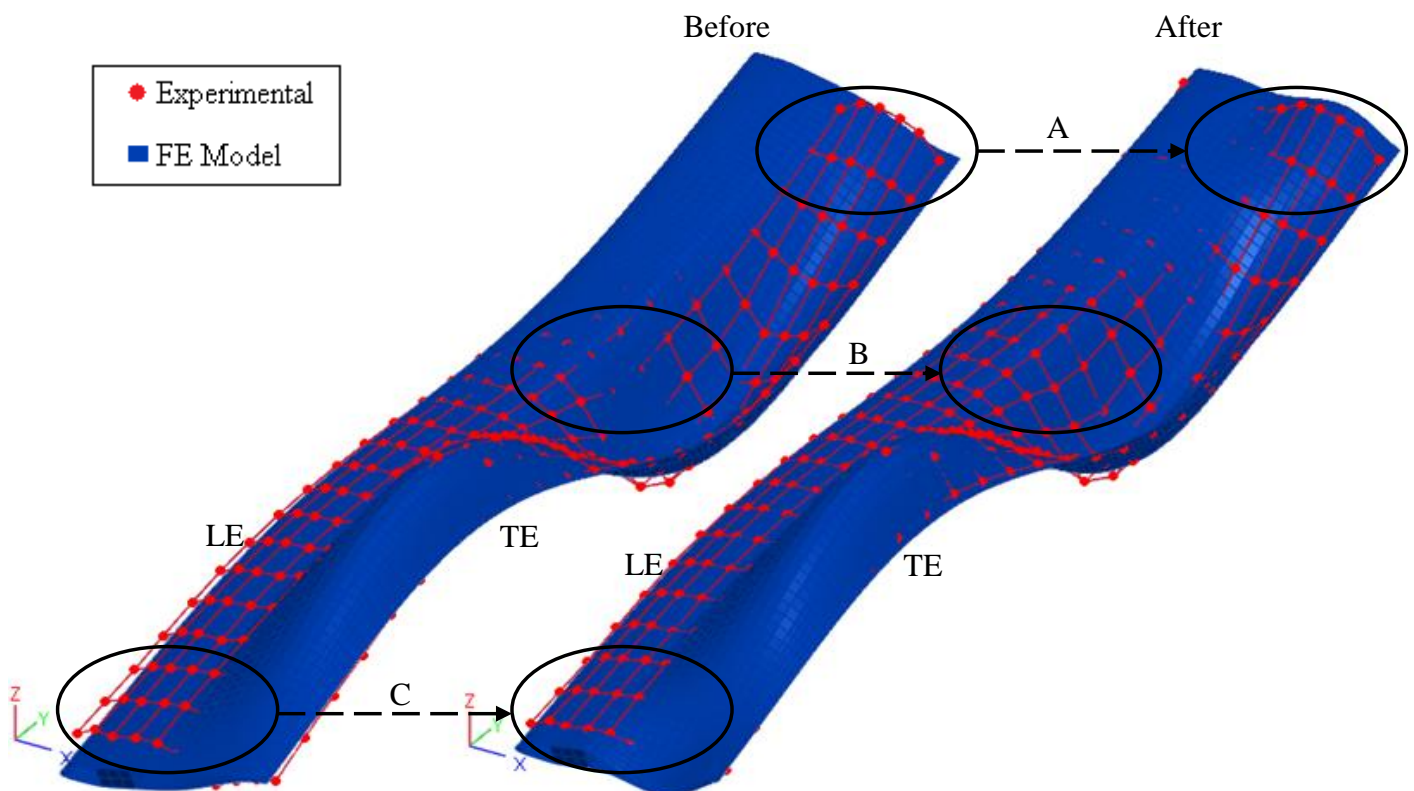
Figure 5-14: Superimposed 2nd Order Bending Modes

The figure shows three areas of updating improvement. Areas A, B and C draw attention to better superposition of the FEM nodes in blue and the EMA scan points in red. The figure on the left is before and that on the right after updating.

A FEA FRF now generated from updated modal responses superimposed on a test FRF, shows a significantly better fit in figure 5-15 (Need better quality, Extract from FEMtools).
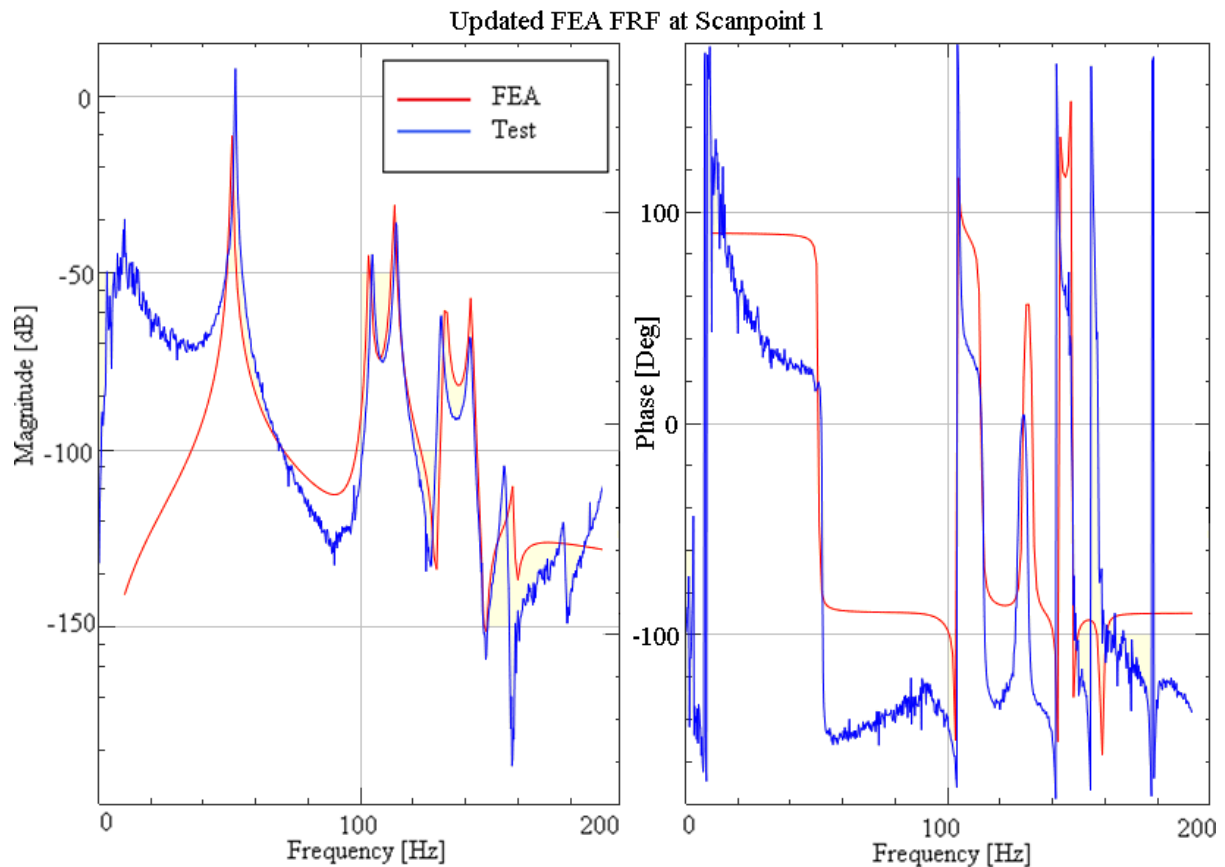
Figure 5-15: Superposition of Updated FRF

Note that the mode peaks and anti-resonances are captured. Observation also supports the statement that higher order modes are more difficult to simulate accurately. The largest MAC error occurs for the 6th mode shape.

It is quite clear that the model updating has succeeded in finding better correlation between the FEM and EMA responses. The only aspect not attended to yet is that of damping.

In order to address damping, it was necessary to first update parameters affecting mode shape and frequency. FRF correlation coefficients can now be used to better match FRF's. The Cross Signature Scale Factor (CSF) criterion (equation B-2, Appendix B) is sensitive to FRF amplitude and is thus suited to updating modal damping factors.

This section presents the pre-updating parameter values and compares them against the post-update values. The variance from the tensile test mean of the updated values are then check against the distribution variance.

Consider table 5-6. The update parameters are presented with their corresponding pre and post updating values. The isotropic values are those now considered correct and deterministic. The largest parameter change from multi-model updating is that of the spar with 33% density change. It would seem that the initial estimates were too high. It is possible that incorrect manufacturer information was considered and different foam was used as originally thought. In fact the results show the foam parameters to converge closer to values of Roha-cell 51 than that of Roha-cell 71 originally thought to be used. Refer to Appendix D.3 for additional datasheet info.

Table 5-6: Updated Material Property Parameters - UAV Wing

	Foam Spar			Resin Beading			Pre-preg Skin				
Units	GPa		kg/m^3	GPa		kg/m^3	GPa			*	kg/m^3
Parameter	E	G	ρ	E	G	ρ	E_1	E_2	G_{12}	v_{12}	ρ
Before	0.09	0.03	75	3.4	1.41	1170	18.65	20.21	3.34	0.16	1087
After	0.07	0.02	50	4.38	1.52	1480	19.43	21.36	3.83	0.15	1244
% Change	22.2%	20.0%	33.3%	28.8%	7.8%	26.5%	4.2%	5.7%	14.7%	6.3%	14.4%

The updated values of variable parameters (skins) show less change. The trend though is higher stiffness in all the skin modulus parameters. It would seem from this table that the estimates for skin modulus were slightly lower than those identified for wing 1. This is possibly due to the curing cycle process, as was the case with batch 6 of the tensile test coupons; refer to figure 3-28.

The necessity to lower the FEM frequencies to match FEA response is an explanation for the drop in converged stiffness values of the spar and increased density for the resin and skin. This result is typical of the compromise necessary between improving response correlation and converging parameters to reasonable values.

5.3. Validating the FE Model

Consider now the statistical box plots in figure 5-16. Plotted are the quartiles of the five pre-preg property distributions. Superimposed on them are the updated property values.

The updated pre-preg material property values all lie between the 3rd and 4th quartile except for Poisson's ratio which lies between the 2nd and 3rd quartile. This simple visual construction easily illustrates that while the values of stiffness and density extracted for UAV wing 1 are larger in value than the mean distribution values, they still belong to the same material distribution.
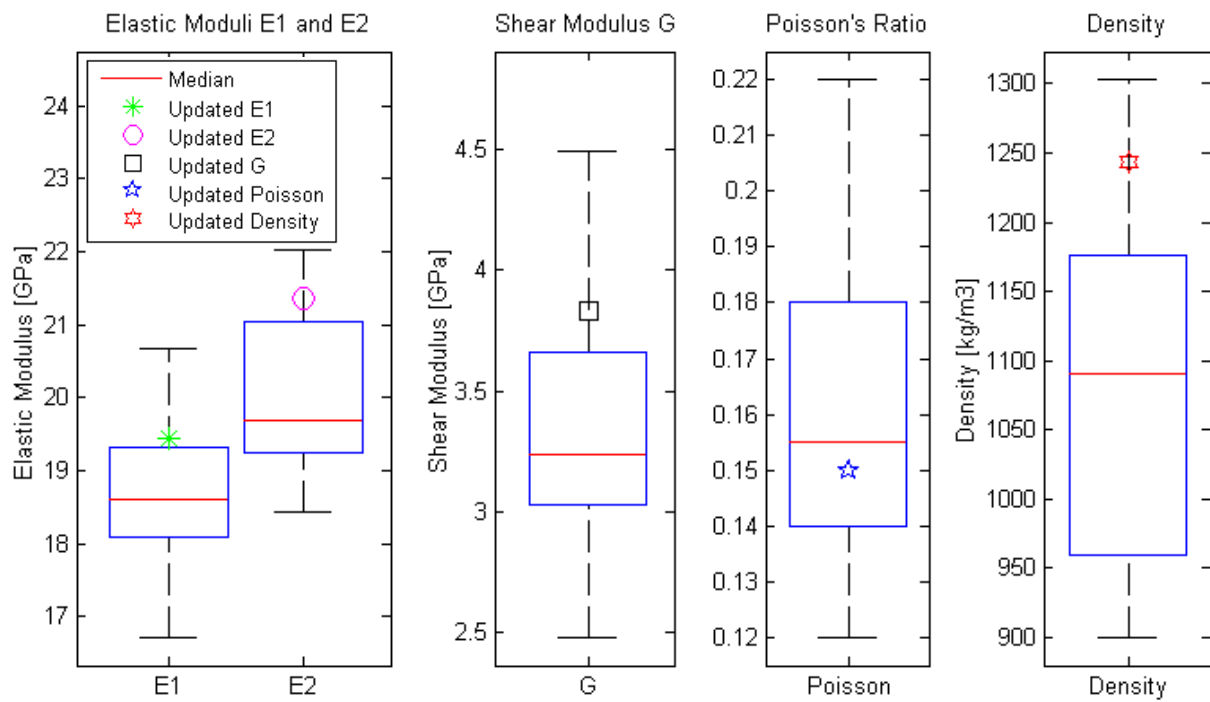
Figure 5-16: Material Distribution Box Plots

Considering that the deterministic properties converged to sensible values and the stochastic material properties converged to lie in the defined material distribution. It leads to conclude that the FE model is representative not only of wing 1 but can be used as a basis to vary the stochastic material properties and represent an entire production line of these UAV wings.

6. Probabilistic Analysis

This chapter has two main objectives. Firstly a Monte Carlo simulation is performed to ascertain the effect of material variability on modal response. The definition of a confidence region on modal responses is then used in case studies to verify if undamaged wing responses fall within this confidence region and whether damage can be detected.

6.1. Monte-Carlo

Finally now that a FE wing model has been updated and is representative of an undamaged UAV wing, the most sensitive and variable parameters can be made to vary in a Monte-Carlo simulation. This section generates the required parameter distributions, runs the simulation and defines the necessary probabilistic modal vibration responses.

6.1.1. Probabilistic Parameters

FEMtools has a Monte-Carlo simulator and generates input parameters based on the mean, standard deviation and distribution type. Since the all the 2D-orthotropic properties of the pre-preg skins were defined, it was decided to include Poisson's ratio as a probabilistic parameter despite its lower sensitivity value.

Table 6-1 below gives the mean and standard deviation % or coefficient of variance (COV) values of the variable parameters from tensile tests. These are calculated from the material property mean values for each of the six tensile coupon batches. FEMtools was used to generate 200 normally distributed values for each parameter. Thus 200 Monte-Carlo simulation cycles were completed to attain 200 different modal responses.

Table 6-1: UAV Wing Variable Parameters

Parameter	E_1	E_2	G_{12}	v_{12}	ρ
Units	[GPa]				[kg/m³]
Mean	18.65	20.21	3.34	0.16	1087
COV	3.2%	3.2%	11.4%	7.6%	12%

The Monte-Carlo process is performed entirely in FEMtools and is a simple process. Firstly the variable parameters are specified with variance as in the table above. The second operation is to generate normally distributed parameter values which adhere to the standard deviation limits. And finally these 200 sets of parameter values are iteratively plugged into the FE model and solved.

6.1.2. Probabilistic Response Construction

The main modal responses attained from the Monte-Carlo Simulation are natural frequency and mode shape. Since the practicality of using frequency as a damage detection tool has been ruled out, the focus is set on mode shape variability.

6.1.2.1. Wing Geometry Grid

First consider the wing geometry in figure 6-1. The wings were scanned at 264 locations and thus the 264 corresponding FEM nodes produce a modal response. The geometry is divided up into a grid of 11 rows and 24 columns. Each of these points has a distribution of mode shape deflection data for the first 6 mode shapes.

By plotting the modal response along a row or column of the wing geometry, a 2 dimensional modal response slice (line mode) can be obtained and easily inspected. A slice along a specific column is a cross-section through the wings aerofoil profile.
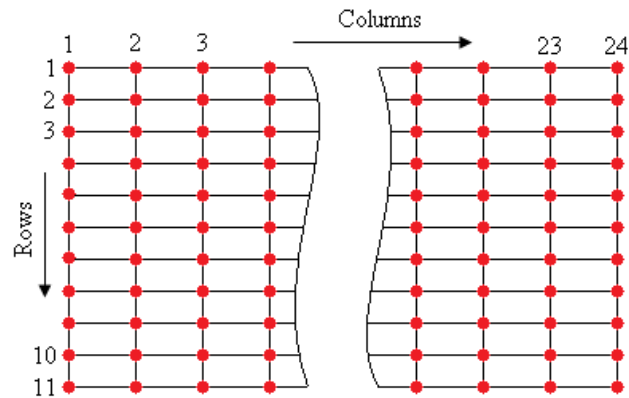
Figure 6-1: UAV Wing Geometry Grid

6.1.2.2. Confidence Bounds

In order to construct confidence bounds using equation 2.29, the data must be proved to follow a normal distribution. The mode shape deflection distribution for scan point 191 (Column 18 row 4) is plotted below on a normal probability plot (figure 6-2) to validate this.
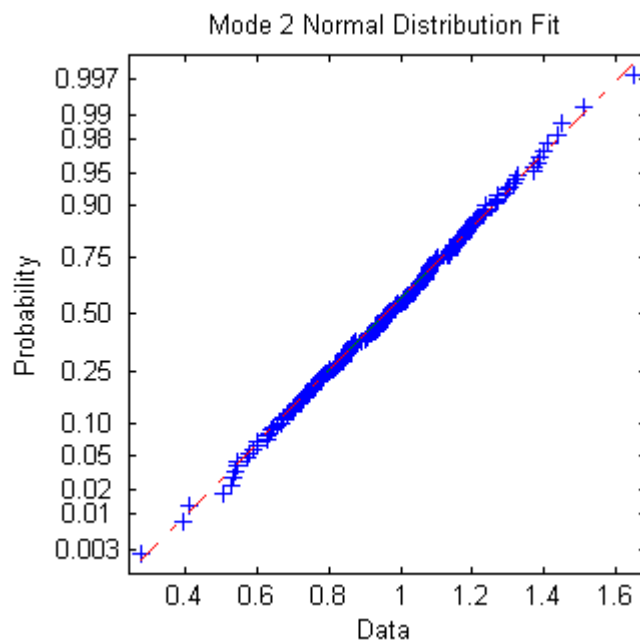
Figure 6-2: Mode 2 Distribution

Confidence bounds for modes shape responses were established with 90% confidence on sample variance from the sample mean, using equation 2.29 and $t_{\alpha/2,n-1} = 1.645$ (table A-3, Appendix A).

Presented below are the mode shape confidence bounds for modes along column 18. This slice is selected because it is located approximately quarter way down the length of the wing and roughly at the centre of the delaminations. Recalling from section 4.2.3.2 on modal analysis, wing mode shape 2 is a 2nd order bending mode with its maximum response magnitude at this slice location. Figure 6-3 shows the mode shape confidence region with the mean value.

The modes were normalised with respect to the mean response values for mode shape 2. The large skin dynamics are immediately clear from the figure and decrease nearer the leading edge as expected.
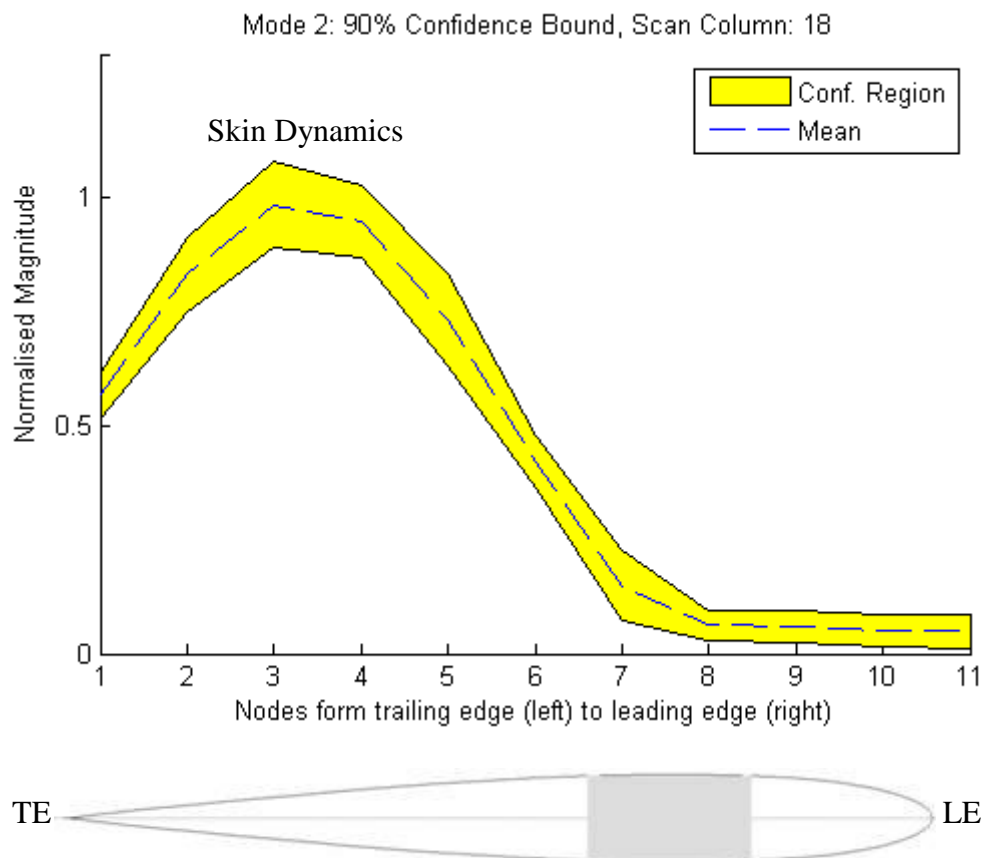
Figure 6-3: Line Mode 2 Confidence Region at Grid Column 18

The mean coefficient of variance for mode 2 along grid column 18 is 48%. This illustrates large variation in mode shape dynamics resulting from skin property variation.

Mode shape 1 (1st order bending) in figure 6-4 clearly shows narrowing at both trailing and leading edges. The magnitude of mode shape deflection for this line mode is low due to it being located near a nodal line. The coefficient of variance for the high skin dynamics area is still in the region of 40%.
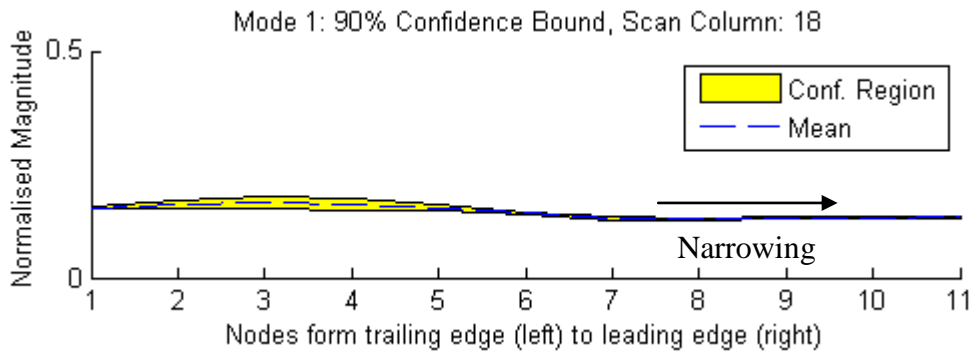
Figure 6-4: Line Mode 1 Confidence Region at Grid Column 18

Narrowing of the confidence region generally occurs near the trailing and leading edges for most modes because structural stiffness is added by resin beads and the foam spar at these locations. The mode shape variation is thus less dependent on skin stiffness modulus.

It was noted that location of nodal lines is less affected by material variance for lower order modes and that mode shape sensitivity to material changes is larger at higher frequencies with the COV of modes 4 and 5 around 60-70%.

6.1.2.3. Verifying FEM with Experimental Data

The FE model can be again verified by comparing the modal parameter variance (defined by FEM and Monte-Carlo, based on destructive material tests) with modal results from experimental tests on undamaged wings. Superposition of line modes (mode shape 2 for undamaged wings 1 and 3) on the confidence region is shown in figure 6-5.
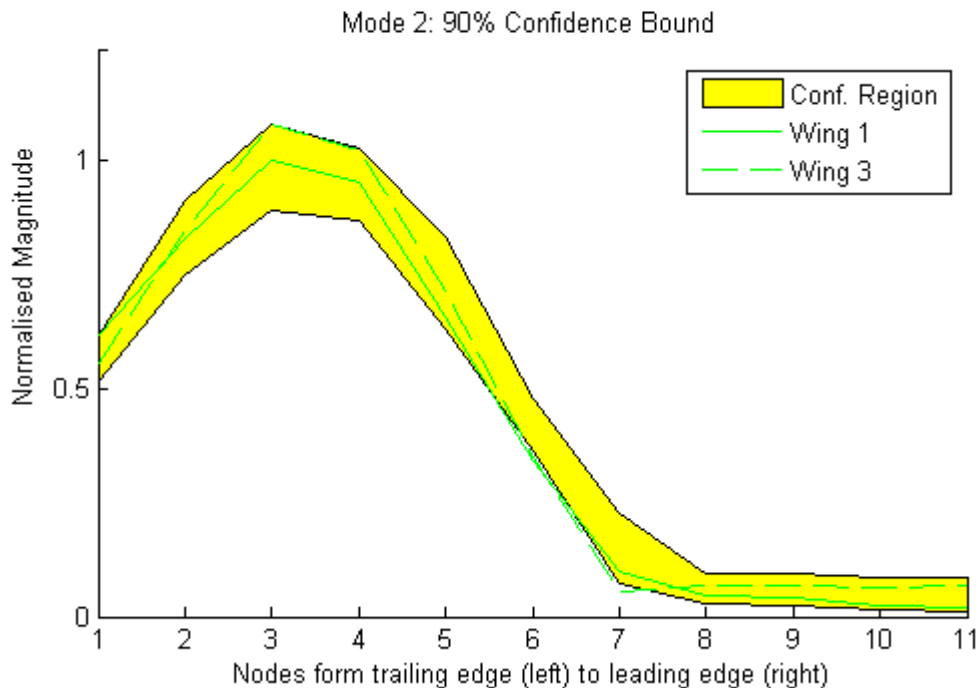
Figure 6-5: Line Mode 2 Comparison at Grid Column 18

The experimental modes fit comfortably inside the confidence region suggesting that the experimental variance has been captured by Monte Carlo simulation; especially in areas were sensitivity to skin properties is high.

Torsional mode shape variance is captured but variation resulting from design tolerances is not (figure 6-6).
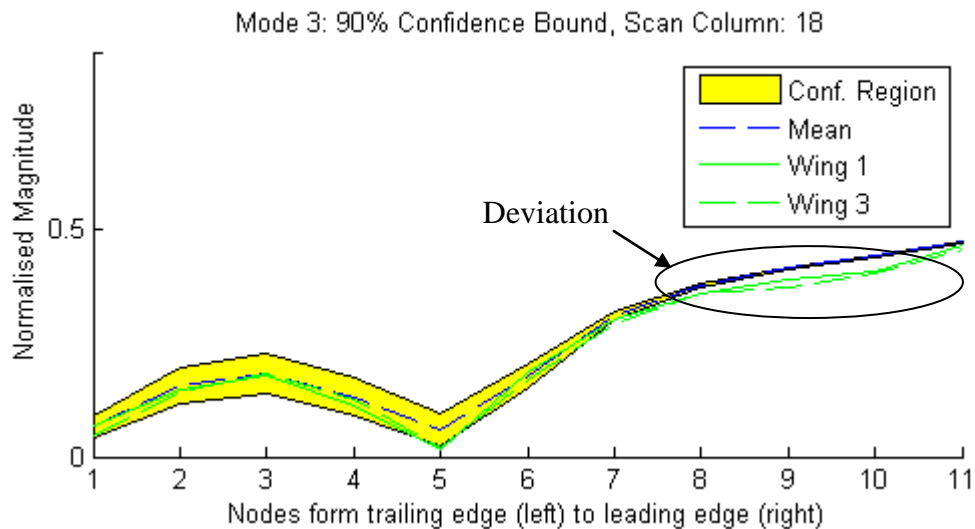
Note the deviation from the confidence region near the leading edge. Narrowing of the confidence region is severe at this location due to modal response being more sensitive to geometrical tolerance and less to skin variance, because of added stiffness form the spar. Repeatability problems with manufacturing the interface between the skins and the foam spar has resulted in an interface gap giving rise to varying damping effects in this location.

Also note that deviation from the confidence region is possible due to it being based on 90% confidence in sample variance and not 100%.

6.2. Damaged Case Study

Variability of material properties has been related to variable modal data and confidence bounds are in place for expected modes of undamaged UAV wing vibration. It is now possible to use this database of information to identify damage in the UAV wings.

6.2.1. Delaminated Wings

Suppose delamination is present in a wing manufactured using the same procedures and materials as those used to create this database. The question is whether the effect of delamination will be appreciable enough to influence the modal shapes to lie outside the undamaged confidence regions.

Recall wings 4, 5 and 6 being embedded with 50, 110 and 200 mm diameter delaminations (figure 3-9). By superimposing the modal line plots through a delamination area and comparing these to the expected confidence bounds, effects of delamination damage can be observed. Mode 2, which excites the area of delamination the most, is considered in figure 6-7.
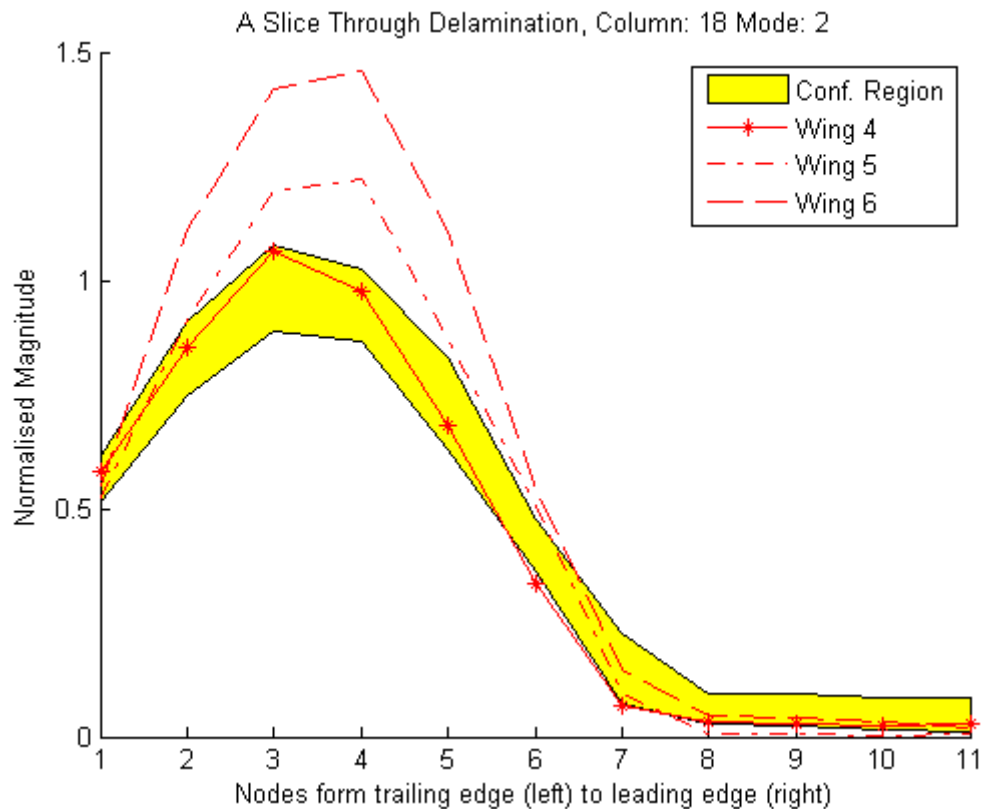
Figure 6-7: Line Mode 2 Superimposed Delamination

From the figure it is very clear that the delaminations of wings 5 and 6 have an appreciable effect on the magnitude of mode shape deflection, around the centre of the profile, and deviate from the confidence region by 20% and 43% respectively. Low deflection and lower sensitivity to skin stiffness keeps the responses in the confidence region near the leading edge.

Delaminations in wings 5 and 6 extend over the spar into the dynamic skin zone where as the delamination in wing 4 does not extend far into this zone. As a result the mode corresponding to wing 4 stays within the confidence region.

In the case of mode shape 1, the line mode is located near a nodal line, and correspondingly has low deflection magnitude (figure 6-8). Wing 5 and wing 6 show deviation at the centre of the aerofoil profile.

While this mode does detect delamination damage, it is not visually as impressive as mode 2. The deviation of wing 6 is around 46% at the centre of the profile and is 20% over the spar, still making it an effective mode for delamination detection.
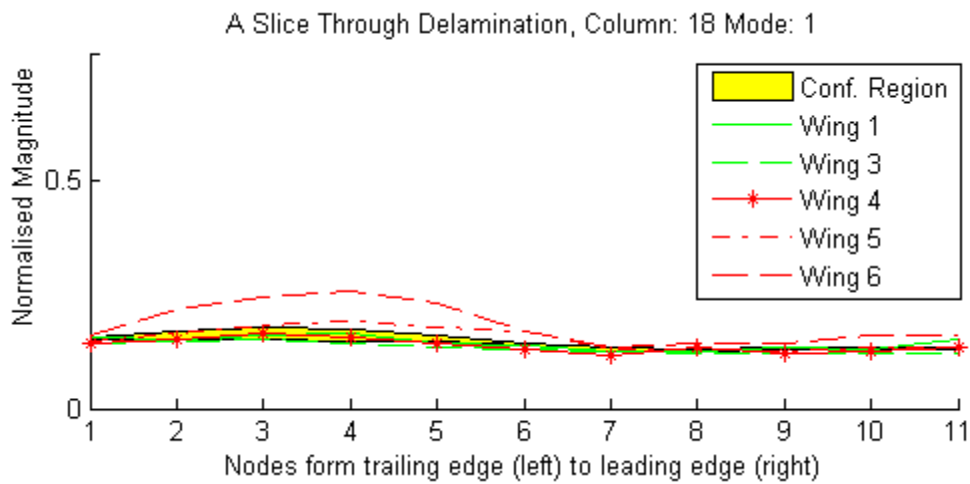
Figure 6-8: Line Mode 1 Superimposed Delamination

Another observation is that the effect of delaminations is localized. Superimposing line modes for all the wings, at a location away from delamination, shows adherence to the confidence zone (figure 6-9). The figure is a slice through grid column 7, which is the mirror image of grid column 18 about the centre of the wings length. Since mode 2 is symmetric about its length with a nodal line in the centre, comparison of the line modes from the delaminated and undamaged areas is easily accomplished. Undamaged and delaminated wings adhere to the confidence region along grid column 7.
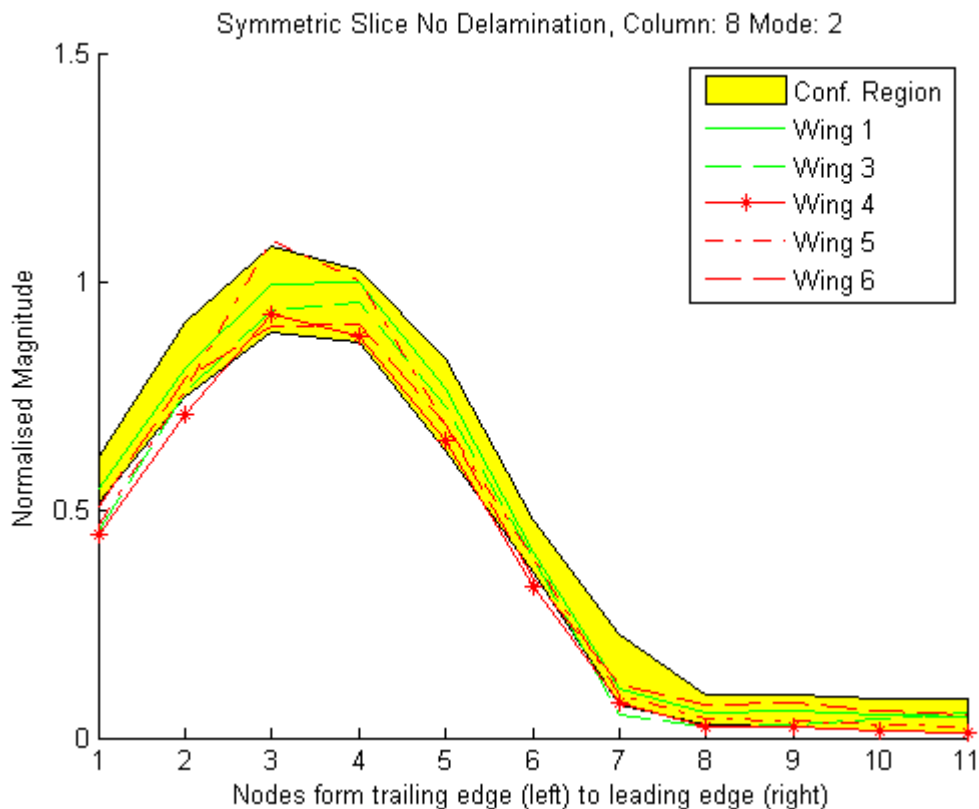
Figure 6-9: Line Mode 3 without Delamination

This location of delamination methodology can now be administered using the confidence region of the line modes over the wing geometry. Any deviation from the confidence region

is an alert to possible wing damage and can be pinpointed by referring to the specific line mode location in the wing geometry grid.

6.3. Chapter Summary

Monte-Carlo simulation has successfully produced confidence bounds for mode shape responses and correlates well with experimental results. Any undamaged wing manufactured using the same procedures and with the same materials, is expected to have modal response that lie within these bounds.

The variance of modal responses as a result of skin property variance is high especially in high magnitude deflection areas were added structural stiffness from other wing components is less.

The observations in the damaged wing case study showed that skin delamination is capable of perturbing the line mode shapes from the defined confidence regions. The localized effect of delaminations in combination with line mode confidence regions over wing grid geometry serves to locate damage.

Conclusion

A review of literature revealed that while the field of structural health monitoring has been researched for some time, it still lacks definitive work relating to real world application. Variability of new age composite materials poses complicated problems relating to SHM and analysis techniques. To fill the gap between research and application this dissertation presented and validated a methodology for damage detection in composite UAV wings through modal analysis, while considering probabilistic effects of stochastic material properties, for application to wings on a production line.

This research combines aspects of three main fields of research; effects of material variability on the vibration of structures, Multi-model updating, and SHM. In order to accomplish this, a reliable database of material properties was necessary to attempt a probabilistic approach.

Inspection of the manufactured wing structures revealed manufacturing uncertainties including spar placement tolerance, wing-spar interface gaps and variation in the quantity of resin beading applied. The uncertainties were measured and average values were used for modelling in order to consider such uncertainty deterministic. Effects of the interface gaps were later shown to be appreciable.

A distribution was created for each of the variable two dimensional orthotropic material properties E_1, E_2, G_{12}, ν_{12} and ρ of the UAV laminate skins. This distribution was normally distributed as is the generally the case with material property parameters, tolerances etc. The material properties were found to have a coefficient of variance of between 7 and 12%. Caution during testing achieved reasonable and repeatable tensile testing results but despite careful finishing of test coupons, edge singularities were found to be the main cause of failure.

The mean values of these properties and those attained for the wing's isotropic materials were used to model a numerical approximation of an undamaged wing case, using finite element analysis. The FEM consisted of laminate shell elements, representing the skins, in combination with solid elements to model isotropic spar and resin bead materials. Convergence test were performed on the wing model and a convergence rate, relating decrease in element size to difference in average natural frequency, of 0.6 was observed. Normal modes analysis was performed on the FE model to attain modal responses (natural frequency and mode shapes).

In order to verify the FE model, a multi-model updating procedure was performed to update selected sensitive material property parameters. Experimental modal parameters from an undamaged wing were used as response correlations. In total six UAV wings were vibration tested using a modal hammer and laser vibrometer setup. Free-free vibration conditions were used in order to eliminate uncertainties relating to boundary conditions and loading. Caution through had to be shown due to damping effects added by the suspension rubbers. An undamaged wing was twice cut to a smaller lengths and re-tested in order to provide enough response parameters for multi-model updating.

Modal analysis yielded six modes, for a full length UAV wing, with large variation of natural frequencies between wings. It was noted that there was no relation between delamination damage and natural frequency but that modal damping factors were indeed sensitive to delaminations, especially for higher order modes. The skins were found to have high levels of dynamics which tapered off nearer the leading and trailing ends of the aerofoil profile as a result of added stiffness from the spar and resin beadings.

Sensitivity analysis provided evidence for selection of skin laminate material properties as probabilistic and isotropic materials as deterministic. All material properties were updated in order to attain a FE model representative of an undamaged UAV wing since datasheet vales are often unreliable. This process also served as a non-destructive materials testing method. Converged values of the laminate properties were shown to fall within the confines of the normal distribution created by tensile testing.

Improvement of the FEA and EMA response correlation was found. The average natural frequency correlation was improved from 28.2% to 2% error. MAC improved by up to 19%.

Monte Carlo simulation, with the 2D orthotropic material property distribution used as variable parameters, yielded confidence bounds for the mode shapes of undamaged UAV wings. A geometry grid was established, using the wing data acquisition points, to define line modes. Variation of laminate skin properties were found to have significant effects on the coefficient of variance of mode shapes, attaining average values of up to 40%.

Application of the probabilistic database for damage detection was presented in terms of case studies. Superposition of damaged and undamaged wing modes, over the constructed confidence regions, showed that delamination effects were capable of perturbing the mode shape responses from the confidence regions. It was noted that this was most effective in areas of high skin dynamics were the structural stiffness was more skin dependant. It was also noted that the effects of delamination on modal shape response was localised.

Through definition of a modal parameter confidence region in combination with a geometry grid and considering that delamination effects are local, detection and location of delaminations is achieved whilst still considering material uncertainties.

Future Work and Recommendations

The development of this SHM methodology may be improved upon in the future by further considerations of uncertainty. A less simplified wing structure should be used which includes sandwich panel skins and wing ribs. More applicable boundary conditions should be considered to comply with real world application. Although the research was performed using velocity based modal analysis, the theoretical background is similar (although less complex) to strain modal techniques which better suit practical application and link with research in strain measurement like that of fibre Bragg gratings.

References

Abbey, T. (2009).*Composite e-learning course, eL005*. NAFEMS, December 2009.

Allegri, G., Corradi, M. & Marchetti.(2006). Stochastic analysis of the vibrations of an uncertain composite truss for space applications. *Composite Science and Technology*, 66:273-282.

Alnefaie, K. (2009). Finite element modelling of composite plates with internal delamination. *Composite Structures*, 90:21-27.

ASTM D3039.(2002). *Standard test method for tensile properties of polymer matrix composite materials*. United States: ASTM International.

ASTM D3518.(2001). *Standard test method for in-plane shear response of polymer matrix composite materials by tensile test of ±45° laminate*. United States: ASTM International.

Axson Technologies. (2008). *Epolam 2022:Technical data sheet*. Available from: http://www.axson-na.com/TDSs/TDS%20-%20Epolam%202022%20System%20-%20US%20REV%2000.pdf
(Accessed October 2010).

Bathe, K.J. (1996). *Finite element procedures*. Prentice-Hall: Englewood.

Campbell, K. *SA continues to spread its UAV wings*. Engineering News (Magazine), January-February 2009.

Carbonfiberdiy.(2010). *Carbon fiber fiberglass DIY how to guides*. Available from: http://www.carbonfiberdiy.com. (Accessed June 2011).

Chandrashekhar, M & Ganguli, R. (2009).Uncertainty in structural damage detection using fuzzy logic and probabilistic simulation. *Mechanical Systems and Signal Processing*, 23:384-404.

Chapelle, D. &Bathe, K.J. (2000).The mathematical model underlying general shell elements. *International Journal for Numerical Methods in Engineering*, 48:289-313.

Chattopadhyay, A., Changho, N. & Dragomir-Daescu, D. (1999).Delamination modeling and detection in smart composite plates. *Journal of Reinforced Plastics and Composites*, 18(17):1557-1572.

Chen, C., Duhamel, D. & Soize, C. (2006). Probabilistic approach for model and data uncertainties and its experimental identification in structural dynamics: Case of composite sandwich panels. *Journal of Sound and Vibration*, 294:64-81.

Composites Institute. (1998). *Introduction to composites, 4th edition*. New York: Society of the Plastics Industry.

Cook, R.D., Malkus, D.S., Plesha, M.E. & Witt, R.J. (2002). *Concepts and applications of finite element analysis*. United States: John Wiley & Sons. Inc.

Cunha, J. & Piranda, J. (1999).Application of model updating techniques in dynamics for the identification of elastic constants of composite materials. *Composites: part B: engineering*, 30:79-85.

Cusano, A., Capoluong, P., Campopiano S., Cutolo, A., Giordano, M., Ferdinando, F., Paolozzi, A. & Caponero, M. (2006).Experimental modal analysis of an aircraft modelwing by embedded fibre Bragg grating sensors. *IEEE Sensors Journal*, 6(1):67-77.

De Gersem, H., Moens, D., Desmet, W. & Vandepitte, D. (2005). A fuzzy finite element procedure for the calculation of uncertain frequency response functions of damped structures: Part 2 – Numerical case studies. *Journal of Sound and Vibration*, 288:463-486.

Della, N.D. (2007). Vibration of Delaminated Composite Laminates: A review. *Applied Mechanics Reviews*, ASME, January 2007.

Deperrios, A. (2009). XFLR5 v.4.1.7 (Computer software). Available from: http://xflr5.sourceforge.net/xflr5.htm.

Diamanti, K. & Soutis, C. (2010).Structural health monitoring techniques for aircraft composite structures. *Progress in Aerospace Sciences*, 46:342-352.

Doebling, S. W., Farrar, C. R., Prime, M. B. & Shevitz, D. W. (1995). *Damage identification and health monitoring of structural and mechanical systems from changes in their vibration characteristics: a literature review*. Report LA-13070-MS, Los Alamos, NM.

Epo. (2006). *Low temperature pre-preg FT109: Preliminary data sheet*. Received from: Chris Adrian, Lightweight Structures Technology.(25 October 2010).

Euler, E. Sol, H.& Dascotte, E. (2006). *Identification of material properties of composite beams: inverse method approach*, Proceedings of the SEM Annual Conference & Exposition on Experimental and Applied Mechanics, USA: St. Louis, MO.

FEMtools 3.4.1.(2010).*Model updating theoretical manual*. Dynamic Design Solutions.

Gentile, C. & Saisi, A. (2007).Ambient vibration testing of historic masonry towers for structural identification and damage assessment. *Journal of Construction and Building Materials*, 21:1311-1321.

GOM mbH. (2009). *Aramis user manual: Software*. Copy right 2007: GOM mbH.

Grouve, W.J.B., Warnet, L., de Boer, A., Akkerman, R. & Vlekken, J. (2008). Delamination detection with fibre Bragg gratings based on dynamic behaviour. *Composite Structures and Technology*, 68:2418-2424.

Hexcel. (2007a). *Mechanical Testing of Sandwich Panels: Technical Notes*. Available from: http://www.hexcel.com/Resources/DataSheets/Panel-Data-Sheets/SandwichPanels_global.pdf(Accessed January 2010).

Hexcel. (2007b). *HexWeb A1 and A10: High strength aramid honeycomb product data*. Available from: http://www.hexcel.com/Resources/DataSheets/Honeycomb-Data-Sheets/A1A10_eu.pdf(Accessed January 2010).

Hexcel. (2010). *Fibrelam Honeycomb Sandwich Panels for Aerospace*. Available from: http://www.hexcel.com/Products/Aerospace/AAircraft-Flooring. (Accessed January 2010).

Irvine, T. (2004).*Damping properties of materials revision C*. Available from: http://www.cs.wright.edu/~jslater/SDTCOutreachWebsite/damping%20properties%20of%20materials.pdf.(Accessed May 2011).

Kashtalyan, M. & Soutis, C. (2007). Stiffness and fracture analysis of laminated composites with off-axis ply matrix cracking. *Composites A*,38(4):1262-1269.

Kellas, S., Morton, J. & Jackson, K. E. (1993). *Damage and Failure Mechanisms in scaled angled-ply laminates*. Conference proceedings of the fourth Composites Symposium on Fatigue and Fracture, ASTM STP 1156.Held by the American Society for Testing and Materials, 257–280.

Kessler, S.S., Spearing, S.M., Atalla, M.J., Cesnik, C.E.S. & Soutis, C. (2002).*Structural health monitoring in composite materials using frequency response methods*. Unpublished thesis. Department of Aeronautics and Astronautics: Massachusetts Institute of Technology, Cambridge.

Keye, S. (2006). Improving the performance of model-based damage detection methods through the use of an updated analytical model. *Aerospace Science and Technology*, 10:199-206.

Kharrazi, M.H.K., Carlos, E.V., Brincker, R. & Dascotte, E. (2001).*A study on damage detection using output-only modal data*. Conference proceedings of the 19th IMAC conference held in Hyatt Orlando.

Kollar, L.P. &. Springer, G.S. (2003). *Mechanics of composite structures*. Cambridge University Press.

Kritz, R. (2000). *Introduction to mechanical behaviour of laminates (laminate plate theory): analytic model*. Available from: http://www.jwave.vt.edu/crcd/kriz/lectures/ Laminates.html (Accessed January 2010).

Lauwagie, T., Sol, H. & Dascotte, E. (2002a). *Damage Identification in Beams using Inverse Methods*. Proceedings of the International Seminar on Modal Analysis (ISMA), 715-722.

Lauwagie, T., Sol, H., Roebben, G., Heylen, W. & Shi, Y. (2002b). *Validation of the Resonalyser method: An inverse method for material identification*. Proceedings of the International Seminar on Modal Analysis (ISMA), 687-694.

Lauwagie, T. & Dascotte, E. (2002c).*Layered Material Identification using Multi-Model updating*. Proceedings of the 3rd International Conference on Structural Dynamics Modeling - Test, Analysis, Correlation and Validation, Portugal: Madeira Island.

Lloyd Instruments LTD, 1999. *Lloyd EZ50 user manual version 2.0*. Available from: http://wdturner.com/ez_series_OM.pdf. (Accessed May 2010).

Lopez, I. & Sarugul-Klijn, N. (2010). A review of uncertainty in flight vehicle structural damage monitoring, diagnosis and control: Challenges and opportunities. *Progress in Aerospace Sciences,* 46:247-273.

Maeck, J., Wahab, M.A. & Peeters, B. (2000). Damage identification in reinforced concrete structures by dynamic stiffness determination. *Engineering Structures*, 22:1339:1349.

Manan, A. & Cooper, J.E. (2010). Prediction of uncertain frequency response function bounds using polynomial chaos expansion. *Journal of Sound and Vibration*, 329:3348-3358.

Montgomery, D. C. & Runger, G.C. 2007. *Applied statistics and probability for engineers*. USA: Wiley.

MSC.(2007). *NAS 113, MD Nastran composite materials*. MSC Software Corporation: Copyright 2007.

MSC.(2008). *NAS 113, Patran Release Guide 2008 r1*. MSC Software Corporation: Copyright 2008

Oliver, J.A., Kosmatka, J.B., Hemez, F.M. & Farrar, C.R. (2006). *Validating finite element models of composite aerospace structures for damage detection applicatio*ns. Proceeding of SPIE – the international society for optical engineering, 6176:71-90.

Pan.S., Wu, L. & Sun Y. (2008).Transverse shear modulus and strength of honeycomb cores. *Composite Structures*, 84:369-374.

Pandey, A.K., Biswas, M. & Samman, M.M. (1990). Damage detection from changes in curvature mode shapes. *Journal of Sound and Vibration*, 145(2):321-332.

Polytec. (2008). *PSV-400 Scanning laser vibrometer: hardware manual*. Germany: Polytec GmbH.

Rao, S.S. (2005). *Mechanical vibrations* fourth edition. Upper Saddle River: Prentice Hall.

Robert M. J. (1998). *Mechanics of composite materials, second edition.* Taylor & Francis: BS Publication.

Roha-cell.(2010). *Rohacell 70 polymethacrylimide (PMI) rigid foam sheet*. Received from: Chris Adrian, Lightweight Structure Technology. (20 August 2010).

Rosato, D. V. (1997). *Designing with reinforced plastics*. Ohio Cincinnati: Hanser/Gardner.

Salawu, O. S. (1997). Detection of structural damage through changes in frequency: a review. *Engineering structures*, 19:718-723.

Saravanos, D.A. & Hopkins, D.A. (1996). Effects of delaminations on the damped dynamic characteristics of composite laminates: Analysis and experiments. *Journal of Sound and Vibration*, 192(5):977-993.

Shook, Gerald, (1986). *Reinforced plastics for commercial composites source book*, ASM, Metals Park, OH.

Singh, B.N., Bisht, A.K.S., Pandir, M.K. & Shukla, K.K. (2009).Nonlinear free vibration analysis of composite plates with material uncertainties: A Monte Carlo simulation approach. *Journal of Sound and Vibration*, 324:126-138.

Spangenberg, U. (2009). *The development of a robust output-only strain based damage detection technique for wing-like structures, requiring a minimum number of sensors. masters dissertation*. Pretoria: University of Pretoria.

Teh, K.K. & Huang, C.C. (1980). The effects of fibre orientation on free vibration of composite beams. *Journal of Sound and Vibration*, 69(2):327-337.

Teughels, A., Maeck, J. & De Roeck, G. (2002). Damage assessment by FE model updating using damage functions. *Composite Structures*, 80:1869-1879.

Teughels, A., Maeck, J. & De Roeck, G. (2004). Structural damage identification of the highway bridge Z24 by FE model updating. *Journal of Sound and Vibration*, 287:589-610.

Trendafilova, I., Cartmell, M.P. & Ostachowicz, W. (2008). Vibration-based damage detection in an aircraft wing scaled model using principal component analysis and pattern recognition. *Journal of Sound and Vibration*, 313:560-566.

Van Vinckenroy, G. & de Wilde, W.P. (1995). The use of Monte Carlo techniques in statistical finite element methods for the determination of the determination of the structural behaviour of composite materials structural components. *Composite Structures*, 32:247-253.

Vanlanduit, S., Parloo, E. & Guillaume, P. (2002). Combined damage detection techniques.*Journal of Sound and Vibration*, 266:815-831.

Vári, L.M. & Heyns, P.S. (1997). Strain modal testing – a critical appraisal. *R & D Journal*, 13(3):83-90

Wahab, A.M.M. & Roeck, G.D. (1999a). Damage detection in bridges using modal curvatures: Application to a real damage scenario. *Journal of Sound and Vibration*, 226(2):217-235.

Wahab, A.M.M., Roeck, G.D. & Peeters, B. (1999b). Parameterization of damage in reinforced concrete structures using model updating. *Journal of Sound and Vibration*, 228(4):717-730.

Yam, L.H., Leung, T.P., Li, D.B. & Xue, K.Z. (1996). Theoretical and experimental study of modal strain analysis. *Journal of Sound and Vibration*, 191(2):251-260.

Yang, Z., Wang, L., Wang, H., Ding, Y. & Dang, X. Damage detection in composite structures using vibration response under stochastic excitation. *Journal of Sound and Vibration*, 325:755-768.

Zou, Y., Tong, L. & Steven, G.P. (2000).Vibration-based model-dependent damage(delamination) identification and health monitoring for composite structures - a review. *Journal of Sound and Vibration*, 230(2):357-378.

Appendix A: Probability

A.1 SDOF Verification of Equation 2.20

A Monte Carlo simulation with 200 iterations was performed on the system described below in order to validate the analytical solution (equation 2.20), developed to find the variance of the natural frequency of a SDOF system and to consider frequency distribution.

Example 2.4 from Rao (2005:123) was used as a basis for the SDOF system. The example considers a mass of 2000N and stiffness of 10^7N/m. For this dissertation, standard deviations of 100N and 10^6 N/m for mass and stiffness respectively were used in equation 2.20 and to generate 200 normally distributed values for MC.

Table A-1 presents the values attained by both methods. The standard deviation result from eq. 2.20 differs from a 200 iteration MC result by less than 1%. This certainly indicates that eq. 2.20 is a valid analytical solution for the standard deviation of the natural frequency of a SDOF system.

Table A-1: SDOF Analytical Solution (eq. 2.28) Validation

Defined Parameters			Deterministic	Eq. 2.29	Monte Carlo	% Diff.
Statistic	M [N]	K [N/m]	ω_n (Hz)	ω_n (Hz)	ω_n (Hz)	[%]
Mean μ	2000	10^7	35.25	35.25	35.34	0.27%
Std σ	100	10^6	N/A	1.97	1.98	0.72%
COV	5%	10%	N/A	5.59%	5.62%	0.45%

The figure below presents the scatter of the natural frequency as determined by MC. It was found that the normally distributed nature of the variable input parameters has filtered through to the natural frequency as indicated by the histogram and Normal probability plots.
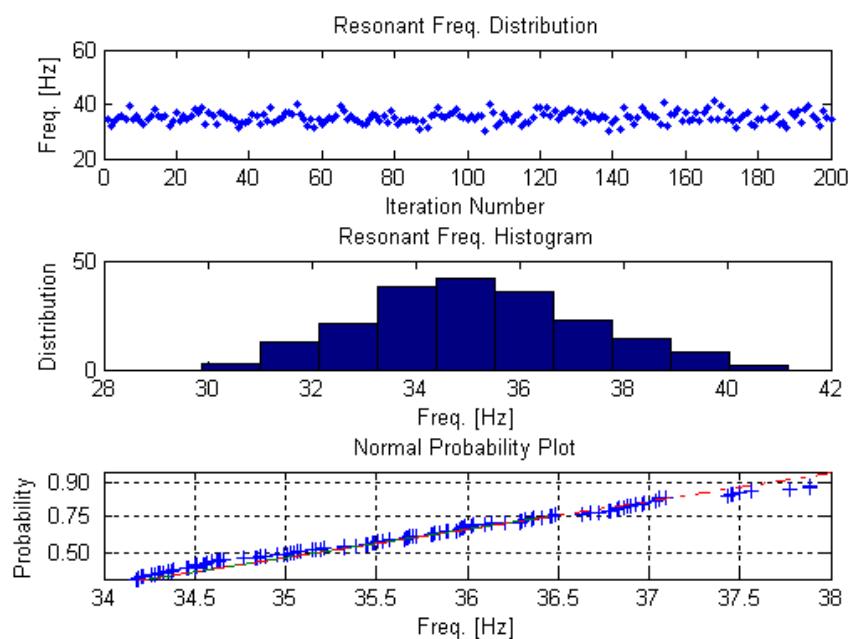
FigureA-1: SDOF Frequency Normally Distributed

A.2 MDOF Monte Carlo Simulation

Calculation of the necessary derivatives for tailor series approximation becomes exponentially resource hungry with an increase invariable input parameters. For this reason the analytical solution is inefficient for models larger than 1DOF. Monte Carlo however still remains a viable way to determine the statistical parameters (standard deviation, COV).

The exercise here however is to verify whether the normal distribution nature of the input variable will filter through the eigen-value solution to result in normally distributed modal parameters (natural frequency) in a MDOF scenario. The analytical solution here is no longer in the neat form of equation 2.20 but rather a lengthy loop of differentiation and substitution.

The model considered here was adapted from Rao (2005:515), example 6.23. A 3DOF system with masses m_1=100, m_2=10 and m_3=10 kg and stiffness k_1=4,k_2=4, k_3=4 and k_4=1 kN/m result in global matrices:

$$K = \begin{bmatrix} k_1 + k_2 & -k_2 & -k_3 \\ -k_2 & k_2 + k_3 & 0 \\ 0 & -k_3 & k_3 + k_4 \end{bmatrix} \text{ and } M = \begin{bmatrix} m_1 & 0 & 0 \\ 0 & m_2 & 0 \\ 0 & 0 & m_3 \end{bmatrix} \quad (A.1)$$

Solving the system results in three resonant frequencies:1.02, 2.52 and 5.25 Hz. Only stiffness was considered variable in order to limit calculation time. The average time to analytically solve for the standard deviation of the resulting three natural frequencies with variance only specified on stiffness is approximately 4min 45 sec. The addition of more stochastic variables, i.e. varying mass, results in a solution time of 10 hours. Table A-2 gives the problem standard deviation result with a COV on the stiffness of 5%.

Table A-2: 3DOF Analytical Solution

3DOF: Std. Deviation of Natural Frequency [Hz]			
$\sigma_{\omega n}$	Analytical	Monte Carlo	% Diff.
$\sigma_{\omega 1}$	0.0215	0.0214	0.47%
$\sigma_{\omega 2}$	0.0373	0.0366	1.91%
$\sigma_{\omega 3}$	0.0982	0.0977	0.51%

While the solution of the analytical method is clearly still valid, the resource required for calculation is not desirable. Monte Carlo however still presents good results in reasonable time. Another advantage is that the distribution of the resonant frequencies can be observed. A histogram and probability plot of the third frequency (figure A-2) clearly shows that the normally distributed nature of the stochastic stiffness input variables has filtered through the eigen-value problem to the resonant frequencies.

Considering now that the same result has been achieved for both SDOF and MDOF systems, it leads to a conclusion that the possibility of normally distributed modal parameters may be the character of more complicated structures. This is by no means guaranteed for all cases but

certainly gives confidence that equation 2.21could be of use in creating confidence bounds on modal parameters.
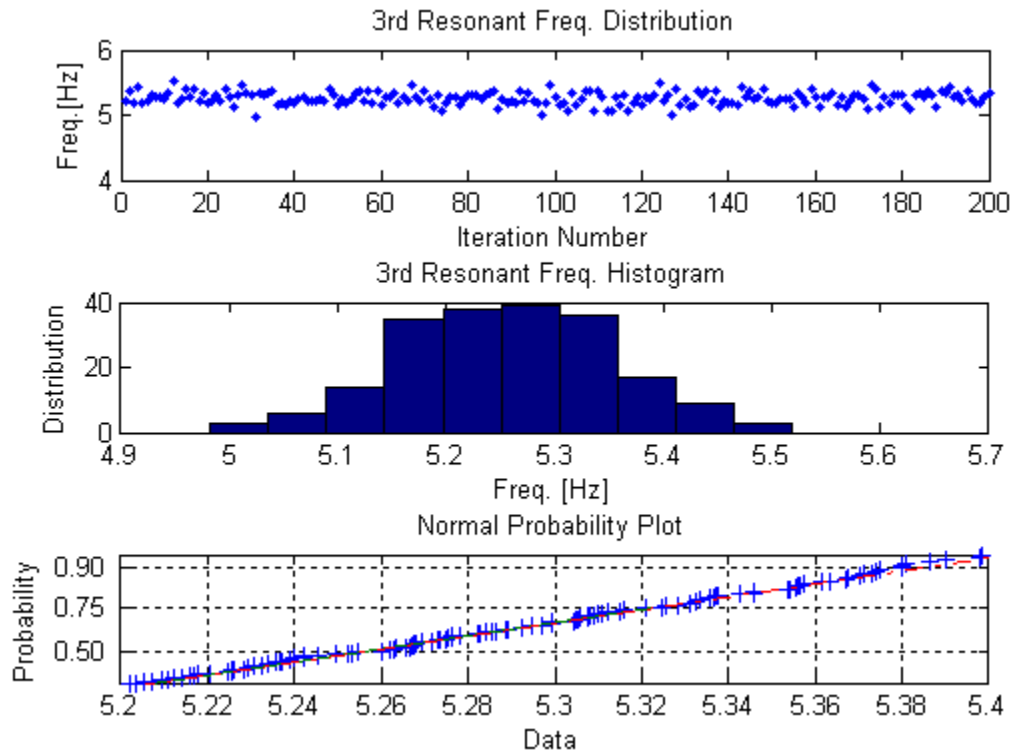
FigureA-2: MDOF Frequency Normally Distributed

A.3 SDOF Matlab Code

```
% SDOF Analytical Verification of equation 2.20
% Timothy Prinsloo
% University of Pretoria
% 2010


n = 200;      %Number of Monte Carlo Iterations

%--------------------------------------------------
%Define Stiffness K: Mean = 110 and STD = 5 [N/m]
%--------------------------------------------------

Mean_k = 1e7;                % Stiffness Mean
std_k = Mean_k*0.1;          % Stiffness Standard Deviation
COV_k = std_k/Mean_k*100;    % Stiffness Coefficient of Variance


%------------------------------------------
%Define Mass M: Mean = 2000 and STD = 100 [N]
%------------------------------------------

Mean_m = 2000/9.81;          % Mass Mean [kg]
std_m = Mean_m*0.05;         % Mass Standard Deviation [kg]
COV_m = std_m/Mean_m*100;    % Mass Coefficient of Variance [%]

det_mean=sqrt(Mean_k/Mean_m)/(2*pi) %Deterministic Mean [Hz] eq. 2.1
```

```
%----------------------------------
% Equation 2.20 Analytical Solution
%----------------------------------

Mean_wn = sqrt(Mean_k/Mean_m);        % w_n Mean [rad/s] eq. 2.1

% Equation 2.20 Standard Deviation of Natural Frequency [Hz]
% The equation here is divided by 2*pi for conversion to Hz
std_wn=1/(2*Mean_wn*(Mean_m)^2)*sqrt((Mean_k)^2*(std_m)^2+(Mean_m)^2*(std_k
)^2)/(2*pi);

COV_wn = std_wn/det_mean*100;         % COV [%] of eq. 2.28

%---------------------
%Monte Carlo Simulation
%---------------------

uk = Mean_k+std_k.*randn(n,1);        % 200 Normally Distributed Stiffness
um = Mean_m+std_m.*randn(n,1);        % 200 Normally Distributed Mass
un = sqrt(uk./um);                    % MCS 200 Values of w_n eq. 2.1

Mean_wn_iter = mean(un)/(2*pi);       %MCS Mean [Hz]
std_wn_iter = std(un)/(2*pi);         %MCS Standard Deviation
COV_wn_iter = std_wn_iter/Mean_wn_iter*100; %MCS COV [%]
```

A.4 MDOF Matlab Code

```
% 3DOF Distribution of Modal Parameters
% Timothy Prinsloo
% University of Pretoria
% 2010

%--------------
% Deterministic
%--------------
k = [8 -4 0;-4 8 -4;0 -4 5].*1000;  % Stiffness Matrix
m = [100 0 0;0 10 0;0 0 10];        % Mass Matrix
[v,d]=eig(k,m);                     % Eigen Solution
f(1,:) = sqrt(diag(d))./(2*pi)      % Deterministic Freq. [Hz]

%--------------------------
% Probabilistic Monte Carlo
%--------------------------
n = 200;                            % n=200 MC Iterations

% Normally Distributed Stiffness
k1 = 4000+200.*randn(n,1);k2 = 4000+200.*randn(n,1);k3 =
4000+200.*randn(n,1);k4 = 1000+50.*randn(n,1);

% Mean Stiffness Matrix
mean_k(1,1) = mean(k1);mean_k(1,2) = mean(k2);mean_k(1,3) =
mean(k3);mean_k(1,4) = mean(k4);

% Variance on Stiffness
std_k(:,1) = std(k1);std_k(:,2) = std(k2);std_k(:,3) = std(k3);std_k(:,4) =
std(k4);

% Stiffness COV
cov_k(:,1) = std(k1)./mean(k1)*100; cov_k(:,2) =
std(k2)./mean(k2)*100;cov_k(:,3) = std(k3)./mean(k3)*100;cov_k(:,4) =
std(k4)./mean(k4)*100;
```

```
% Eigen Problem and Matrix Assembly
for i = 1:n
%mass
    M = zeros(3,3);M(1,1) = 100;M(2,2) = 10;M(3,3) = 10;

%stiffness
    K = zeros(3,3);K(1,1) = k1(i)+k2(i);K(1,2) = -k2(i);K(1,3) = 0;
K(2,1) = -k2(i);K(2,2) = k2(i)+k3(i);K(2,3) = -k3(i);K(3,1) = 0;
K(3,2) = -k3(i);K(3,3) = k3(i)+k4(i);

%solution
    [V,D] = eig(K,M);
F(:,i) = sqrt(diag(D))./(2*pi); % 200 MC Frequency Values [Hz]
end


%-----------
% Analytical
%-----------
syms k1k2k3k4w%System Variables

%Assemble Matrix
K = [k1+k2 -k2 0; -k2 k2+k3 -k3;0 -k3 k3+k4]
m1 = 100;
m2 = 10;
m3 = 10;
M = [m1 0 0; 0 m2 0; 0 0 m3]

W = det(K - w^2.*M);    % Eigen Solution
sol = solve(W,'w');

% Probabilistic Loop
ct = 0;
for i = 1:2:6
      ct = ct+1
      clear a1a2a3a4a5a6a7

      % Partial Differentiation of Stiffness Variables
      a4 = abs(diff(sol(i),k1));
      a5 = abs(diff(sol(i),k2));
      a6 = abs(diff(sol(i),k3));
      a7 = abs(diff(sol(i),k4));

      % Mean Values
      m1 = 100;m2 = 10;m3 = 10;
      k1 = 4000;k2 = 4000;k3 = 4000;k4 = 1000;

      % Substitution of Mean values into variables
      a(4) = subs(a4);
      a(5) = subs(a5);
      a(6) = subs(a6);
      a(7) = subs(a7);

      % Taylor Series Expansion, Solution for Std. Dev. of Freq. [Hz]
      sigw(ct) = sqrt(a(4)^2*std_k(1)^2 + a(5)^2*std_k(2)^2 +
      a(6)^2*std_k(3)^2 + a(7)^2*std_k(4)^2)./(2*pi);
end
```

A.5 t Distribution

Below is the table required by equation 2.21 to determine the upper and lower percentage point of the *t* distribution with *n*-1 degrees of freedom. For 90% confidence bounds on sample mean $t_{\alpha/2,n-1} = 1.645$.

Table A-3: t Distribution Table, (Montgomery, et al. 2007)

ν \ α	.40	.25	.10	.05	.025	.01	.005	.0025	.001	.0005
1	.325	1.000	3.078	6.314	12.706	31.821	63.657	127.32	318.31	636.62
2	.289	.816	1.886	2.920	4.303	6.965	9.925	14.089	23.326	31.598
3	.277	.765	1.638	2.353	3.182	4.541	5.841	7.453	10.213	12.924
4	.271	.741	1.533	2.132	2.776	3.747	4.604	5.598	7.173	8.610
5	.267	.727	1.476	2.015	2.571	3.365	4.032	4.773	5.893	6.869
6	.265	.718	1.440	1.943	2.447	3.143	3.707	4.317	5.208	5.959
7	.263	.711	1.415	1.895	2.365	2.998	3.499	4.029	4.785	5.408
8	.262	.706	1.397	1.860	2.306	2.896	3.355	3.833	4.501	5.041
9	.261	.703	1.383	1.833	2.262	2.821	3.250	3.690	4.297	4.781
10	.260	.700	1.372	1.812	2.228	2.764	3.169	3.581	4.144	4.587
11	.260	.697	1.363	1.796	2.201	2.718	3.106	3.497	4.025	4.437
12	.259	.695	1.356	1.782	2.179	2.681	3.055	3.428	3.930	4.318
13	.259	.694	1.350	1.771	2.160	2.650	3.012	3.372	3.852	4.221
14	.258	.692	1.345	1.761	2.145	2.624	2.977	3.326	3.787	4.140
15	.258	.691	1.341	1.753	2.131	2.602	2.947	3.286	3.733	4.073
16	.258	.690	1.337	1.746	2.120	2.583	2.921	3.252	3.686	4.015
17	.257	.689	1.333	1.740	2.110	2.567	2.898	3.222	3.646	3.965
18	.257	.688	1.330	1.734	2.101	2.552	2.878	3.197	3.610	3.922
19	.257	.688	1.328	1.729	2.093	2.539	2.861	3.174	3.579	3.883
20	.257	.687	1.325	1.725	2.086	2.528	2.845	3.153	3.552	3.850
21	.257	.686	1.323	1.721	2.080	2.518	2.831	3.135	3.527	3.819
22	.256	.686	1.321	1.717	2.074	2.508	2.819	3.119	3.505	3.792
23	.256	.685	1.319	1.714	2.069	2.500	2.807	3.104	3.485	3.767
24	.256	.685	1.318	1.711	2.064	2.492	2.797	3.091	3.467	3.745
25	.256	.684	1.316	1.708	2.060	2.485	2.787	3.078	3.450	3.725
26	.256	.684	1.315	1.706	2.056	2.479	2.779	3.067	3.435	3.707
27	.256	.684	1.314	1.703	2.052	2.473	2.771	3.057	3.421	3.690
28	.256	.683	1.313	1.701	2.048	2.467	2.763	3.047	3.408	3.674
29	.256	.683	1.311	1.699	2.045	2.462	2.756	3.038	3.396	3.659
30	.256	.683	1.310	1.697	2.042	2.457	2.750	3.030	3.385	3.646
40	.255	.681	1.303	1.684	2.021	2.423	2.704	2.971	3.307	3.551
60	.254	.679	1.296	1.671	2.000	2.390	2.660	2.915	3.232	3.460
120	.254	.677	1.289	1.658	1.980	2.358	2.617	2.860	3.160	3.373
∞	.253	.674	1.282	1.645	1.960	2.326	2.576	2.807	3.090	3.291

ν = degrees of freedom.

Appendix B: Model Updating Correlation Coefficients

Different levels of correlation analysis exist. They range from visual comparison of the mode shapes, global and local correlation and the calculation of correlation coefficients that are calculated from the weighted relative differences between different modal parameters. Appended here are further correlation coefficients (CC) available in FEMtools for correlation between FEA and EMA output parameters.

- FRF Correlation

Frequency response functions can be correlated locally and globally in FEMtools using Cross Signature Correlation (CSC) functions. The global correlations are Cross Signature Assurance Criterion (CSAC) and Cross Signature Scale Factor (CSF) criterion. It must be noted though that these methods can become extremely time consuming owing to large quantities of data. The benefit however is that it provides enough test response data in relation to numerical responses.

At each frequency point ω_k the level of correlation between the measured FRFs (α_X) and predicted FRFs (α_A) can be evaluated as:

$$CSCA(\omega_k) = \frac{\left| \alpha_{Xi}^H(\omega_k)\alpha_{Ai}(\omega_k) \right|^2}{\left(\alpha_{Xi}^H(\omega_k)\alpha_{Xi}(\omega_k) \right)\left(\alpha_{Ai}^H(\omega_k)\alpha_{Ai}(\omega_k) \right)}, \; k=1,2...\,\mathrm{Nf} \qquad \text{(B-1)}$$

where Nf is the number of frequency points. This criterion expresses the shape correlation between measured and predicted response Values range between 0 and 1. Because CSAC evaluates the shape of an FRF, which is mainly determined by the position and amount of resonance peaks, this function is most sensitive to changes of mass and stiffness modeling.

Because an FRF is not only defined by its shape, it is necessary to introduce a second correlation function that evaluates the discrepancies in amplitude namely CSF, and is defined as:

$$CSF(\omega_k) = \frac{2\left| \alpha_{Xi}^H(\omega_k)\alpha_{Ai}(\omega_k) \right|}{\left(\alpha_{Xi}^H(\omega_k)\alpha_{Xi}(\omega_k) \right)\left(\alpha_{Ai}^H(\omega_k)\alpha_{Ai}(\omega_k) \right)}, \; k=1,2...\,\mathrm{Nf} \qquad \text{(B-2)}$$

Like CSAC, the values of CSF can range between 0 and 1. CSF evaluates amplitude, and is thus more sensitive to damping.

Appendix C: UAV Wing Manufacture Sheet (PPS)

The process of manufacturing structural components is governed by a part process sheet (PPS) as in table C-1 below. Here the manufacturing steps and instructions are communicated to the workmen on the factory floor.

Table C-1: PPS, Lightweight Structures Technology

WORKSHOP PART PROCESS SHEET		
FT109 pre-preg wing skin		
DOCUMENT NO: LST-PPS-1054 – 005	SHT 1 OF 1	
PART No	SERIAL NO: SN 01	DRG NO: N/A

No	PROCESS PROCEDURE	MATERIAL
1.	Prepare mould with Frekote	
2.	Cut material, (1220 long)	Cut material accurately and layup accurately!!
3.	BI 45	280 gsm FT109
4.	BI 0/90	280 gsm FT109
5.		
6.	BI 0/90	280 gsm FT109
7.	BI 45	280 gsm FT109
8.	peel ply	
9.	Cure in autoclave @ 120 deg for 2hrs min	3 bar max
10.	Demould and trim	

Appendix D: Tensile Test Addition Results Tables

D.1 Additional Fibrelam Tensile Test Results

Results from the Fibrelam tensile tests are given in the tables below. The statistical mean, standard deviation and coefficient of variance are given for each material property relating for both panels 2 and 4.

Table D-1: Fibrelam Modulus of Elasticity (E_2)

Coupon #	Panel 1 [GPa]		Panel 4 [GPa]	
1	16.31	SWT	17.82	LGM
2	17.26	SWT	17.29	LWB
3	17.19	LWT	15.98	LGM
4	16.71	LWT	18.84	LGM
5	16.48	SWB	17.81	AWT
Mean	16.79		Mean	17.55
Std dev	0.43		Std dev	1.04
COV	2.54%		COV	5.94%

Table D-2: Fibrelam Poisson's Ratio (v_{12})

Coupon #	Panel 1 [GPa]		Panel 4 [GPa]	
1	0.17	AWT	N/A	AWT
2	0.18	LWT	N/A	LWB
3	0.17	LGM	0.17	AWB
4	0.18	LWT	0.17	LWT
5	0.17	AWT	0.17	LWT
Mean	0.18		Mean	0.17
Std dev	0.006		Std dev	0.003
COV	3.23%		COV	1.59%

Table D-3: Fibrelam Shear Modulus (G_{12})

Coupon #	Panel 1 [GPa]		Panel 4 [GPa]	
1	3.34	AGM	3.52	AGM
2	2.98	AGM	3.76	AGM
3	3.01	AWT	3.67	AGM
4	3.29	AWT	3.72	AWB
5	3.21	AGM	3.53	AGM
Mean	3.16		Mean	3.64
Std dev	0.17		Std dev	0.11
COV	5.22%		COV	3.07%

D.2 Additional UAV Pre-preg Tensile Test Results

Results from the UAV pre-preg tensile tests are given in the tables below. The statistical mean, standard deviation and coefficient of variance are given for each batch. The final mean and standard deviation is calculated from the 6 means and standard deviation of each batch and used for establishing a material property distribution.

Table D-4: UAV pre-preg Poisson Tensile test Result v_{12} from 0° coupons

	Individual Coupon Result: Poisson's Ratio (v_{12})						Batch Result		
Batch #	Coupon 1	Coupon 2	Coupon 3	Coupon 4	Coupon 5		Mean	Std dev	COV
1	0.17	0.15	0.20	0.15	0.16		0.17	0.02	12.51%
2	0.18	0.18	0.14	0.16	0.18		0.17	0.02	11.68%
3	0.15	0.15	0.18	0.13	0.18		0.16	0.02	13.15%
4	0.15	0.12	0.15	0.17	0.14		0.15	0.02	10.78%
5	0.15	0.13	0.14	0.15	0.15		0.14	0.01	5.47%
6	0.19	0.14	0.16	0.16	0.22		0.17	0.03	18.11%

Table D-5: UAV pre-preg Elastic Modulus Tensile test Result (E_2) from 90° coupons

	Individual Coupon Result: Elastic Modulus E_2 [GPa]						Batch Result [GPa]		
Batch #	Coupon 1	Coupon 2	Coupon 3	Coupon 4	Coupon 5		Mean	Std dev	COV
1	19.70	24.30	19.38	21.57	19.57		20.91	2.09	10.02%
2	21.23	20.22	20.88	20.20	21.03		20.71	1.44	6.93%
3	19.12	21.53	19.01	19.33	24.36		20.67	1.57	7.61%
4	18.98	19.27	20.02	19.45	19.80		19.51	1.68	8.61%
5	18.44	19.24	22.03	20.79	19.41		19.98	1.02	5.10%
6	18.93	18.59	18.47	19.68	21.70		19.47	1.33	6.81%

Table D-6: UAV pre-preg Shear Modulus Tensile test Result (G_{12}) from 45° coupons

	Individual Coupon Result: Shear Modulus G_{12} [GPa]						Batch Result [GPa]		
Batch #	Coupon 1	Coupon 2	Coupon 3	Coupon 4	Coupon 5		Mean	Std dev	COV
1	3.03	2.64	4.49	3.15	2.48		3.16	0.79	25.06%
2	3.23	2.87	3.33	3.01	3.24		3.13	0.54	17.33%
3	3.29	2.52	3.24	3.44	2.65		3.03	0.31	10.17%
4	3.19	3.09	3.12	3.43	3.79		3.32	0.37	11.18%
5	3.27	3.17	3.66	3.78	2.55		3.29	0.38	11.48%
6	4.79	3.80	3.84	3.63	4.34		4.08	0.62	15.11%

D.3 Additional Datasheet Info

The table D-7 is taken from the Evonik Röhm GmbH website (Evonik, 2011). Data values for Roha-cell 71 varies a little from that originally used in FEM and as received from the wing manufacturer. Values of Roha-cell 51 however, seem to correlate with the updated Roha-cell material properties.

Table D-7: Additional Roha-cell Datasheet Values

Properties of ROHACELL® WF

Properties	Unit	ROHACELL® 51 WF	ROHACELL® 71 WF	ROHACELL® 110 WF	ROHACELL® 200 WF	Standard
Density	kg/m³	52	75	110	205	ISO 845
	lbs./cu.ft.	3.25	4.68	6.87	12.81	ASTM D 1622
Compressive strength	MPa	0.8	1.7	3.6	9.0	ISO 844
	psi	116	246	522	1305	ASTM D 1621
Tensile strength	MPa	1.6	2.2	3.7	6.8	ISO 527–2
	psi	232	319	536	986	ASTM D 638
Shear strength	MPa	0.8	1.3	2.4	5.0	DIN 53294
	psi	116	188	348	725	ASTM C 273
Elastic modulus	MPa	75	105	180	350	ISO 527–2
	psi	10,875	15,225	26,100	50750	ASTM D 638
Shear modulus	MPa	24	42	70	150	DIN 53294
	psi	3,480	6,090	10,170	21750	ASTM C 273
Strain at break	%	3.0	3.0	3.0	3.5	ISO 527–2
						ASTM D 638

Technical data of our products are typical values for the nominal density.

Appendix E: Vibration Testing and Modal Analysis

E.1 Test Structure Surface Reflection

A test was performed on a Fibrelam panel to determine whether the reflectivity of the surface to be scanned by the laser vibrometer could be improved to attain less noisy FRFs. Three approaches were compared. Firstly an unprepared (clean) surface was tested, then the surface was spray painted with a reflective coating (paint) and finally reflective tape/stickers were used (tape).

The figure below give the results of an acceleration/voltage FRF transfer function obtained from the laser vibrometer tests on the Fibrelam panels. A vibro-pet setup with a periodic chirp actuation was used. Also the panel was not removed from the setup but rather surface treated in place in order to enhance the repeatability of the test setup for better comparison.
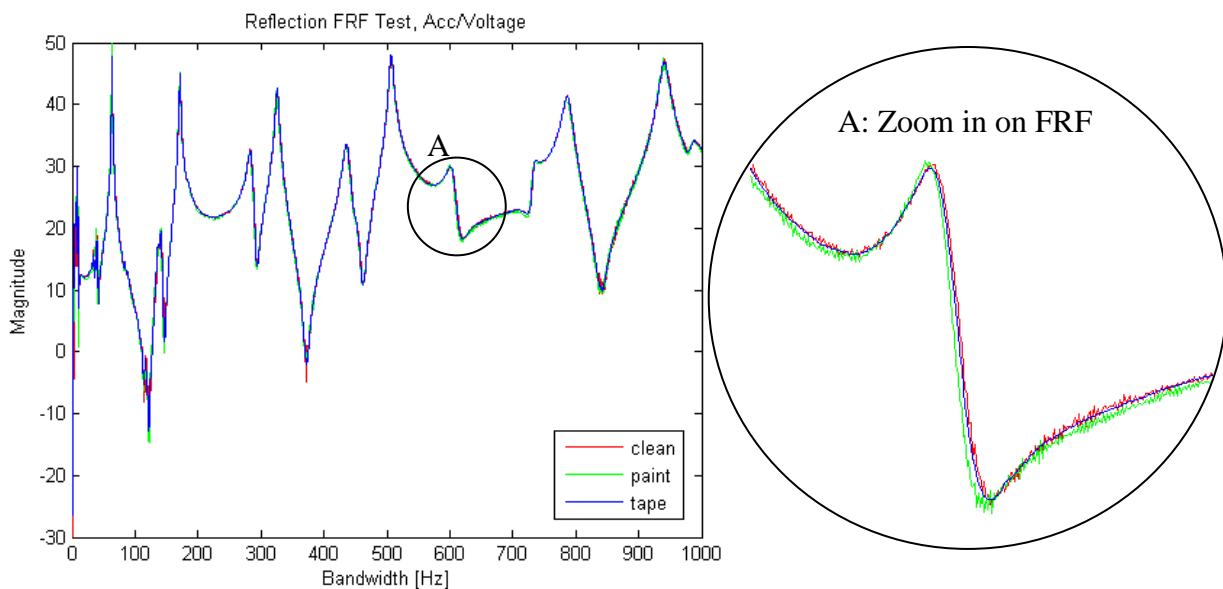

Figure E-1: Reflectivity Test, Fibrelam Panel

Zooming in on a Fibrelam mode, a clear improvement on noise level is noticed for the case of reflective tape/stickers (blue). This is true especially at the anti-resonances where low magnitude vibration is sensitive to noise. For this reason it was decided to utilise reflective tape for all vibration tests in this thesis, especially that of the black UAV wings that have particularly low surface reflectivity.

E.2 Wing 2 Discussion

Owing to debonding of the resin beading from the skin plies at the leading edge of wing 2, it could no longer be used for wing manufacture repeatability studies. This development has however presented an opportunity to test the developed damage detection methodology against another type of damage other than delamination. It must be mentioned though that an attempt was made to re-bond the leading edge before testing but as results below indicate, the effort was in vain.

The modal parameters extracted though OROS modal analysis is presented in the table below and compared to those of undamaged wing 1. A general drop in frequency of wing 2 across modes 2 to 6, suggests reduction in stiffness as a result of the damage. An equally interesting observation is the increase in modal damping, which grows in magnitude with modal order.

Table E-1: Accidentally Damaged Wing 2 Modal Parameters

Wing #	Frequency [Hz]			Modal Damping %		
	1	2	% Diff	1	2	% Diff
Mode 1	52.2	54.8	5.00%	0.37	0.41	9.76%
Mode 2	104.4	103.3	1.05%	0.43	0.48	10.42%
Mode 3	113.6	104.8	7.79%	0.45	0.52	13.46%
Mode 4	130.6	125.6	3.86%	0.44	0.5	12.00%
Mode 5	141.9	130.0	8.41%	0.49	0.64	23.44%
Mode 6	155.0	150.4	2.95%	0.34	0.73	53.42%

By superimposing mode shape 2 of the damaged wing along grid column 6 (where damaged occurred at the leading edge) onto the confidence region (figure E-2) developed in this dissertation, damage can be seen to slightly deviate the response at the leading edge from the confidence bounds.
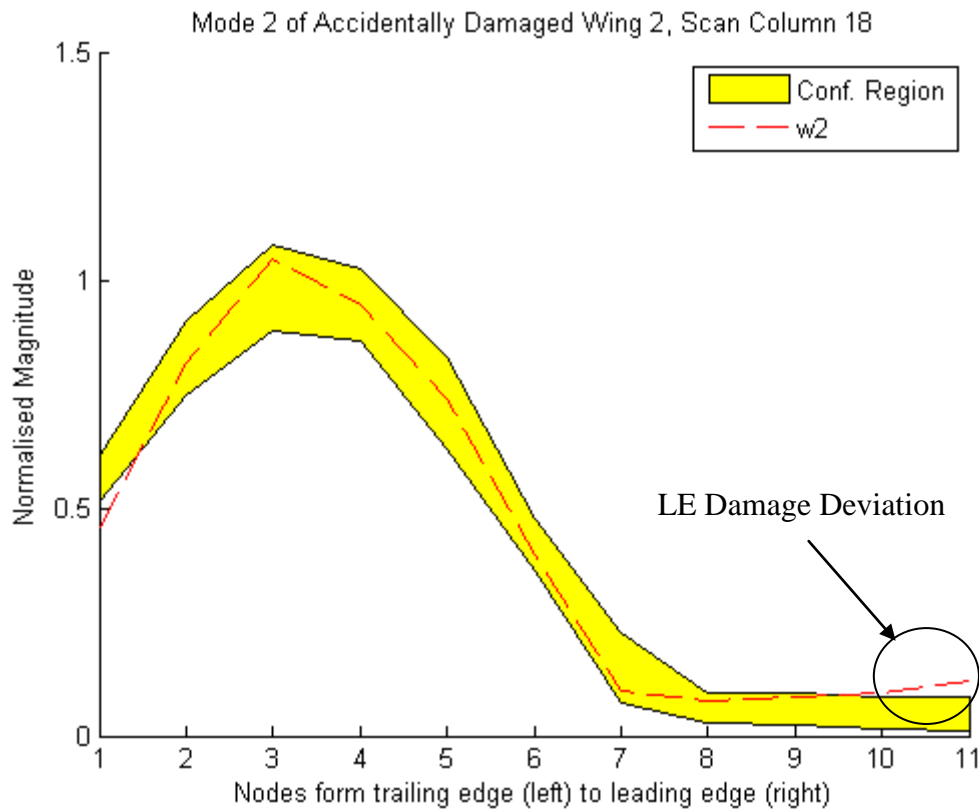

Figure E-2: Small Size Wing Modes

E.3 Medium and Small Wing Modal Analysis

In order to perform Multi-model updating, two addition sets of experimental tests had to be performed. These differed only in geometry of the test structure. Thus a wing (wing 1) was cut to a length of 275 mm and modal analysis was performed on the response. Likewise, the

wing was again cut to a length of 225 mm and analysed again. The modal parameters of these shortened wing geometries are given below.

The natural frequencies and damping factors of the first 6 modes are given in table (E-2). The frequency values are higher for the medium length wing than the full length wing and even higher for the short wing. This is just as a result of the overall structural bending stiffness increasing about the y-axis from decrease in length. The damping factors lie roughly in the range of the full size wing.

Table E-2: Medium and Short Wing Modal Parameters

Mode #	Medium Wing 275mm Length		Short Wing 225mm Length	
	Frequency (Hz)	Damping (%)	Frequency (Hz)	Damping (%)
1	154.77	0.60	169.84	0.51
2	185.22	0.49	187.66	0.47
3	225.64	0.37	264.46	0.62
4	229.49	0.35	338.22	0.38
5	327.84	0.40	372.31	0.56
6	342.20	0.60	384.64	0.44

The mode shapes for the medium and short wings are presented in figures E-3 and E-4 respectively. The first 3 modes are similar for the medium and short wings but differ in higher order.
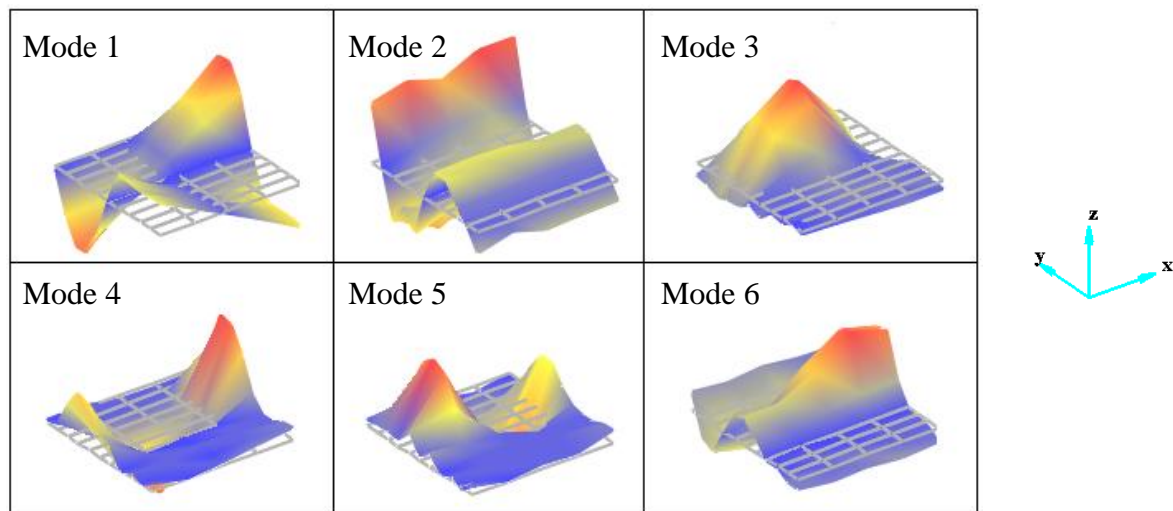

Figure E-3: Medium Size Wing Modes

Notice though that skin dynamics are still complicated and as a result will cause difficulty in numerical simulation.
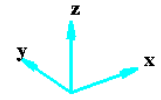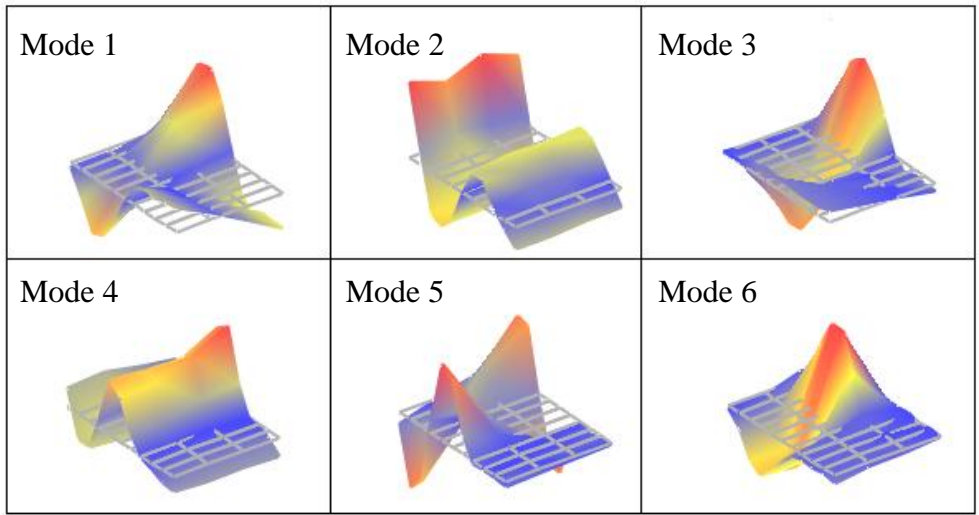
Figure E-4: Small Size Wing Modes

Appendix F: Additional Model Updating Results

The Fibrelam multi-model updating procedure was similar to that of the UAV wings. The 2D orthotropic material properties of both the Fibrelam skins and honeycomb cores were updated and converged to the values in the table below.

Table F-1: Updated Material Property Parameters - Fibrelam

	Property	E_1 **[GPa]**	E_2 **[GPa]**	G_{12} **[GPa]**	v_{12}	ρ **[kg/m^3]**
Skins	**Before**	16.67	16.79	3.16	0.18	1546.64
	After	17.78	18.39	4.90	0.17	1466
	% Diff	6.66%	9.53%	55.06%	5.56%	5.21%
Core	**Before**	0.040	0.025	0.010	0.20	48.0
	After	0.036	0.020	0.014	0.16	47.50
	% Diff	11.25%	20.00%	40.00%	20.00%	1.04%

The updated properties did not have significant changes except in the case of the shear elastic moduli. The 45° tensile coupons were susceptible to scissoring, and despite following ASTM specifications, the result was an under estimation of the stiffness modulus. In the case of the honeycomb, the shear modulus is a critical parameter of the structure. The simplification of the core modelling may be the cause of the large percentage change.

Response parameters were improved as indicated in the table below. The natural frequencies of the first 6 modes are given with their updated values. In general the frequency values increased, which correlates with the increase in skin stiffness values.

Table F-2: Updated Natural Frequency - Fibrelam

EMA [Hz]	FEA Before [Hz]	% Diff Before	FEA After [Hz]	% Diff. After
64.1	63.2	1.38%	64.3	0.35%
140.6	131.5	6.51%	147.3	4.76%
171.7	173.7	1.20%	173.3	0.95%
286.6	274.2	4.35%	291.1	1.55%
324.8	338.7	4.28%	328.3	1.06%
439.5	438.1	0.32%	432.8	1.52%